NORTHWESTERN UNIVERSITY

Surface Structures of the Metal-Oxide Materials Strontium Titanate and Lanthanum Aluminate

A DISSERTATION

SUBMITTED TO THE GRADUATE SCHOOL IN PARTIAL FULFILLMENT OF THE REQUIREMENTS

for the degree

DOCTOR OF PHILOSOPHY

Field of Materials Science & Engineering

By

Danielle M. Kienzle

Evanston, Illinois

July 2013

Abstract

A wide array of techniques were applied in this research to investigate the perovskite materials $SrTiO_3$ and $LaAlO_3$ with the goal of furthering the understanding of oxide surfaces. Specifically, a combination of transmission electron diffraction, direct methods and density functional theory was used to determine the structure of the $SrTiO_3$ (001) $(\sqrt{13}\times\sqrt{13})R33.7^{\circ}$ surface reconstruction. It has a TiO_2-rich surface with a 2D tiling of edge or corner-sharing TiO_5 octahedra. By tiling these units and forming network surface structures ranging from ordered, like the 2x1 and c(4x2), to pseudo-ordered, like the c(6x2), to a disordered glass-like surface layer made up of TiO_x units, dictated by local bond valence sums.

The $LaAlO_3$ (110) 3x1 surface reconstruction, here reported for the first time, was found to have a hydroxylated Al-rich surface with X-ray photoelectron spectroscopy. Transmission electron diffraction data and direct methods revealed a high resemblance to the previously solved $SrTiO_3$ (110) 3x1 reconstruction leading to a hydrated version that fits the for $LaAlO_3$ 3x1 structure. The hydroxyl groups are necessary to balance the surface polarity, an issue arising from the difference in cationic valences between La/Sr and Al/Ti.

Also reported and investigated here for the first time is a $LaAlO_3$ (100) 5x2 reconstruction. A direct methods analysis was done for several sets of recorded diffraction pattern; however the results have yet to lead to an atomic surface structure solution. X-ray photoelectron spectra were collected over a range of detector-to-surface-normal angles elucidating an Al-rich surface layer. X-ray photoelectron intensities were calculated for a model of alternating Al and La layers over a

range of grazing angles and varying amounts of Al in the top surface layer. An Al concentration of 0.5 was found to give the best fit to experimental results.

Approved by

Professor Laurence D. Marks

Department of Materials Science and Engineering

Northwestern University, Evanston, IL 60208, U.S.A.

Acknowledgments

First and foremost, I would like to thank my adviser, Laurie Marks, without which this dissertation would not be possible. I am truly grateful for the opportunity and the experiences I have had at Northwestern in the L. D. Marks Group. For as much as I have learned about surfaces, I have also learned a lot about myself and what I can accomplish. I would also like to thank my Qualifier committee: Professors Scott Barnett, Chris Wolverton, and Peter Stair, as well as my defense committee: Professors Scott Barnett, Thomas Mason, and Ken Poeppelmeier, for their time and energy.

I would like to thank the staff at the Electron Probe Instrumentation Center (EPIC) at Northwestern University for their expertise, interest, and readiness to help me with any sample preparation or instrumentation. Dr. Shuyou Li and Dr. Jinsong Wu, in particular, were indispensable to me and could always be counted on for getting me what I needed, be it more slurry for the dimple grinder or the electron beam I managed to "lose" from the TEM screen…again. I would also like to thank Ken Eberly from Hitachi for the time he spent with maintenance and repairs for our groups UHV-TEM. Thanks to the Materials Science Department staff, especially Peggy Adamson for fielding all of my "clueless grad student" questions; the Chemistry Department staff and Pat Fulton at the Catalysis for Catalysis for helping me schedule group meetings over the years.

Thank you to all past and present L. D. Marks members: Courtney, Yingmin, Yougui, Jim C., Brian, for teaching me how to make a TEM sample, use SPEAR, and tend goal on the MatSci floor hockey team; Jim E. and Andres for your collaboration on all things STO; Ariel,

Emilie, Yifeng, Chuandao, Yuyuan for providing a sounding board for me to work through research problems; Thanks to Richard Zou who worked with me as an undergraduate and did much of the sample preparation for the LAO 3x1 in Chapter 5.

A special thanks to all of the friends I have made at Northwestern, Steph, Minna, Marie, Marc, Jason, Matt, Megna, Ted, David, Mitch, Alok, Jon, Andres, Ariel, Brian, Prad, for all the good times and shared experiences that will stay with me forever. Thank you to my parents for their unwavering support and love no matter the circumstances. And to Justin, who has been encouraging and supporting me through the last few years of my graduate career, just meeting you may have been my greatest accomplishment.

Table of Contents

List of Abbreviations

AES	Auger electron spectroscopy
APW	Augmented plane waves
BV	Bond valence
BVS	Bond valence sum
DFT	Density functional theory
DL	Double layer
DM	Direct methods
DP	Diffraction pattern
EDM	Electron Direct Methods
GGA	Generalized gradient approximation
HREM	High-resolution electron microscopy
LDA	Local density approximation
LEED	Low energy electron diffraction
NC-AFM	Non-contact atomic force microscopy
PBE	Perdew, Burke, Ernzerhof
REM	Reflection electron microscopy
RMT	Muffin-tin radius
RT13	$(\sqrt{13}\times\sqrt{13})R33.7^{o}$
RT2	$(4\sqrt{2}\times\sqrt{2})R45^{o}$
RT5	$(\sqrt{5}\times\sqrt{5})R26.6^{o}$
SPEAR	Specimen Preparation, Evaluation, Analysis, and Reaction System

STM	Scanning tunneling microscopy
TED	Transmission electron diffraction
TEM	Transmission electron microscopy
TPSS	Tao, Perdew, Staroverov, Scuseria
UHV	Ultra-high vacuum
XPS	X-ray photoelectron spectroscopy

List of Figures

List of Tables

1. Introduction

1.1 Motivation

The surface is where the action is. It is the boundary between the bulk of a material and its environment, whether it is air, water, or another material. How a surface interacts with its environment will ultimately affect its properties. Knowledge of how a surface interacts is paramount to many technologies and industrial processes such as heterogeneous catalysis, one of the workhorses of the chemical industry. Reactants interact with a catalyst by adsorbing onto the catalyst's surface, forming chemical bonds with surface atoms, which allows for a reaction to proceed efficiently. But, with which specific atoms do reactants bond? Is the local bonding of one surface atom preferable to another? Knowing the specific atomic sites that are active in a catalytic reaction would not only help us understand the process more completely, but would also enable us to design better catalysts. This is just one example of how a comprehensive knowledge of a material's surface structure could open doors to technological advancements.

There are thousands of known bulk crystal structures along with a thoroughly developed set of analogies and rules to help characterize the bulk structure of an unknown material. The same cannot be said for the atomic surface structure, which may deviate from the bulk. When the "surface" of a material is discussed, it refers to the layer of atoms where the repetition of the bulk ends. These atoms do not have the same local bonding environment as the atoms in the bulk and are left under-coordinated with "dangling bonds." To stabilize, the surface can atomically reconstruct, absorb foreign adatoms such as H_2O, or electronically reconstruct.

Atomic rearrangements at the surface can achieve a lower energy by structural relaxation

or reordering leading to drastically different properties. If the surface atoms are arranged with a periodically repeating unit larger than that of the bulk, the resulting structure is referred to as a surface reconstruction and is described by its surface unit cell size relative to that of the bulk's.

An example of this is shown in Figure 1.1 comparing the bulk surface unit cell (1x1) with a known $SrTiO_3$ (001) 2x1 reconstructed surface unit cell which is twice the length in the horizontal direction and the same length in the vertical direction. It is a key point to note that having the same surface periodicity does not imply having the same structure.

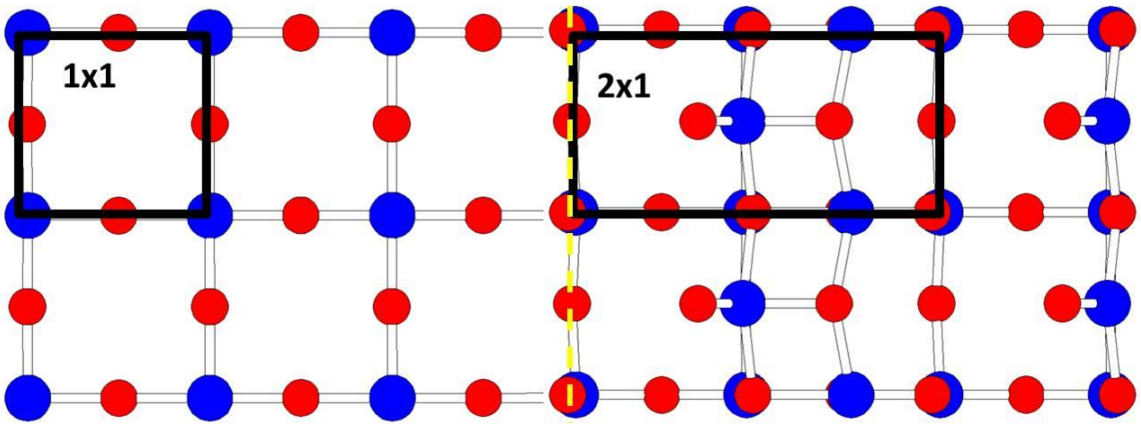

Figure 1.1. Top view of $SrTiO_3$ (001) with bulk TiO_2 termination (left of dashed line) with 1x1 surface unit cell outlined. (Right of dashed line) shows the 2x1 surface reconstruction [1] with the surface unit cell outlined. The size and periodicity is defined relative to the surface unit cell with the 2x1 twice as large in one direction.

In this dissertation, the study of atomic surface structures is presented for the metal-oxide perovskite materials strontium titanate and lanthanum aluminate. $SrTiO_3$ is one of the most widely used substrates in literature for thin film growth since it is now routine to be able to

prepare atomically flat TiO_2 surfaces by buffered-HF etching for epitaxial growth [2, 3]. Additionally, with the advent of processes like atomic layer deposition, molecular beam epitaxy, and pulsed laser deposition that allow for growing films layer by layer, interest in $SrTiO_3$ surfaces has increased because of how necessary it is to determine the effect of substrate on the film at the interface. Applications include epitaxial thin film growth of high-T_c superconductors [4-6], interface layers (or buffer layers) in electronic devices, such as between GaAs and silicon [7, 8] or as a gate dielectric in metal-oxide semiconductor based structures [9, 10]. It may also be possible to take advantage of unique surface nanostructures that $SrTiO_3$ can exhibit, such as nanolines [11] or arrays of nanodots [12] for use as nanowires or quantum dots. More recently, $SrTiO_3$ has garnered further interest due to the unique electronic properties observed, such as a conductive 2D-electron gas formed at a ultra-high vacuum (UHV)-cleaved $SrTiO_3$ surface [13] or similarly at $SrTiO_3/LaAlO_3$ interfaces [14, 15]. The wide range of, and largely unexplored phenomena exhibited at such oxides interfaces is promising for a new generation of electronic devices far beyond semiconductor-based devices.

$SrTiO_3$ is a transition metal oxide with a perovskite structure (Figure 1.2) that exhibits ferroelectric [16] and photocatalytic [17] properties. It is an insulator with a band gap of 3.2 eV at 25 ºC [18], but behaves as a semiconductor, or even superconductor [19] when chemically reduced. For our research purposes, $SrTiO_3$ is a model system for surface studies because of its relatively simple structure. The structure can be visualized as corner-sharing titanium octehedra at the center of a cell with 12-coordinated strontium at the corners of the cell. The unit cell is cubic with a = 3.905 Å and $Pm\bar{3}m$ symmetry. Along its [001] direction, the bulk structure can be described as alternating layers of SrO and TiO_2. Truncating the bulk will create either a SrO or TiO_2 surface layer, depending on where the truncation occurs. As will be later described, these

bulk-truncated surface layers are typically not the lowest energy configuration, and upon annealing they will reconstruct. Along the [110] direction, alternating layers of $SrTiO^{4+}$ and O_2^{4-} make up the bulk and render the surface polar, meaning it will not be valence-neutral and there will be a nominal 2+/2- valence excess, depending on the terminating bulk layer. This is also energetically unfavorable, creating holes in the valence band or electrons in the conduction band.

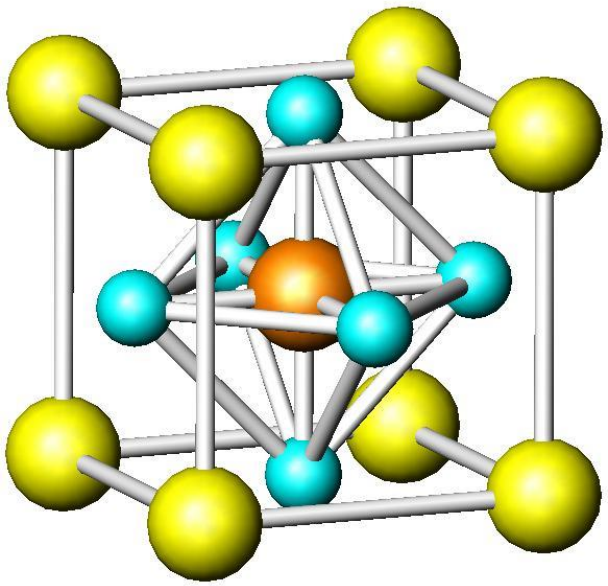

Figure 1.2. Cubic perovskite structure ABO_3. The 12-coordinated A site (Sr/La) in yellow, octahedral B site in orange (Ti/Al), and blue are oxygen.

It should be noted that $SrTiO_3$ (001) is categorized as a non-polar surface because each layer of SrO and TiO_2 with formal valence values, Sr^{2+}, Ti^{4+}, and O^{2-}, appears to have a valence neutral surface. However, $SrTiO_3$ is not fully ionic and the Ti-O bond presents a non-negligible part of covalent character as well as the loss of ideal coordination at the surface. The true ionic

valences are, therefore, most likely not equal to their formal charges, making it unlikely that each plane of atoms in a unit cell is valence-neutral. This point is helpful in understanding the driving force behind $SrTiO_3$ reconstructions and why so many are readily observed on the surface of $SrTiO_3$ (001).

$LaAlO_3$ is another member of the perovskite structure family (Figure 1.2). Its structure is formally rhombohedral with $a = b = c = 5.357$ Å and $\alpha = \beta = \gamma = 60.1^{o}$, however it is often thought of as pseudo-cubic with $a = b = c = 3.79$ Å and $\alpha = \beta = \gamma = 90.05^{o}$. A rhombohedral-to-cubic phase transition takes place at 435 ± 25ºC. For our purposes, we will be treating $LaAlO_3$ as cubic with $Pm\bar{3}m$ symmetry. In the perovskite structure, aluminum occupies the 6-fold coordinated spot and lanthanum occupies the 12-fold coordinated position. Lanthanum and aluminum have formal valences of 3+ and oxygen has 2+. Consequently, along the cubic <001> direction, $LaAlO_3$ consists of alternating layers of $(LaO)^{+}$ and $(AlO_2)^{-}$, as shown in Figure 1.3. At any given interface between an AlO_2 and a LaO layer within the bulk, the valence is balanced because the LaO layer contributes ½+ of its total 1+ charge to the AlO_2 layer above it and the other ½+ to the AlO_2 layer below it. AlO_2 layers do the same by contributing ½- of their total 1- charge to the LaO layer above and ½- to the LaO layer below. At the surfaces, however, the valence is unbalanced and therefore classified as polar.

$LaAlO_3$ is a relevant oxide used as substrates for thin film growth, such as high T_c superconductors [20-22]. Although $SrTiO_3$ is widely used for this purpose, $LaAlO_3$ may be advantageous for materials such as $Ba_2YCu_3O_7$ because it has a much lower dielectric constant than $SrTiO_3$ [23]. Like $SrTiO_3$, $LaAlO_3$ is also a potential candidate for gate dielectrics or buffer layers in small-scale electronic devices [24-27], as well as, useful for catalytic applications such as the support material for Pd particles for the reduction of NO by CO [28].

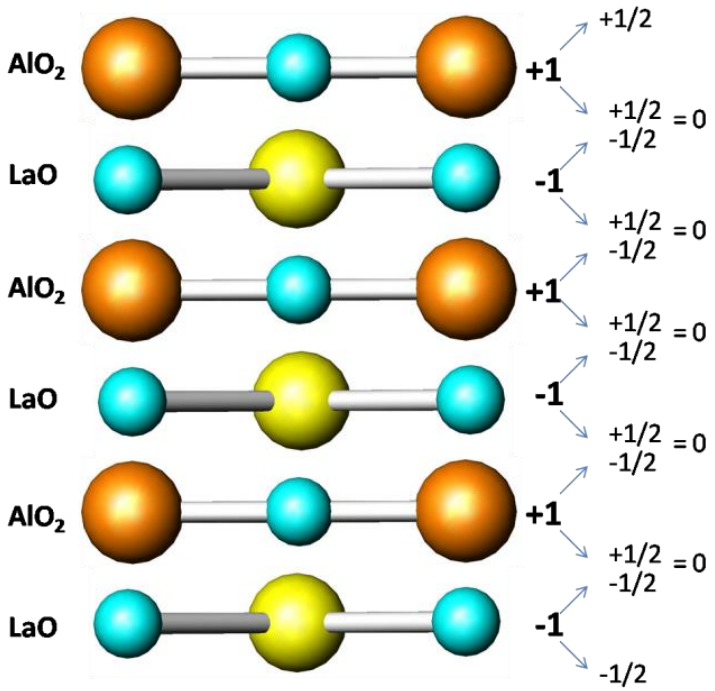

Figure 1.3. Schematic atomic model of stacked layers of $LaAlO_3$ in the <001> directions. La are yellow, Al are orange, and O are blue. Within the bulk, charged layers balance with the layer above and below, except at the surface. If AlO_2 or LaO is the terminating layer, there is a 1+ or 1- valence per (1x1) surface unit cell, respectively.

The overarching goal of this work is to further the fundamental, scientific understanding of oxide surfaces by studying in depth model systems, like $SrTiO_3$. This is done not only by determining the structure of surface reconstructions, but also by determining how reconstructions relate to other reconstructions on the same surface, and why one reconstruction forms versus another. Understanding the surface is the first step to controlling the surface.

A second goal is to relate the surface behavior of $SrTiO_3$ to a similar perovskite oxide, $LaAlO_3$, and leverage what is already known about $SrTiO_3$ to aid in in solving $LaAlO_3$ surface reconstructions. By determining surface structures of $LaAlO_3$, generalities will emerge that will perhaps be applicable to even more oxides.

1.2 Organization

This dissertation is presented as follows: Chapter 2 details the general concepts for experimental and theoretical techniques utilized in this work. More specific details relating to a specific reconstruction study can be found in subsequent chapters. Chapter 3 provides an overview of published research on $SrTiO_3$ surface reconstructions, and the different views on what structural changes are occurring to produce different reconstructions, including strontium adatoms, oxygen vacancies, and TiO_2 double surface layers. Chapter 4 presents the atomic surface structure for the $SrTiO_3$ (001) ($\sqrt{13}$x$\sqrt{13}$)R33.7° reconstruction and the methods used to solve it via transmission electron diffraction. Chapter 5 presents the investigation and first report of the $LaAlO_3$ (110) 3x1 surface reconstruction, and describes how it is structurally similar to the $SrTiO_3$ (110) 3x1 structure. Chapter 6 present the investigation and first report of the $LaAlO_3$ (001) 5x2 surface reconstruction with X-ray photoelectron spectroscopy. Chapter 7 summarizes the findings of this work and offers suggestions for further work.

2. Techniques

This chapter describes the experimental and theoretical techniques employed for the research presented in the following chapters. Additional information specific to the material system is provided in each subsequent chapter.

2.1. Sample Preparation

Conventional sample preparation techniques were used to obtain self-supported transmission electron microscopy (TEM) specimens; "Self-supported" means the center of a circular disc-shaped sample is thinned until a small hole is formed, while the edge of the disc remains thick to enable handling. Ideally, this hole will be as small as possible, on the order of a few microns. From the center hole to the outside edge, the thickness of the sample gradually increases. The inner sample edge is the thinnest part and electron-transparent; the greater the area of electron transparency, the better the sample.

All samples used for work in this dissertation were prepared from single crystal substrates (10 x 10 x 0.05 mm) of known orientations, commercially purchased from MTI Corporation (Richmond, CA) and cut into discs 3mm in diameter with a rotary disc cutter. The discs were mechanically thinned to thicknesses of approximately 100 μm with silicon carbide sandpaper. Next, the discs were dimpled with a Gatan 656 Dimple Grinder in combination with 0.5 μm diamond slurry, such that the thickness at the center was thinned to approximately 15 μm, while the outer edges of the disc remained thick, resembling a "dimple" in the surface. The samples were then ion milled using a Gatan Precision Ion Polishing System with Ar^+ ions at

energies in the range of 3-4.5 keV for 1-3 hours until a small hole could be seen with an optical microscope at 20x magnification.

The process of sample preparation inflicts stress, defects, and strain on the sample, as well as leaving the surface reduced and non-stoichiometric from the ion bombardment. Fortunately, a well-ordered surface can be recovered by annealing in air or oxygen at temperatures high enough to allow surface diffusion, but not high enough for bulk diffusion [29]. Samples were annealed in a Carbolite STF 15/51/180 tube furnace with a temperature limit of 1500°C. Within the tube furnace, samples were placed in an alumina boat inside a quartz tube. The ends of the quartz tube were open to anneal in an air environment, or alternatively, end-caps could be attached to the ends of the tube to introduce flowing gas regulated by a Matheson flow meter adjusted to 50 cc/min. Figure 2.1 shows a representative image of a sample after its preparation, and again, after an annealing treatment.

2.2. Transmission Electron Microscopy and Diffraction

TEM was the primary investigative tool used in the presented research. The basic idea of TEM involves a beam of electrons accelerated through an applied voltage, transmitted through a given sample, and recorded on the other side. Image contrast arises from the interaction of the electron beam with the crystal structure. The beam can be manipulated by magnetic lenses and apertures to access different modes and obtain relevant information. The two main modes of operation, imaging (real-space) and diffraction (inverse Fourier-space), can be easily toggled between to obtain an image and corresponding diffraction pattern (DP) from the same sample area. For single crystals, a DP is a two-dimensional array of spots dependent on the symmetry and

crystallographic orientation of the illuminated area of sample, with each spot representative of a plane in the crystal.

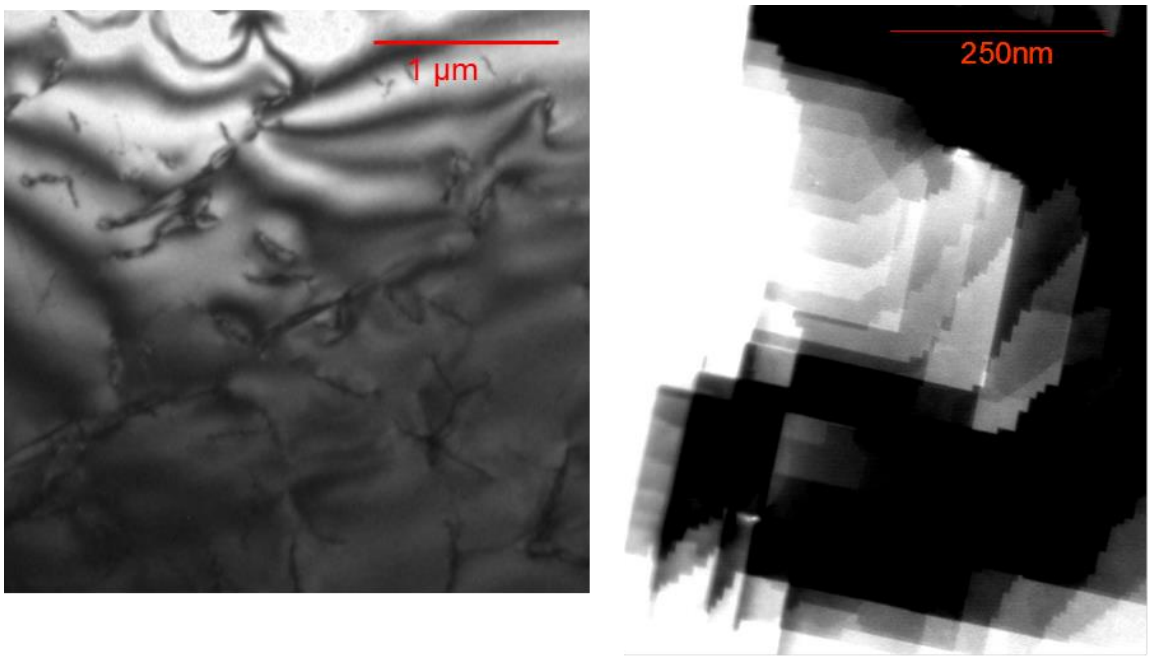

Figure 2.1. (Left) Bright field TEM image of $SrTiO_3$ (001) before and after (right) annealing.

Diffraction from a sample volume will also be affected by the size and shape of the sample. If a sample was infinite in all directions, the DP would be a point. In practice, a single crystal sample can be considered infinite in the plane perpendicular to the beam, but finite in the direction parallel to the beam. This finite thickness is represented by reciprocal lattice rods, or "relrods" in reciprocal space. Since DP spots arise from the Ewald Sphere construction intersecting with reciprocal space points, the elongation of these relrods can cause DP spots over a range of angles.

For a reconstructed surface, the atoms in the top-most layers will be significantly displaced from bulk positions. The shape effect from the surface layers will cause a greater elongation of the relrods parallel to the beam relative to the bulk because of its even thinner thickness. This effect can be taken advantage of by tilting the sample slightly away from the strong-scattering zone axis so that the intensity of bulk diffraction spots is decreased, effectively increasing the signal from surface diffraction. See Figure 2.2.

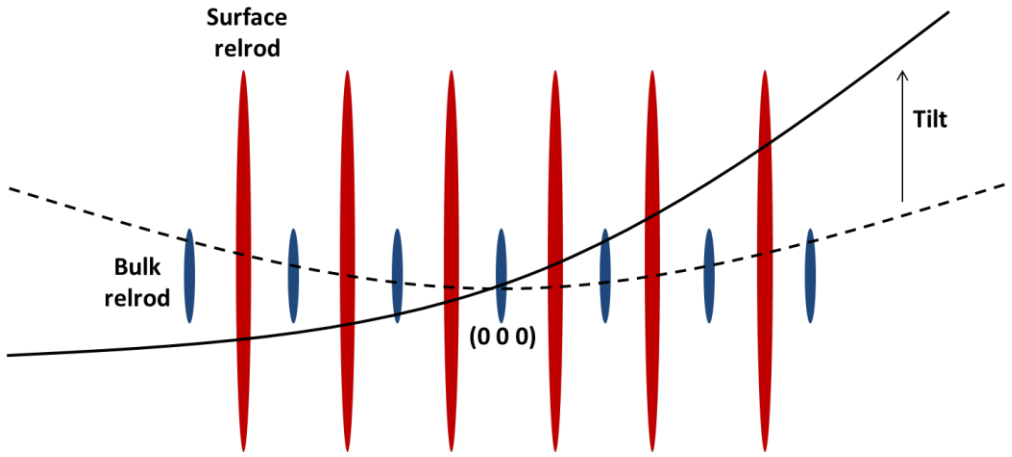

Figure 2.2. Schematic illustration of reciprocal lattice rods for a crystal with a reconstructed surface layer. Tilting off the zone axis (0 0 0) decreases the intersection with bulk relrods while still intersecting with surface relrods, effectively strengthening the surface diffraction signal.

Although it may seem counter-intuitive to use TEM for surface analysis because electrons go *through* the sample, thus interacting with a top surface, bulk, and bottom surface, it offers many advantages over other commonly used surface techniques such as low energy electron diffraction (LEED). LEED makes use of an electron beam with a much lower energy (20-200 eV) relative to transmission electron diffraction (TED) (100-300 keV). The electrons

bombard the sample and are back-scattered to form a DP. Because of the low energy, the electrons have a small mean free path and therefore a shallow sampling depth of a few Angstroms, making LEED a highly surface-sensitive technique.

In a diffraction experiment the intensity of each diffracted beam is recorded and is related to the square of its wave amplitude; however, the phase of the wave is not. This is well-known as the "phase problem". If both the phase and amplitude were known, an inverse Fourier transform would return the real-space structure. Since this is not the case, the phases need to be approximated, and this is where the crucial difference between LEED and TED comes in; LEED has a higher percentage of dynamical diffraction, or multiple scattering events, that make a quantitative analysis much more complicated. A simpler kinematical approximation assumes single scattering events, and this has proven true for surface structure determination via TED [30].

TEM characterization of samples for this work was done in the Northwestern Electron Probe Instrumentation Center (EPIC) on a Hitachi H-8100 transmission electron microscope operating at an accelerating voltage of 200 kV. Bright field and dark field images, as well as diffraction patterns, were obtained from the samples. Diffraction was done with a small probe (small spot size, small condenser aperture) rather than selected area diffraction, which allows diffracted beams from an area outside the aperture to contribute to the pattern, adding to the noise.

Since the intensity of surface spots can vary over several orders of magnitude, a series of diffraction patterns from the same area were recorded using photographic film for a range of

exposure times, from 1-90 seconds. Once developed, the films were digitized using an Optronics P-1000 microdensitometer with a 25 μm pixel size.

When irradiating the area of a sample for an extended period, such as during the collection of a series of diffraction patterns, beam damage can be an issue and degrade the surface. TEM images arising from the same sample area were taken early and later in a TEM session, so they can be compared for evidence of beam damage. For this work, any effects of beam damage were not observed for either $SrTiO_3$ or $LaAlO_3$.

2.3. Direct Methods

In a diffraction experiment, the way in which a crystal scatters radiation is described by its structure factor, F_{hkl}, defined by

$$F_{hkl} = \sum_{j=1}^{atoms} f_j \exp(2\pi i(hx_j + ky_j + lz_j))$$

where *f* is the atomic scattering factor for each atom type, *hkl* is the crystal plane, and (*x,y,z)* is the atomic position, relative to the bulk unit cell. Theoretically, the inverse Fourier transform of a crystal's structure factor will result in a real-space map of scattering potential (electron density for X-ray irradiation), i.e., the atom positions. However, in structure determination, the atom positions are the unknown and need to be found. The phase of the beam, Φ, contains the position information shown here:

$$\Phi = 2\pi\,(\,hx_j + ky_j + lz_j\,).$$

while the square of amplitude, $|F|^2$, can be measured directly from diffraction intensities ($I = |F|^2$).

In the past, the “phase problem” was tackled for structure determination of bulk crystals using X-ray data by using *a priori* information to obtain and develop constraints and probability relationships between the phases of diffracted beams. The set of these methods is called direct methods (DM) and is now routinely used for determining protein structures [31] and has been successfully used for surfaces [32].

The DM analysis for the surface structure determination in this work was done using the software package Electron Direct Methods (EDM v3.0) [33] and begins with measuring intensities of diffraction spots from experimentally obtained diffraction patterns. A set of phases for the measured intensities is initially approximated and EDM uses a genetic algorithm to iteratively search the solution space for the best phase sets. The output, in most cases, is a set of possible phase sets, each with their own, now calculable, scattering potential map.

Further refinement of atom positions can be done by comparing how well the calculated structure factors fit the experimental data using two metrics, R_1 and χ^2.

$$R_1 = \Sigma \mid I_{meas} - I_{calc} \mid / \Sigma I_{meas}$$

$$\chi^2 = 1/(N-M)\Sigma((I_{meas} - I_{calc})/\sigma)^2$$

where I_{meas} is the measured intensity, I_{calc} is the calculated intensity, N is the number of data points, M is the number of variable parameters, and σ is the measurement error. It is also helpful for uncovering atom positions not represented in the map. In the case of oxides, the oxygen atom positions in a map are typically not found. In this case, knowledge of the bulk structure, the preferred coordination of the cations, and valence compensation must be used to deduce oxygen positions.

2.4. Density Functional Theory

Density functional theory (DFT) is a way to solve a quantum many-body problem, such as a solid material composed of positively charged nuclei and negatively charged electrons, by solving the time-independent Schrodinger's Equation for the ground state energy:

$$\hat{H}\Psi(r_1, r_2, \dots, r_N) = E\Psi(r_1, r_2, \dots, r_N)$$

where Ψ is the wavefunction of the system, E is the energy, r_i is the position of the ith electron, and $\hat{H}$ is the Hamiltonian functional. The Hamiltonian contains operators for the kinetic energy of electrons and nuclei, and for Coulombic interactions between electrons and nuclei, electrons and other electrons, and nuclei with other nuclei.

This problem is made easier with the Born-Oppenheimer approximation, which assumes nuclei are at fixed positions because they are relatively much heavier and slower than electrons. The consequence of this is that the kinetic energy of the nuclei goes to zero and their effect on electrons can be reduced to a single external positive charge. Consequently, a many-particle system is now reduced to a many-electron system.

The Hohenburg-Kohn Theorems [34] form the basis for DFT and state that there is a one-to-one correspondence between the ground state density of a many-electron system and the external potential, and the density that minimizes the external potential is the ground state energy. The implication of this is that the electron density contains as much information as the wavefunction, and observable quantities can be found from the density alone.

Furthermore, Kohn and Sham proposed a fictitious system of N non-interacting electrons, whose sum represents the electron density of the real system and whose kinetic energy and

electron density are known from orbitals [35]. The energy functional of the system can be written as:

$$E[\rho] = T_s[\rho] + V_{ext}[\rho] + V_H[\rho] + V_{xc}[\rho]$$

where T_s is the kinetic energy of the fictitious system, V is the energy computed from classical coulombic electron-electron interactions, and V_{xc} is the exchange-correlation functional shown here:

$$V_{xc}[\rho] = (T[\rho] - T_s[\rho]) + (V_{ee}[\rho] - V_H[\rho]).$$

V_{xc} is a sum of the errors arising from the difference between the kinetic energy of a system of non-interacting electrons and the actual kinetic energy ($T[\rho]$), and the difference between the actual electron-electron interaction ($V_{ee}[\rho]$) and the classical interaction. The correspondence of electron density between the fictitious and real systems is exact if the functionals are known exactly. V_{xc} is the only functional that needs to be approximated; thus, the accuracy of DFT is highly dependent on the V_{xc} approximation chosen.

The first type of approximation for the V_{xc} functional is called the local density approximation (LDA) [36]. It assumes that the exchange-correlation energy of a particular density can be found by dividing the material into infinitesimally small volumes with a constant electron density corresponding to that of an equal volume of electron gas whose density is numerically known. A natural extension of this approximation is the generalized gradient approximation (GGA) [37] that depends on the (local) density of each volume as well has the densities of neighboring volumes or the "gradient" of the densities.

No matter which approximation is used, the goal is to reduce the problem from an infinite set of single-particle equations to a finite set described by φ_m single-particle orbitals:

$$\varphi_m = \sum_{p=1}^{P} c_p^m \varphi_p^b$$

where c are the coefficients being solved for using a particular basis set, φ^b. In principle, P is infinite and φ_m is found exactly, but practically, limits must be placed on P to solve. It is important to choose a basis set that best describes φ_m with the fewest number of functions; describing φ_m becomes a tradeoff between accuracy and computational time.

Using a basis set of plane waves is a common approach because it is unbiased and mathematically simple. The number of plane waves to use is decided by the smallest length dimension to be described in real space. The number of plane waves can be further reduced if the potential of regions closest to the nucleus, where electrons are not involved in bonding, are given a "pseudopotential" described by less plane waves.

Augmented plane waves (APW) is another basis set that defines a border between this region in the center of the atom, where electrons behave more like free electrons, and an outside interstitial area. The border between inner core electrons and outer valence electrons is called the muffin-tin radius (RMT). Outside the muffin-tin sphere, plane wave functions are still used, but inside, more atom-like spherical harmonic functions are employed. A condition for this basis set is that the functions match at the RMT sphere boundary. An energy dependence in the atom-like functions leads to a non-linear solution and is, therefore, computationally more intensive. Adding local orbitals (lo) to APW improves the treatment of semi-core electrons.

For this work, DFT was primarily used to relax a structure to its lowest energy configuration and calculate surface energies. DFT calculations were performed using WIEN2k [38] with an APW+lo basis set. The exchange correlation term was approximated using the Perdew, Burke, and Ernzerhof (PBE) version of GGA [39]. While PBE is commonly used, it was designed for bulk and does not approximate well for surface and interface energies as it goes to an incorrect limit in vacuum. This has become known as the surface intrinsic error [40]. More modern functionals for surfaces use a fit to the jellium surface energy as a constraint. The one used for the $LaAlO_3$ DFT work in Chapter 5 is the PBEsol [41], which is a slightly different parameterization than PBE. It does a better job of matching the bulk lattice parameters and surface energies. Unfortunately, it is slightly more covalent than PBE. A hybrid PBE functional called PBE0 [42, 43], which adds a small component of exact-exchange for relevant orbitals, in this case, *d*-electrons, was used. By doing so, the ionicity of bonding is increased, which can be underestimated with PBE [44]. With this hybrid component added to PBEsol, it is called PBEsol0.

A meta-GGA functional called TPSS (Tao, Perdew, Staroverov, Scuseria) was also employed, which includes the Kohn-Sham orbital kinetic energy density along with the electron density and its gradient [45]. Additionally, a combination of TPSS and PBE0, called the TPSSh functional, was used [46] for $SrTiO_3$ calculations in Chapter 4. The TPSSh functional allows for better treatment of both *d*-electrons and surface energies. The meta-GGA functional corresponding to PBEsol is called revTPSS [47], and the corresponding hybrid is revTPSSh.

For $SrTiO_3$, it is better to use hybrids. For $LaAlO_3$, in principle, it is better to use hybrids for the La *d*- and *f*-electrons. However, the hybridization

between the La *d* and O *sp* is much smaller than that for Ti, and made little difference to the energy, so it was not used for final $LaAlO_3$ DFT calculations in Chapter 5.

2.5. Bond Valence Sums

A relatively simple way to analyze the bonding and coordination of an ion is the bond valence sum (BVS) method, which assigns a bond valence (BV) to a specific bond between two ions, dependent only on the type of ions and the bond distance shown here:

$$BV = e^{\frac{R_0 - R}{b}}$$

where R is the bond distance, R_0 is a standard bond distance value specific to each type of ion-ion pair, and b is a constant found empirically, usually taken to be 0.37. The BVS for a particular ion is found by adding the BV of each bond the ion is involved in, positive BV for cations and negative BV for anions, shown here:

$$BVS_{ion} = \sum BV_{bond}$$

Resulting BVS values can be compared to formal valence charges or BVS of ions in other materials. Relative to each other, higher absolute BVS values indicate higher oxidation and higher coordination number, while lower absolute BVS values indicate higher reduction and lower coordination number.

2.6. X-ray Photoelectron Spectroscopy

X-ray photoelectron spectroscopy (XPS) is a surface-sensitive characterization tool for determining chemical species and bonding states. Monochromatic x-rays are used to eject electrons from a sample governed by the photoelectric effect, shown here:

$$BE = h\nu - KE - \varphi$$

where $h\nu$ is the energy of the incident x-ray, KE is the kinetic energy of the ejected photoelectron and what is being measured, φ is the work function specific to the spectrometer, and BE is the binding energy of the photoelectron. Elements can be identified by their binding energies because each element has a unique set of energies for electrons escaping from different orbitals. Differences in oxidation states can be readily determined from peak shifts or peak asymmetry caused by multiple peaks within one.

XPS can be made even more surface-sensitive by changing the angle between the surface normal of the sample and the detector by making the angle more grazing, thus effectively changing the sampling depth, d, by $\cos\theta$ described by the Beer-Lambert Equation:

$$I = I_0 \exp[-d/\lambda\cos\theta]$$

where I is the intensity of electrons, I_0 is the intensity of electrons from an infinitely thick sample, and λ is the attenuation length related to the inelastic mean free path of an electron in the sample. A schematic is shown in Figure 2.3 showing how the thickness of the reconstructed surface layer can be estimated using the Beer-Lambert relationship and the ratio of peak intensities.

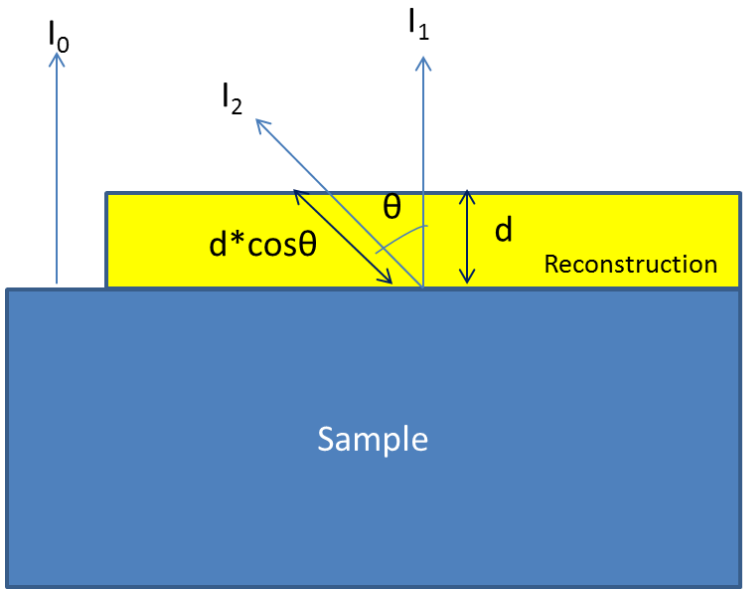

Figure 2.3**.** Schematic of reconstructed surface overlayer (yellow). The depth, *d*, can be found by measuring peak intensities at different angles.

XPS for this work was done within the Marks Group's Specimen Preparation, Evaluation, Analysis, and Reaction System (SPEAR). SPEAR is an in-house built system of UHV chambers with a base pressure of $7x10^{-11}$ Torr and includes a UHV-TEM, an XPS, an electron gun, and a heating stage. TEM samples were introduced to the system through a load lock chamber, which was subsequently baked with external heating bands to a temperature of ~200°C overnight to remove any carbonaceous material before the sample was brought into the main chamber. From there, samples were transferred to the analytical chamber, where there is an Al K-α X-ray source and PHI model 05-458 hemispherical analyzer to collect XPS data. The software, XPSPEAK 95 version 2, [48] was used to analyze the recorded XPS spectra.

3. $SrTiO_3$ Reconstructions

A large number of different reconstructions have been experimentally observed on the $SrTiO_3$ surface, including a series of (n×n) reconstructions on the (111) surface [49], (n×1) and (1×n) reconstructions on the (110) surface [50], and an even larger number for the (001) surface, namely, the (1×1) [3, 4, 51-56], (2×1) [1, 4, 56-59], (2×2) [3, 4, 56, 60-62], c(4×2) [6, 12, 58, 60], c(4×4) [4, 57, 62], (4×4) [62], c(6×2) [6, 12, 58, 59, 63], (6×2) [12], (√5×√5)R26.6º (RT5) [62, 64-67], (√13×√13)R33.7º (RT13) [59, 62], plus many more [68], which may only be locally stable, such as the (4√2×√2)R45º. Table 3.1 is a compilation of reported reconstructions that have been experimentally observed on the $SrTiO_3$ (001) surface, as well as the sample treatment and detection technique.

If there is one thing to be ascertained from Table 3.1, it is the wide array of annealing temperatures, annealing times, environments, and characterization tools with which different surface periodicities have been observed. It is not surprising that there are conflicting ideas of thought as to why these surfaces have arisen.

3.1. Strontium Adatom

The Sr adatom model for $SrTiO_3$ surface reconstructions was proposed by Kubo *et al.* when they observed a series of square cell $SrTiO_3$ (001) surface reconstructions [62]. Their $SrTiO_3$ samples were etched with a buffered NH_4F-HF (BHF) solution (pH=4.5) for 10 minutes. By doing so, the SrO is dissolved, and an atomically smooth TiO_2 terminated surface is left. They observed the $SrTiO_3$ (001) surface transitioning from the co-existence of a c(4x4) with a (2x2) at 1000ºC, to

only the c(4x4) at 1100ºC, to a (4x4) with a RT5 at 1180ºC, to only a RT5 at 1200ºC, to finally a RT13 at 1250ºC. These transitions were observed in the STM in UHV with each temperature being held only for a few seconds.

The Sr adatom model proposes one Sr adatom per surface unit cell in a four-fold oxygen coordinated position. Therefore, the transitions from one cell to another is solely caused by the diffusion of Sr adatoms on the surface. Kubo *et al.* [62] support this theory with several points. First, non-contact atomic force microscopy (NC-AFM) experiments were conducted, which are less sensitive to chemical bonding interaction, such that images reflect surface corrugations (i.e., bright spots are related to surface atomic positions while dark spots are related to the hollow positions) [64]. They observed a RT5 reconstruction with NC-AFM and scanning tunneling microscopy (STM), where a periodic arrangement of bright spots in the images was determined to be Sr or SrO clusters. This determination of Sr on the surface of the RT5-reconstructed surface led to the Sr adatom model, and was extended to the other square periodicities observed. Although not imaged with NC-AFM, bright spots in STM images were identified as Sr or SrO. In contrast, Akiyama *et al*. also imaged the RT5 reconstruction with STM and also identified Sr atoms as bright spots; however, the bright spots were confined to the domain boundaries, with very few found in the domains of the RT5 reconstruction [66].

The second case made by Kubo *et al.* [62] for the Sr adatom surface is that after etching the samples, most terrace steps observed with STM were along the [010] or [100] directions, consistent with a TiO_2 rich surface [69]. Upon heating in UHV to 1000ºC for 20 minutes, Sr clusters were reported to appear. This was confirmed by an additional anneal at 800ºC in oxygen for 30 minutes to oxidize the Sr clusters, resulting in curved terrace steps indicative of a SrO-terminated surface [69].

3.2. Oxygen Vacancy

In direct disagreement with the Sr adatom model is the oxygen vacancy model in which a TiO_2 terminated surface with oxygen vacancies was proposed by Tanaka *et al*. [65]. This disagreement between the results of Kubo *et al*. [62] and Tanaka *et al*. seems to stem from their differences in STM image interpretation. Tanaka *et al*. identified bright spots in their STM images as oxygen vacancies. Kubo *et al.*, on the other hand, identified bright spots in their STM images of the surface to be Sr or SrO clusters. Gonzalez *et al.* additionally reports oxygen vacancies as the cause for RT5 reconstruction observed with photoelectron spectroscopy and LEED. Samples were annealed in UHV for 2 hrs at 830°C [67]. Jiang *et al*., a proponent of the oxygen vacancy model, observed several reconstructions, including the 1x1, 2x1, c(4x2) and c(6x2) at high temperature in UHV as well as oxygen using a combination of LEED, auger electron spectroscopy (AES), and STM [70]. They found the higher order reconstructions, c(4x2) and c(6x2), to be terminated with a TiO_2 surface, with SrO at the surface, less stable at higher temperatures.

3.3. Double layers Reconstruction

1.1.1 3.3.1. Surface: 2x1, c(4x2), c(6x2)

Double layer (DL) reconstructions refer to $SrTiO_3$ reconstructions that are terminated on a TiO_2 bulk layer with additional TiO_2 units on top of it. The first DL $SrTiO_3$ (001) surface reconstruction to be structurally determined was the 2x1 [1], followed by the c(4x2) [58], c(6x2) [63] and the RT13 [72] (the subject of Chapter 4). For the remainder of the chapter and this work, whenever a $SrTiO_3$ reconstruction is referred to, it should be assumed that it refers to the

DL-type reconstructed structure as described here, unless noted otherwise.

Table 3.1. Observed surface reconstructions of the $SrTiO_3$ (001) surface.

Reconstruction	Sample Prep.	Temp. (K)	Atmosphere	Time (min.)	Technique
(1x1)	Sputtered	1100	UHV	60	LEED[54]
	Sputtered	900	10^{-6} mbar O_2		LEED[53]
	Sputtered	1200	UHV	few min.	LEED[49]
		873	UHV	10-120	LEED[4]
		e^- bombardment		60	LEED[57]
		973	10^{-4} mbar O_2	60	LEED[51]
	BHF etch	873	UHV	30	LEED + STM[12]
(2x1)	Sputtered	1100	10^{-5} mbar O_2		LEED[54]
	followed by:		UHV	15	
		1023-1073	HV	60	RHEED[56]
		1073	UHV	20-120	LEED[4]
	Etched	873-1073	UHV	30	LEED+STM[50]
	BHF etch	1173	10^{-2} mbar O_2	30min	STM+RHEED[69]
	Sputtered	1223-1323	flowing O_2	120-300	HREM+TED[1]
(2x2)	Sputtered	1100	10^{-5} mbar O_2		LEED[54]
	followed by:	900	UHV	15	
		1173-1223	HV	30-120	LEED[4]
		1473	UHV		STM[58]
		<973	10^{-10} mbar O_2	several hrs.	LEED[51]
	Etched	1273	UHV	20	STM[60]
c(4x2)	(2x1) + sputtering	1133	UHV	5	STM[12]
	Sputtered	1173-1673	UHV	15	LEED+STM[50]
	Sputtered	1123-1203	flowing O_2	120-300	HREM+TED[55]
	mechano-chemically polished	1100C	flowing O_2		LEED+STM[68]
	followed by:	950C	5×10^{-7}–5×10^{-5} mbar H_2	120min	
c(4x4)	(2x1)	1173-1673	UHV	30	LEED+STM[50]
	Etched	1273	UHV	20	STM[60]
(4x4)	c(4x4)	1423	UHV	several secs.	STM[60]
c(6x2)		1073-1373	flowing O_2	900	RHEED[56]
	Sputtered	1323-1373	flowing O_2	120-200	HREM+TED[61]
		1373	O_2	several hrs.	LEED[6]
c(6x2)	*followed by:*	1203	O_2	brief time	
		1223-1373	O_2	240-300	LEED+STM[70]
	followed by:	1223	UHV	120	

Reconstruction	Sample Prep.	Temp. (K)	Atmosphere	Time (min.)	Technique
	BHF etch	1223	10^{-2} mbar O_2	30min	STM+RHEED[69]
(6x2)	(2x1) + sputtering	1248	UHV	10	STM[12]
(√5x√5)R26.6°	(4x4)	1453-1473	UHV	several secs.	STM[60]
		1473	UHV	2	STM[71]
	Etched	1273	UHV	several secs.	STM+AFM[62]
		1073	UHV	30	STM[64]
		1458	UHV	2	
		1103	UHV	120	LEED[65]
(√13x√13)R33.7°		1073-1373	flowing O_2	900	RHEED[56]
	(√5x√5)R26.6°	1523	UHV	several secs.	STM[60]
	Sputtered + etched	1323	flowing O_2	300	TED[72]

The 2x1 reconstruction reported by Erdman *et al.* was formed at 950-1050°C under oxidizing conditions and solved with a combination of TED, DM, and DFT [1]. An atomic structure representation is shown in Figure 3.1, with the 2x1 repeating cell outlined. It is terminated with two layers of TiO_2 and its characteristic feature is a "zigzag" motif. The surface Ti are bonded to 5 oxygen at the surface, shown by green TiO_5 polyhedra and 6 oxygen in the bulk, shown by purple octahedra.

Similarly, a DL c(4x2) reconstruction was also solved by Erdman *et al.* in a similar manner and formed at 850-930°C under oxidizing conditions [58]. Figure 3.2 shows the top view of the reconstruction with a black line indicating the surface unit cell. The 2x1 and c(4x2) are very similar, not only in their stoichiometry, but also in the fact that a simple rearrangement of a Ti atom position is the only difference between the two structures.

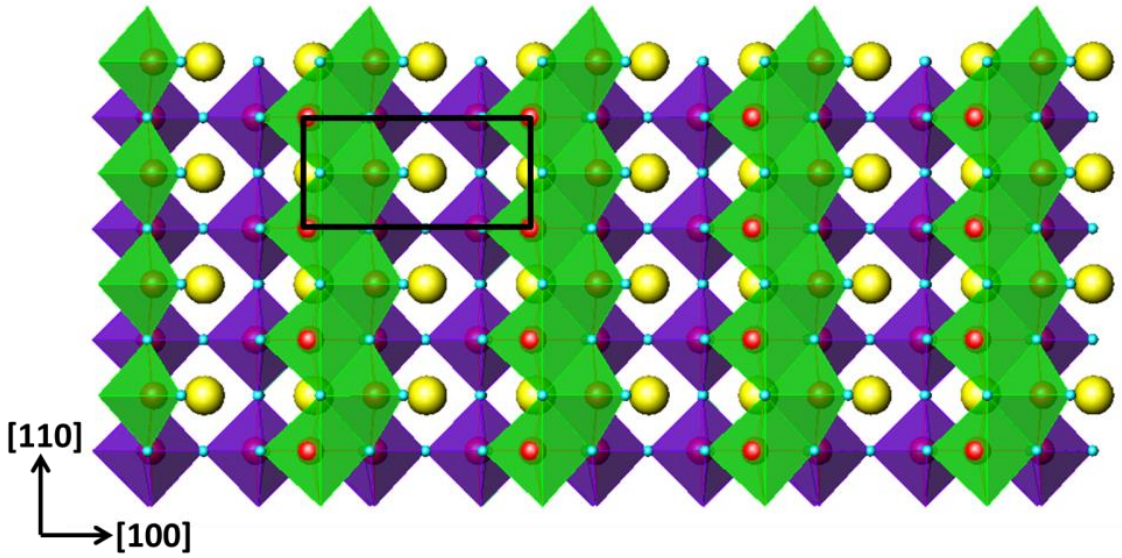

Figure 3.1. Top view of the $SrTiO_3$ (001) 2x1-DL reconstruction. Red are Ti, yellow are Sr and blue are O. Green polyhedra represent TiO_5 units, Blue are TiO_6 units.

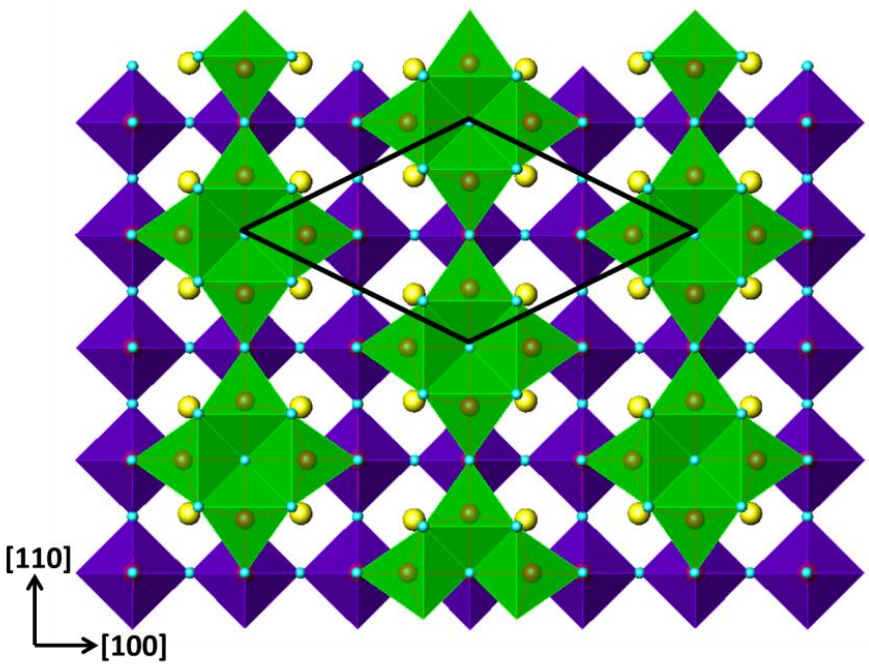

Figure 3.2. Top view of the $SrTiO_3$ (001) c(4x2) reconstruction. Red are Ti, yellow are Sr and blue are O. Green polyhedra represent TiO_5 units, Blue are TiO_6 units.

The c(6x2) structure, solved by Lanier *et al.* by a similar experimental method and formed at temperatures between 1050-1100°C in oxidizing conditions, is a more complex structure made up of four microscopic structurally-similar motifs with additional non-periodic TiO_2 units at the surface [63]. The surface is a random mixture of the motifs, but each motif itself has short-range order. Determining the c(6x2) structure required using both TED and surface X-ray diffraction to find Ti positions. Like the 2x1 and c(4x2), the surface is terminated with a Ti_yO_x layer. Unlike the 2x1 and c(4x2), the c(6x2) has more than one TiO_2 unit above a bulk TiO_2 layer. It also contains both 5- and 4-fold coordinated Ti atoms, while the 2x1 and c(4x2) only have 5-fold coordinated Ti atoms at the surface. The most striking difference is the fact that the c(6x2) reconstruction is composed of multiple related, but different, structural domains, while the c(4x2) and 2x1 reconstructions are single-structure surfaces.

The fourth DL model, to be presented in chapter 4, is the RT13 reconstruction. The similarity in structures consisting of TiO_x units at the surface is also not surprising when considering the overlapping temperature and time domains that each are formed. When annealing in the temperature range of 850-1050°C, Enterkin observed the 2x1, c(4x2), and RT13 to form. At 850°C, either the 2x1 or RT13 will form, with the RT13 being more common, while at 950°C all three can form, with the 2x1 being most common. It has even been observed that two samples annealed together can form the 2x1 on one sample and RT13 on the other [73]. It is apparent that the temperature is not the sole factor governing the surface structure outcome, nor is the annealing environment (see Table 3.1). Other factors, such as local variation in stoichiometry at the surface, kinetic pathways for surface diffusion, and sample preparation, can also contribute.

3.3.2. 2x2

The 2x2 reconstruction discussed here was one of three 2x2-type reconstructions presented by Warschkow *et al.*, and evaluated with DFT as having the lowest surface energy of the three [74]. This 2x2 was later observed experimentally in co-existence with 2x1 by Herger *et al.* using surface X-ray diffraction. Figure 3.3 shows the top view of the 2x2 reconstruction, which displays a "zigzag" like the 2x1, can also be considered as alternating domains of the 2x1. Herger *et al.* looked at a $SrTiO_3$ single crystal sample that had been chemically and thermally etched to give a TiO_2 terminated surface [75]. The resulting surface area was found to be a mixture of 43% 2x2, 37% 2x1, and 20% 1x1 relaxation. When considering the 2x2 as two disordered 2x1 domains, the sample surface could be said to be 80% occupied by 2x1 domains.

3.3.3. (√2x√2)R45°

The (√2x√2)R45° (RT2) reconstruction is a theoretical surface reconstruction proposed by Warschkow *et al.* [74] with the same stoichiometry as the 2x1 and c(4x2). Although it has never been experimentally observed, the surface energy of RT2 is significantly lower relative to that of the 2x1 and c4x2, each of which, have similar surface energies. The structure is shown in Figure 3.4 and can be characterized as diagonal lines running parallel to the [100] direction. Qualitatively, it easy to see the difference between the "straight line" structure of the RT2 versus the "zig-zag line" of the experimentally observed 2x1.

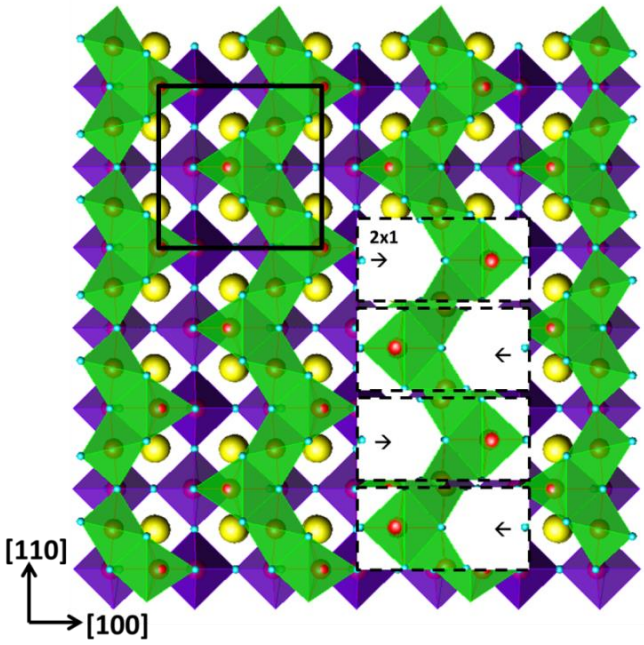

Figure 3.3**.** Top view of $SrTiO_3$ (001) 2x2 reconstruction with surface unit cell outlined in black in upper left corner. The 2x2 can be thought of as alternating 2x1 cells (overlaid). Red are Ti, yellow are Sr and blue are O. Green polyhedra represent TiO_5 units, Blue are TiO_6 units.

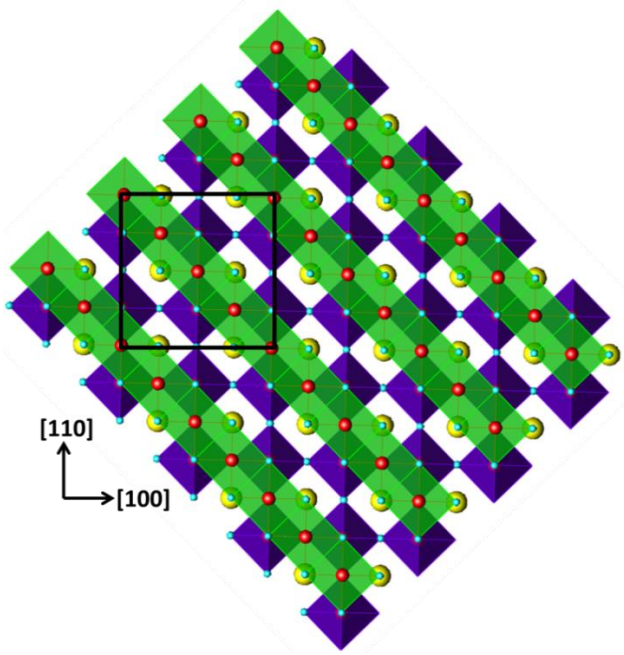

Figure 3.4. Top view of the $SrTiO_3$ (001) RT2 theoretical surface reconstruction. Red are Ti, yellow are Sr and blue are O. Green polyhedra represent TiO_5 units, Blue are TiO_6 units.

3.3.4. $SrTiO_3$ (110)

The polar (110) surface of $SrTiO_3$ has also been observed to exhibit a wide range of periodic surface reconstructions, even with the lesser amount of literature devoted to the surface relative to the (001). A series of nx1 reconstructions, including 3x1, 4x1, and 6x1 periodicities formed by annealing in UHV, was seen by Russel *et al.* via STM and LEED [76]. A 3x1 is formed first at a temperature of 875°C held for 2 hr, with a small amount of 1x4 faintly seen confined to [001] step edges. Then as the temperature is raised, the 3x1 coexists with a 4x1 until 1175°C is reached and held for 2 hr, whereupon the surface fully transitions to 4x1. Further annealing at 1275°C for 2 hr produces a 6x1, with 2x1 domains faintly observed only at terrace edges. The nx1 reconstructions were all found to be oxygen-deficient, which is not surprising since they were annealed in UHV. The 4x1 showed Ti-enrichment and the 6x1 showed Sr-enrichment. Wang *et al.* reported observing the 5x1, 4x1, 2x8, and 6x8 with STM and XPS, whose existences were determined by the Ti/Sr concentration [77]. They were able to change the concentration by evaporating Ti or Sr metal on the surface. With increasing Ti concentration, the reconstructions evolved from 5x1 to 4x1, to 2x8, to 6x8, and were found to be reversible by increasing the Sr concentration. The annealing temperature and time used was 1000°C for less than 1 hr.

Enterkin *et al.* observed a 3x1 concurrent with a 1x4 reconstruction at step edges via TEM after annealing at 1000°C, and recorded TED data, which were used to determine the 3x1 structure [50]. It is comprised of corner-sharing TiO_4 tetrahedra, arranged into six-and eight-member rings. Tetrahedra in the 6-member ring share corners with three other surface tetrahedra and one sub-surface bulk TiO_6. The two tetrahedra that are only in the eight-member ring corner-share with two other surface tetrahedra and edge-share with one sub-surface TiO_6. By varying the number of TiO_4 units in the larger ring, reconstructions with 2x1, 4x1, 5x1, 6x1, etc., can be

formed, thus creating a homologous series shown in Figure 3.5 that was confirmed with DFT and STM. As *n* increases, the TiO_2 surface excess decreases. The relationship of these reconstructions to one another can explain why Russell *et. al.* observed the 3x1, 4x1, 6x1, and to some extent the 2x1, all either in co-existence or in series.

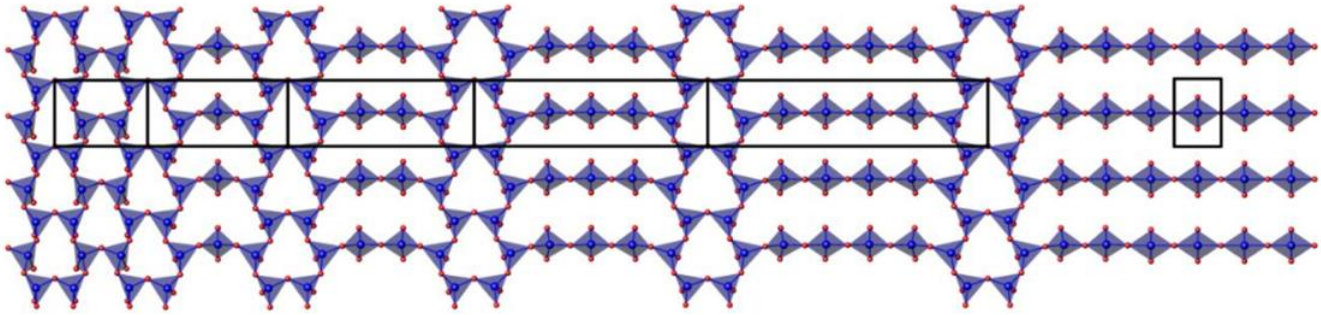

Figure 3.5**.** Surface layer for the homologous series of $SrTiO_3$ (110) reconstructions taken from [50]. Black boxes indicate surface cell, left to right is the 2x1, 3x1, 4x1, 5x1, 6x1, and ∞x1.

3.4. Conclusions

The emerging theme of the DL reconstructions is that the surface can be considered as a network of corner- or edge-sharing TiO_x units in varying stoichiometries. The network can range from ordered to pseudo-ordered, like the c(6x2), to a disordered glass-like surface layer made up of TiO_x units. In all cases, there are additional surface Ti atoms that are under-coordinated relative to bulk Ti, which are octahedrally coordinated to six oxygen atoms. Although the STO (110) 3x1 reconstruction is not technically a DL, it does have a network of TiO_4 tetrahedra. The under-coordination of Ti results in slightly shorter Ti-O bond lengths and more covalent bonds. Under oxidizing conditions, it can be expected that the surface will exist in varying states of disordered TiO_x units and, when annealed, the local stoichiometry and kinetics (as well as sample

preparation details) will dictate what reconstruction is formed.

4. $SrTiO_3$ (001) (√13×√13)R33.7º Surface Reconstruction

4.1. Introduction

This chapter presents a structural solution of the (√13×√13)R33.7º (RT13) (001) reconstruction using transmission electron microscopy (TEM) supported by relatively high-level DFT calculations. Similar to the (110) surface, this is a valence-neutral surface, but with TiO_5 in a more open structure, as dictated by the topology of the underlying bulk structure. Some other candidate valence-neutral surface structures with similar elements, such as the (√5×√5)R26.6º (RT5), were also identified. There are many others, all with relatively similar surface energies, that could occur locally, consistent with the plethora of observed structures. These surfaces are best considered as 2D analogues of bulk SiO_2 glass, consistent with the original concept of network glasses proposed by Zachariasen [78], where one can have ordered and disordered structures, all preserving local co-ordination and bond-valence sums [50]. Even with accounting for topological constraints of the underlying bulk structure, as well as the requirement of valence neutrality, many different, but fundamentally similar local structures can be obtained for both the (001) and (110) surfaces, and presumably other perovskite surfaces, possibly including interfaces.

4.2. Background

The $SrTiO_3$ (001) RT13 reconstruction has previously been reported by Naito *et al.* via reflection high-energy electron diffraction (RHEED), but only in conjunction with c(6x2) domains [59]. The experimental conditions included cleaning by ultrasonic agitation in an organic solvent and

annealing in flowing oxygen for 15 hours at temperatures ranging from 800 to 1100ºC. They characterize the RT13 reconstructed surface as "flat," but do not offer any explanations as to why the surface is formed, or if the surface is Ti-rich or Sr-rich. In contrast, Kubo *et al.* observed the RT13 with scanning tunneling microscopy (STM) after etching with a BHF to remove SrO and leave a TiO_2 surface, followed by annealing at 1250ºC in UHV for a few seconds [62]. Not only was the RT13 observed, it was the final reconstruction after observing a series of reconstructions beginning with the co-existence of a c(4x4) and a 2x2 at 1000ºC transitioning to only a c(4x4) at 1100ºC, to a 4x4 with a (√5x√5)R26.6º at 1180ºC, to only a (√5x√5)R26.6º at 1200ºC to finally, the (√13x√13)R33.7º at 1250ºC. Kubo *et al.* proposed the Sr adatom model, wherein each reconstruction consists of one Sr atom atop a bulk TiO_2 termination.

However, there are many other ways one can obtain similar STM images, so only considering two different structures is not a structure solution. In addition, via basic chemical reasoning a relatively exposed Sr atom sitting on a surface is highly unlikely, as Sr is much more basic than Ti.

4.3. Experimental

Single crystal $SrTiO_3$ (001) (99.95% purity) substrates were purchased from MTI Corporation (Richmond, CA) and conventionally prepared for TEM by methods detailed in Chapter 2. Additionally, samples were etched with a NH_4F-HF solution (pH 5) for 45 seconds to preferentially remove SrO, then annealed in a tube furnace with flowing oxygen (100 sccm) for 5 hours at 1050°C to produce the air stable RT13 reconstruction. As will be shown, this preparation method led to surfaces with a lower TiO_2 excess, thereby allowing different reconstructions to be accessed. The experimental treatment procedure used was that of S.

Christensen of the Bedzyk group at Northwestern University, who was able to consistently obtain the RT13 reconstruction [79]. However, the need of a buffered HF etching may be superfluous because J. Enterkin was able to observe the RT13 reconstruction without etching, only annealing in oxygen [73].

TEM images and off-zone diffraction patterns were taken before etching and after annealing with a Hitachi 8100 TEM operating at 200 kV. Diffraction patterns were recorded with film for a range of exposure times (2-90 seconds) and digitized with an Optronics P-1000 microdensitometer. Spot intensities from both domains were measured using a cross-correlation technique [80] and merged to create a single data set. The data set was reduced by *p4* plane-group symmetry to 43 independent beams. Electron Direct Methods software (EDM 3.0) [33] was implemented to generate 2D scattering potential maps of possible surface structures.

Density functional theory (DFT) was used to obtain atomic positions in the out-of-plane direction that cannot be determined from the scattering potential map, as well as to check the validity of in-plane positions, and calculate the energy of the surface. A 3D periodic surface slab model was created using the in-plane DFT-optimized bulk lattice parameters and 7 layers of $SrTiO_3$ bulk (412 atoms) separated by 10 Å of vacuum. Atomic positions were optimized using the full-electron potential WIEN2k package [38] with an augmented plane wave + local orbitals (APW+lo) basis set, the PBEsol [41] generalized gradient approximation as well as the revTPSS method [46]. Similar to work for the NiO (111) surface [81], the exact-exchange parameter for the Ti-d levels was optimized using experimental energies of some TiO_x molecules [82], which gave a result of 0.5. While this is not a panacea of all DFT ills, and the exact-exchange fraction is surprisingly large, this gave a noticeably better value of 1.36 eV for the decomposition energy of $SrTiO_3$ to SrO and TiO_2, compared to previous work [32], a better band-gap of ~2.8(1) eV as

well as a good absolute fit to the ratio of the surface free-energy of $SrTiO_3$ (001) to (110) from Wulff construction measurements [73], none of these being part of the fitting. Typical muffin-tin radii were 1.55, 1.75, and 2.36 Bohr for O, Ti, and Sr, respectively, a 1x1x1 *k*-point grid, and a plane wave cut-off of K_{max}*min(RMT) = 7.0. Other known (001) surface structures were calculated for comparison with similar parameters, excepting the *k*-point sampling which was kept at the same inverse volume density. The surface energy per (1×1) surface unit cell (E_{surf}) was calculated as:

$$E_{surf}=(E_{slab}-E_{STO}*N_{STO}-E_{TO}*N_{TO})/(2*N_{1x1}),$$

where E_{slab} is the total energy of the slab, E_{STO} the energy of bulk $SrTiO_3$, N_{STO}, the number of bulk $SrTiO_3$ unit cells, E_{TO}, the energy of bulk rutile TiO_2, N_{TO}, the number of excess TiO_2 units, and $N_{1\times1}$, the number of (1×1) surface cells. A reasonable estimation of 0.05 eV/(1×1) cell was used for revTPSS DFT error.

4.4. Results

Imaging RT13 samples show a well-ordered surface with faceting along the <010> and <100> directions, indicative of a TiO_2-terminated surface [34], as expected when using a BHF etchant (see Figure 4.1). Figure 4.2 shows a typical off-zone diffraction pattern, with the two domains of the RT13 marked in addition to the bulk (1×1) cell. The RT13 reconstruction was observed in areas of several microns squared and never in the presence of another reconstruction.

Figure 4.1. Dark field TEM image showing surface faceting along <010> and <100> directions and reconstructed step surfaces.

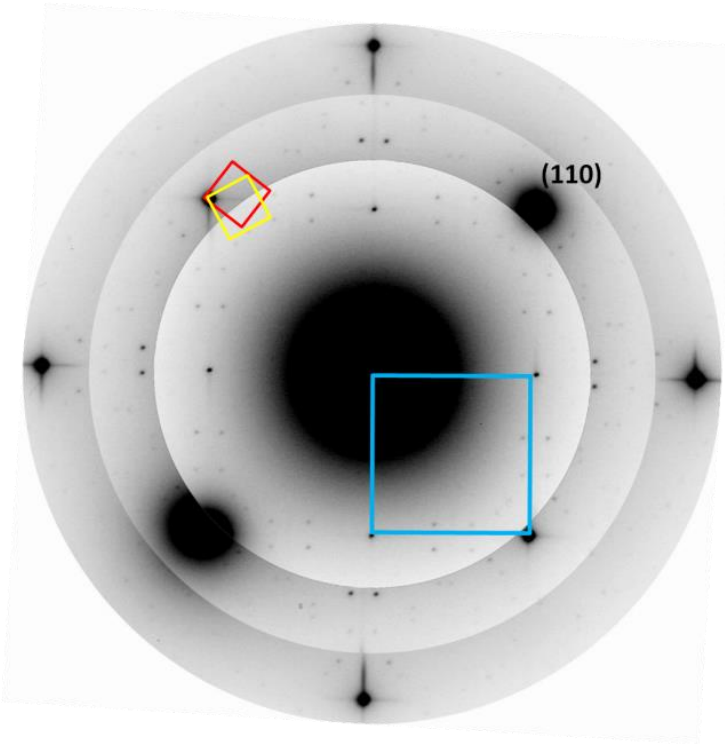

Figure 4.2. Off-zone TEM diffraction pattern of RT13 with outlined bulk surface cell (blue) and two domains of RT13 (red, yellow).

An EDM analysis resulted in only one feasible scattering potential map shown in Figure 4.3. The final DFT-optimized atomic surface structure is overlaid the map, qualitatively showing high agreement between Ti positions refined with EDM versus DFT. A quantitative comparison of Ti atom positions is shown in Table 4.1. When refined against experimental data, in-plane atomic positions, with a global temperature factor, gave χ^2=3.37 and R_1=0.25, presented in Table 4.2. These numbers are slightly high, but with only 43 reflections, adding too many additional parameters is not justifiable even if it reduces the R_1.

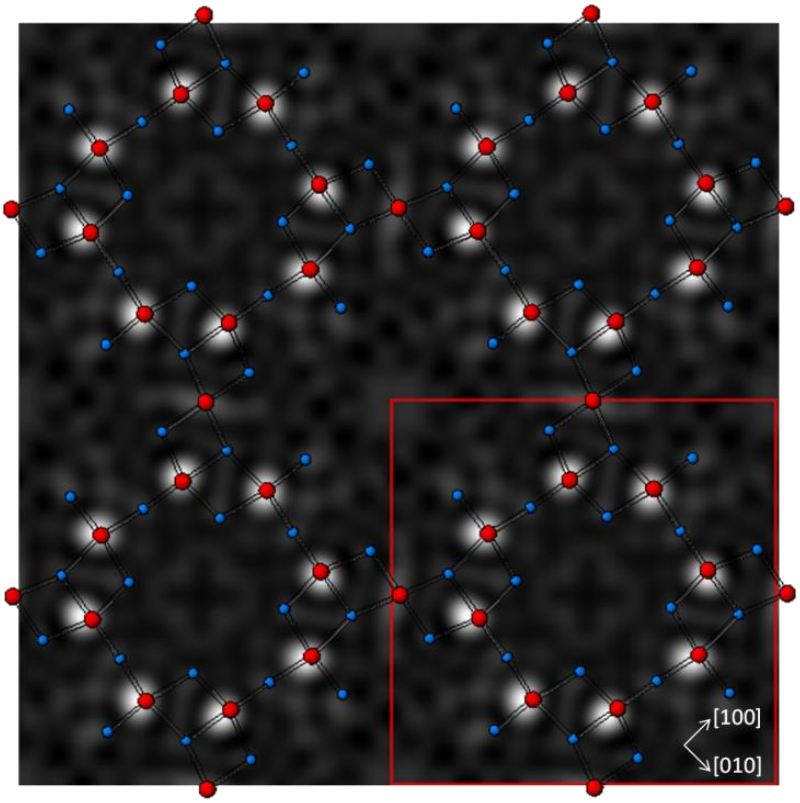

Figure 4.3. Geometrically relaxed RT13 atomic surface layer overlaid scattering potential map solution obtained from EDM showing agreement with DFT structural results. Ti (red), O (blue).

Table 4.1 Comparison of atom positions for RT13 surface Ti in fractional coordinates of the surface cell found through EDM and refined with DFT.

	EDM		DFT		Difference in
Atom	X	y	X	y	Position (Å)
Ti1	0.0000	0.5000	0.0000	0.5000	0.0000
Ti2	0.4439	0.1885	0.4394	0.2047	0.0012
Ti3	0.2297	0.3334	0.2285	0.3429	0.0007
O4	0.3834	0.0558	0.3871	0.0761	0.0015
O5	0.3462	0.2607	0.3378	0.2754	0.0012
O6	0.1415	0.2478	0.1495	0.2432	0.0007
O7	0.3353	0.4584	0.2997	0.4647	0.0026
O8	0.1130	0.4448	0.1256	0.4466	0.0009

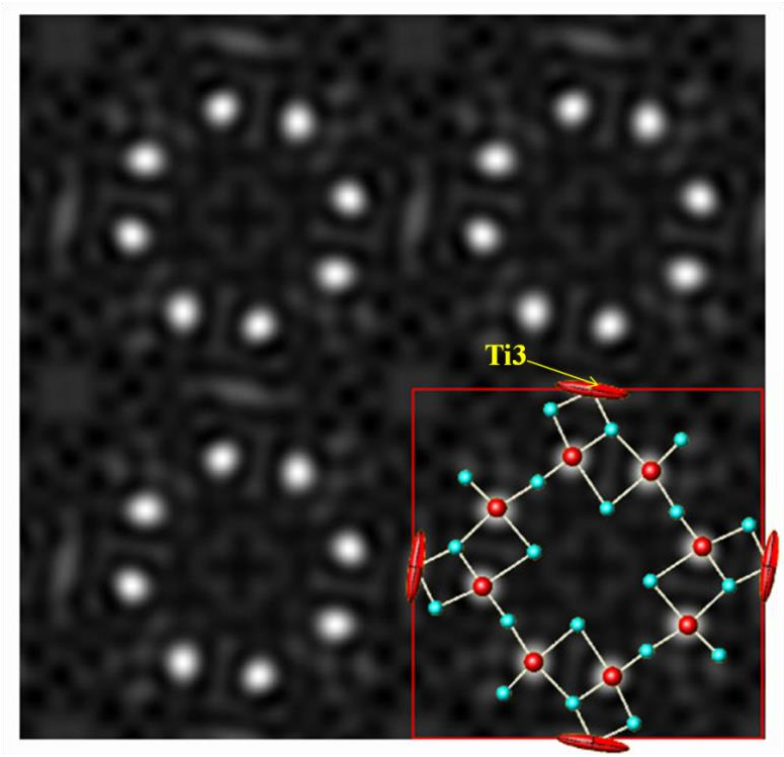

Figure 4.4. Geometrically relaxed RT13 atomic surface layer overlaid scattering potential map solution obtained from direct methods. Anisotropic temperature factors were calculated from SHELXL [80] for Ti3. The ellipsoid shape shows disorder at Ti3's position. Ti are larger (red), O are smaller (blue).

Table 4.2 Observed, $|F_{hk0}|$obs, and calculated, $|F_{hk0}|$calc, amplitudes for each measured reflection, (h,k,0), the difference between observed and calculated amplitudes (Diff), and error (σ) from RT13 TEM diffraction pattern.

H	***k***	$\|F_{hk0}\|$**obs**	$\|F_{hk0}\|$**calc**	**Diff**	**Σ**
2	1	5.4	5.6	0.1	0.5
2	2	3.6	5.4	1.8	0.4
3	0	3.9	4.4	0.6	0.3
0	3	3.9	4.4	0.6	0.3
1	3	3.8	2.7	1.1	0.5
3	1	3.9	4.2	0.2	0.5
0	4	8.1	7.7	0.4	0.4
4	0	8.1	7.7	0.4	0.4
4	1	9.4	1.5	8.0	2.7
1	4	9.5	8.3	1.2	2.7
3	3	2.4	2.4	0.0	0.2
2	4	5.9	2.9	3.0	1.9
4	2	5.9	7.8	1.9	2.0
0	5	8.4	8.4	0.0	0.3
4	3	10.0	8.8	1.2	5.1
3	4	9.4	15.6	6.2	4.9
5	0	8.4	8.4	0.0	0.3
5	1	4.8	11.5	6.6	0.2
1	5	5.0	6.1	1.1	0.2
5	2	5.6	5.6	0.0	0.3
2	5	5.5	5.5	0.0	0.4
4	4	5.1	5.2	0.1	0.4
5	3	4.4	5.9	1.5	1.0
3	5	4.5	7.8	3.3	1.0
0	6	4.1	4.1	0.0	0.2
6	0	4.1	4.1	0.0	0.2
1	6	3.6	3.7	0.2	0.5
6	1	3.4	1.0	2.4	0.5
2	6	3.6	1.4	2.2	0.9
6	2	3.4	3.3	0.2	1.0
5	4	5.8	6.2	0.4	2.3
4	5	5.6	0.8	4.8	2.4
3	6	3.8	3.8	0.0	0.3
6	3	4.0	2.4	1.6	0.3
7	0	2.8	2.8	0.0	0.3
0	7	2.8	2.8	0.0	0.3
5	5	2.7	2.7	0.0	0.3
1	7	3.5	2.8	0.7	1.2
7	1	3.5	2.6	0.9	1.1
2	7	3.1	3.1	0.0	0.5
7	2	3.1	6.7	3.6	0.5
3	7	3.6	3.0	0.6	0.4
7	3	3.6	3.6	0.0	0.5
Robust	$\chi^2_=$	3.37	R_1=	0.25	

As a test, SHELXL [83] was used, and with the addition of anisotropic temperature factors, R_1 decreased by 14%. This is suggestive of a rotation of the Ti atom located at the edge of surface unit cell (Ti3), which is consistent both with the EDM map (showing a streak at this site) as well as being the type of disorder expected if there are surface defects, and for the lowest-energy phonon mode (which will involve alternate rotations within a c(2×2) supercell) (See Figure 4.4). For completeness, there was no indication of reduced occupancy of the Ti3 site. Since maps do not provide registry information and O sites are hard to determine from the maps alone, it was assumed that Ti atoms were bonded to O atoms in the layer immediately beneath the surface (subsurface layer), verified later by DFT.

The RT13 structure (Figure 4.5) has ten TiO_5 polyhedra units that share edges with TiO_6 octahedra located in the subsurface. There is also one TiO_5 unit in the subsurface that remains corner-sharing with neighboring octahedra and is stabilized by rotations of the octahedra in the bulk beneath them. Ti-O bond distances in the surface TiO_5 units are comparable to those in the bulk while, unsurprisingly, Ti-O bonds from surface Ti to subsurface O are slightly smaller than those in bulk (1.89 vs. 1.97 Å, See Table 4.3). The in-plane positions of surface atoms remained in excellent agreement with those found by EDM, as well as having all surface bond-valence sums close to 2- for O and 4+ for Ti, as expected for a stable structure [50] (see Table 4.4).

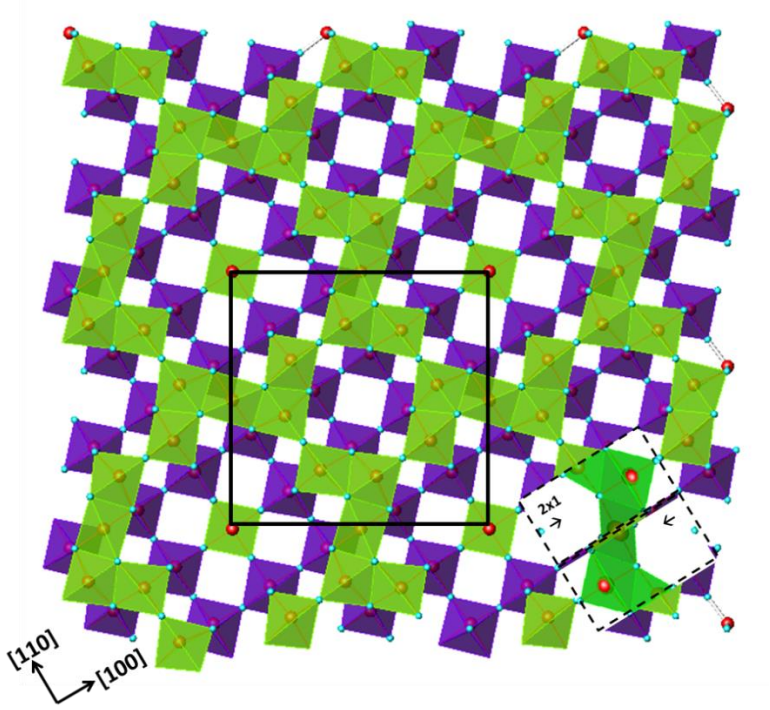

Figure 4.5. Top view of RT13 with TiO_6 octahedra (purple) and TiO_5 polyhedra (green). The reconstruction also affects the next few layers beneath it as shown by slight rotations of the octahedral. TiO_5 unit in the center is in the subsurface layer. Ti (red), Sr (yellow), O (blue).

Table 4.3. Bond distances between Ti and O on the RT13 surface and bulk.

Bond	Type	Length (Å)
Ti1-O4	Surface-Surface	1.94
Ti1-O8	Surface-Surface	2.01
Ti1-O15	Surface-Bulk	1.86
Ti2-O4	Surface-Surface	1.98
Ti2-O5	Surface-Surface	1.85
Ti2-O7	Surface-Surface	1.92
Ti2-O8	Surface-Surface	2.05
Ti2-O13	Surface-Bulk	1.89
Ti3-O5	Surface-Surface	1.90
Ti3-O6	Surface-Surface	1.82
Ti3-O7	Surface-Surface	2.01
Ti3-O8	Surface-Surface	2.14
Ti3-O14	Surface-Bulk	1.91
Average	Surface-Surface	1.96
Average	Surface-Bulk	1.89
Average Ti-O in bulk $SrTiO_3$		1.97

Table 4.4. List of bond valence sums for surface Ti and O for RT13 and for bulk $SrTiO_3$. Calculated with Kalvados

Atom	Location	Bond Valence Sum
Ti1	Surface	3.66
Ti2	Surface	3.84
Ti3	Surface	3.72
O4	Surface	-2.04
O5	Surface	-1.79
O6	Surface	-1.89
O7	Surface	-2.06
O8	Surface	-1.63
O13	Subsurface	-2.04
O14	Subsurface	-2.02
O15	Subsurface	-1.97
Ti16	Subsurface	4.16
Ti17	Subsurface	4.14
Ti18	Subsurface	4.19
Ti19	Subsurface	4.15
Bulk Ti in $SrTiO_3$		4.14
Bulk O in $SrTiO_3$		-2.08

The surface energies for RT13 along with other DL surfaces are plotted in Figure 4.6, with the convex-hull line marked indicating the lowest energy configurations as a function of excess TiO_2. For each structure with the same composition, the energy can be compared directly, and the lower energy structure is thermodynamically the most stable. For structures of different compositions, this is not valid and the convex hull line is used. If, for example, surface structure A with one excess TiO_2 unit per 1x1 cell and structure B with two excess TiO_2/1x1 are known and their surface energies are plotted, structure C with 1.5 excess TiO_2/1x1 is thermodynamically stable if its energy lies on or below the line connecting the energies of A and B. In Figure 4.6, the $(\sqrt{2}\times\sqrt{2})R45°$ (RT2) is included on the graph for completeness, and although it has the lowest

energy for a surface with 1.5 excess TiO_2 per bulk (1×1), since it has never been observed experimentally, only theoretically [74], unlike the higher energy c(4×2) and (2×2), the latter were used for the convex hull. In this case, the energy of the RT13 surface is well below a line between 1x1Sr and RT2 or the 2x2, making it a feasible surface for 1.115 excess TiO_2 per bulk (1×1).

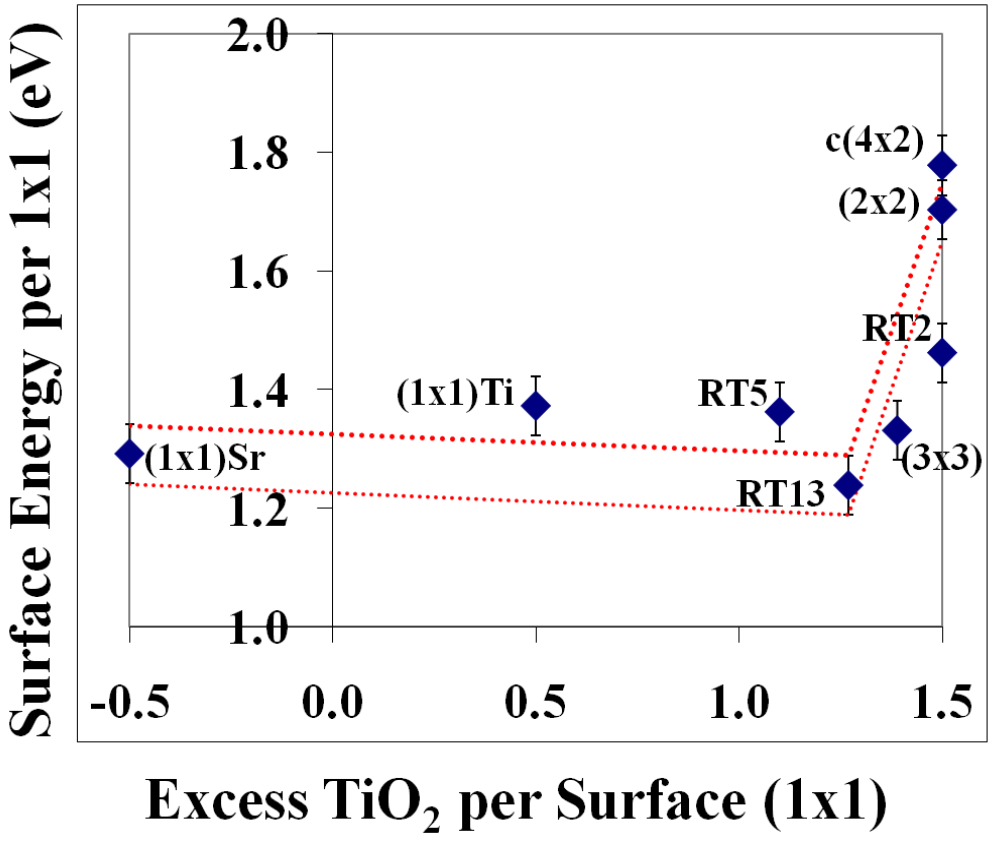

Figure 4.6. Surface energies in eV per (1×1) cell versus number of TiO_2 units per $SrTiO_3$ (1x1) surface unit cell for various $SrTiO_3$ (001) reconstructions. Region between dotted (red) lines shows convex-hull (including DFT error estimate) connecting the lowest energy surface pathway. $SrTiO_3$ (001) theoretical reconstructions, RT5 and (3×3), fall close to the convex hull.

4.5. Discussion

The RT13 surface, shown in Figure 4.5, can be considered an ordered network of corner and edge-sharing TiO_5 units, similar to other DL $SrTiO_3$ (001) surfaces but now in a more open network of rings. One can build an almost endless sequence of such structures by changing the number of each type of unit, both regularly to form an ordered reconstruction or semi-randomly to form a 2D glass. Overlaid the on RT13 surface in Figure 4.5 are two opposite direction domains of the DL 2x1 (or alternatively, one 2x2 domain) illustrating the fact that the RT13 can be assembled from these smaller celled 2x1 units, albeit with 90 degree rotations. Because of the fundamental similarities between the DL structures, it is not surprising that many of them co-exist or are precursors to other reconstructions. Beyond the RT13, one can generate very similar structures with a single-layer of TiO_2 on top of a bulk SrO termination (rather than bulk TiO_2 for DL's), or use combinations of the building blocks in other fashions.

As an example, we have constructed and calculated the structures of two smaller square cell "ring" reconstructions. The smaller of the two is the RT5 reconstruction shown in Figure 4.7 made up of larger rings of 8 Ti polyhedra and smaller rings of 4 Ti polyhedra. The rings consist of half TiO_4 tetrahedra and half TiO_5 polyhedra connected by corner-sharing. The second, shown in Figure 4.8, is a (3×3) reconstruction consisting of a ring of 8 TiO_5 polyhedra linked together, alternating between corner-sharing and edge-sharing. The RT5 and 3x3 surface energies are included in Figure 4.6 and lie near the convex hull line indicating their feasibility.

Continuing the "ring" series, the next smaller reconstruction is a 2x2 surface unit cell where the "ring" of polyhedra has closed in and now is a group of four edge-sharing TiO_5 units exactly like the features of the c(4x2), except not staggered. The group of 4 TiO_5 link to the

group in the next cell in the *x*- and *y*-direction by corner-sharing; the c(4x2) only connects in the *y*-direction, creating columns of TiO_5 groups that are shifted half a cell every other column. This DL 2x2 in the "ring" series is quite a different structure from the DL 2x2 "zigzag" discussed in Chapter 3, and has higher, 4-fold rotation symmetry in the surface plane. Lin *et al.* simulated STM images for both DL 2x2 reconstructions along with others, and found the "ring" 2x2 matches their experimental STM images better than the "zigzag" [84]; however, this does not negate the existence of the "zigzag" 2x2, which has been experimentally observed [75] and theoretically calculated to have the lowest surface energy of any 2x2 reconstruction [74]. Continuing to shrink the square surface unit cell to a RT2 and fitting the group of four TiO_5 on the four available sites above oxygen results in a 1x1 DL.

Conversely, larger surface unit cells with larger rings of TiO_5 can be constructed as well, although the only reconstruction with a larger surface area than a RT13 that has been experimentally observed is a 4x4 [62]. As the rings are enlarged with more units, it seems more likely that they would devolve into more stable configurations, like the "zigzag" 2x1 or 2x2 domains.

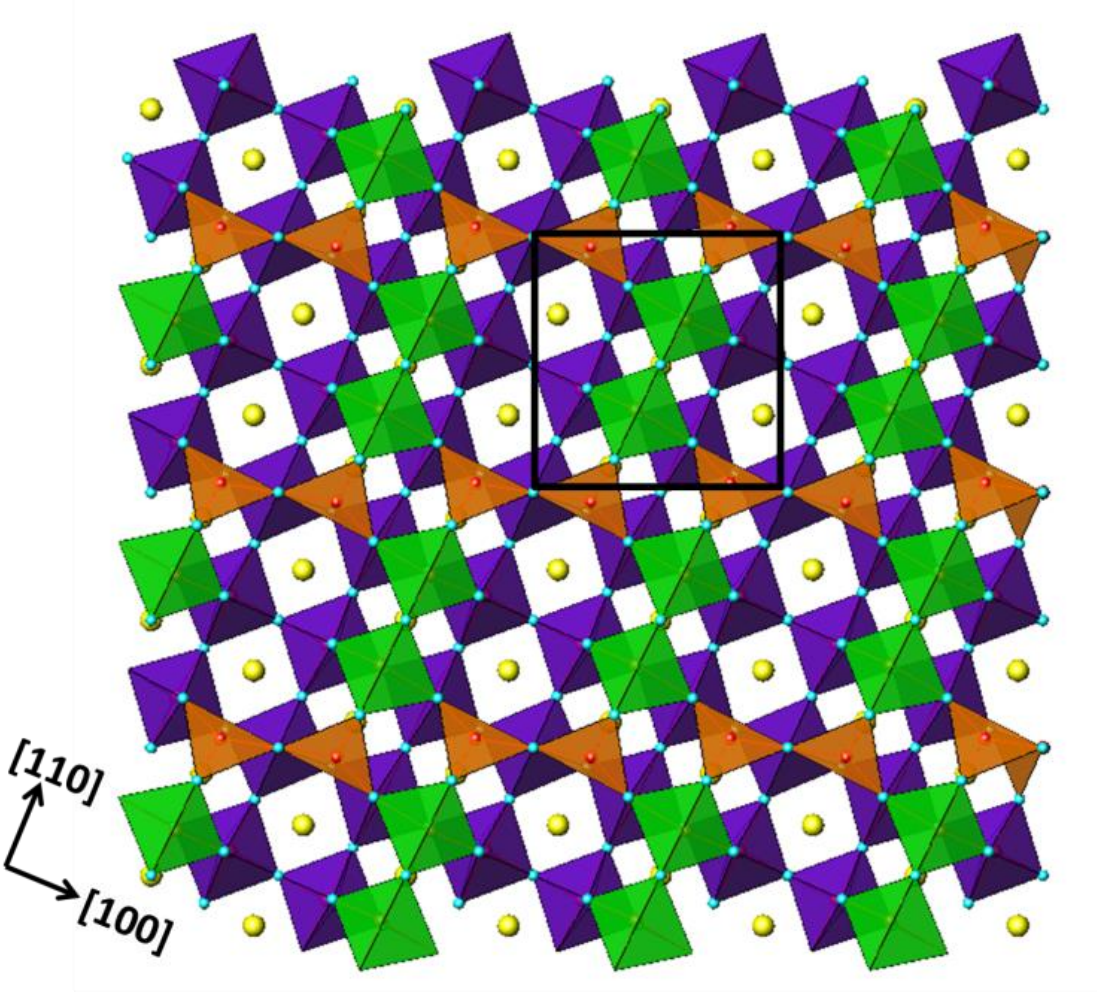

Figure 4.7. Top view (left) of proposed $SrTiO_3$ (001) RT5 surface reconstruction. Orange, green and purple polyhedra show Ti coordinated with 4, 5, and 6 oxygen, respectively. Ti, O, and Sr atoms are shown in red, blue, and yellow, respectively.

However, with relatively sluggish surface diffusion kinetics, surface reordering may not be possible unless given enough energy, typically after longer times and higher temperatures, than used in many experimental studies. We believe that the $SrTiO_3$ surface typically exists as a disordered or semi-ordered 2D network of TiO_x similar to the Si-Au (111) 6×6 structure, which has pentagonal units in a pseudo-glass structure [85], shown recently to be related to a Au-Si eutectic liquid interface structure [86]. Additionally, we suspect that the pseudo-glass surface

network is probably common to all perovskite oxide surfaces and perhaps interfaces. For example, the interface of $SrTiO_3$ and $LaAlO_3$ has been found to give rise to conductive properties [87-89] due to oxygen vacancies, structural deformations, and electronic interface reconstruction, which is not what would be predicted for two insulating materials. Understanding the structure and being able to control the disorder at interfaces such as the $SrTiO_3/LaAlO_3$ interface has powerful implications for novel electronic devices.

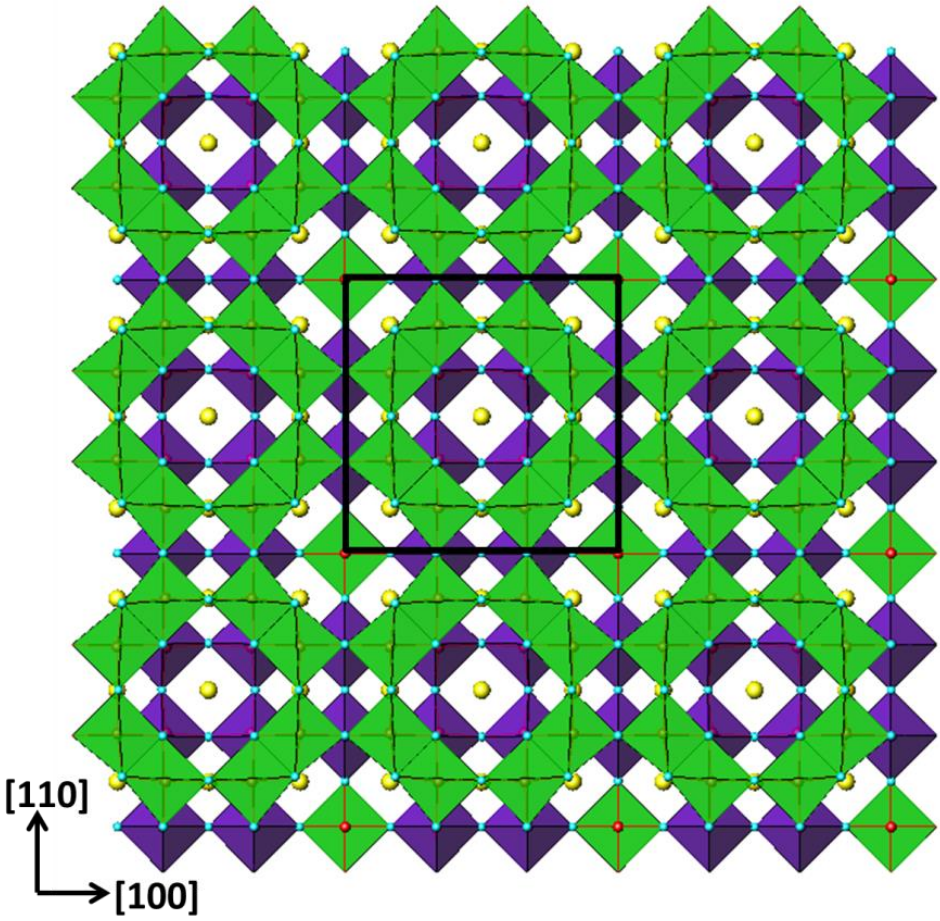

Figure 4.8. Top view of proposed $SrTiO_3$ (001) 3x3 surface reconstruction. Green and purple polyhedra show Ti coordinated with 5 and 6 oxygen, respectively. Ti, O, and Sr atoms are shown in red, blue, and yellow, respectively.

4.6. Conclusions

Pulling together the arguments presented above of how these different structures can be generated by tiling of locally bond-valence satisfied units, as well as the relatively small differences in the surface energies found from the DFT calculations, a consistent picture is starting to emerge. Depending upon exact details of how the surfaces are prepared, as well as local compositional inhomogeneities and the entropy of mixing, numerous structures can coexist locally, as well as, disordered glass-like structures with only local order.

5. $LaAlO_3$ (110) 3x1 Surface Reconstruction

5.1. Introduction

Lanthanum aluminate has recently become the subject of a rapidly expanding research area focused on the properties of oxide heterostructures, specifically $SrTiO_3/LaAlO_3$ interfaces [14, 90-93]. A 2D electron gas at the interface of these two insulating materials arises, along with interesting properties such as superconductivity [14], metal to insulator transitions [91], and magnetism [93], making it of interest for potential applications in microelectronics. However, putting together any $SrTiO_3$ and $LaAlO_3$ surfaces will not necessarily exhibit conductivity [92]. The unique properties have been attributed to an electronic reconstruction, which compensates for the valence discontinuity of the polar $LaAlO_3$ (001) surface with non-polar $SrTiO_3$ (001), but has now expanded to include contributions from structural deformations and oxygen defects [92]. The fact that the properties of the interface can vary so widely due to differences in structure and/or chemistry of only a few atomic layers on either side of the interface illustrates the need for understanding and atomic control at an interface to achieve a desired property. Metal oxide interface engineering poses a huge challenge to the scientific community, but on the other hand presents a great opportunity to discover heterostructures with novel properties for electronic device applications.

Despite the growth in $LaAlO_3/SrTiO_3$ interface research, there is little known about $LaAlO_3$ (LAO) surfaces. One reconstruction has been solved for the (001) surface, a $(\sqrt{5}x\sqrt{5})R26.6°$ [71], and a few others have been reported but not solved [94, 95]. The first reported characterization by Mortada *et al.* [94] of the LAO [110] surface observed a c(4x2)

reconstruction formed after annealing at 900°C in UHV. Another, Wang *et al.* [95], observed high-step terraces with fine-step details attributed to small-width facets after annealing in air at 1500°C for 10-20 hr.

This chapter reports the first observation of a 3x1 surface reconstruction on the LAO (110) surface and its atomic structure analysed from experimental electron diffraction data reinforced by density functional theory (DFT) calculations.

5.2. Experimental

5.2.1. Transmission Electron Microscopy and Direct Methods

Self-supported single crystal TEM samples were prepared from LAO [110] single crystal substrates commercially purchased from MTI Corporation (Richmond, CA), as detailed in Chapter 2. A well-ordered 3x1 surface was produced by annealing in air in a high-temperature tube furnace in the range of 1100-1200°C for 5 hours. TEM characterization of samples was done with a Hitachi H-8100 TEM operating at 200 kV. Bright field and dark field images, as well as off-zone diffraction patterns, were obtained. Diffraction patterns for the observed LAO (110) 3x1 surface reconstruction were recorded using photographic film with exposure times ranging 1-90 seconds and digitized using an Optronics P-1000 microdensitometer with a 25 μm pixel size. Spot intensities arising from the 3x1 surface were measured using a cross-correlation technique [80], and merged to create a single data set of 51 independent beams for EDM analysis.

5.2.2. Density Functional Theory

DFT was employed to determine the atomic positions in the out-of-plane direction perpendicular to the surface, as well as to check the agreement of in-plane atomic positions and calculate surface energies. In addition to conventional GGA, calculations were also performed with an on-site exact-exchange parameter of 0.335 for the La-*d* band levels, chosen so that the rhombohedral LAO lattice parameter was correct, to partially compensate for overbonding of the La-*d* levels with the O-*sp*, although the effect of this was minor; only results for the simpler PBEsol functional [41] and the meta-GGA form revTPSS [47], which is more accurate for the long-range contributions outside the surface, are shown here. Muffin tin radii (RMT) of 2.36, 1.65, 1.25, and 0.5 bohr were employed for La, Al, O, and H, respectively. A K_{max}min(RMT) cutoff of 5.85 and a *k*-mesh density corresponding to sampling 6-points along the ½(110) direction in reciprocal space (~0.3 nm^{-1} between points) were used.

Surfaces were modeled as 3D periodic slabs using in-plane positions from EDM and DFT-optimized bulk lattice parameters with 8 layers of LAO bulk separated by ~10 Å of vacuum in the *z*-direction and infinitely extending in the *x*- and *y*-directions, e.g., a 1.132 x 0.534 x 3.738 nm cell for the 3x1. The surface energy per 1x1 surface unit cell (E_{surf}) was calculated as

$$E_{surf} = (E_{slab} - E_{LAO}N_{LAO} - E_{AO}N_{AO})/(2N_{1x1}),$$

where E_{slab} is the total energy of the slab model, E_{LAO} and E_{AO} are the energies of bulk LAO and Al_2O_3, respectively, N_{LAO} and N_{AO} are the number of bulk LAO units and number of excess Al_2O_3 units, respectively, and N_{1x1} is the number of 1x1 surface cells. Error bars of 0.05 eV/1x1 were assigned, representing the average standard deviation between energies calculated using the

PBEsol and revTPSS DFT functionals, after removing a global shift of the surface energies of about 0.4 eV/1x1, where revTPSS results are higher (as expected.)

As a secondary check, bond valence sums (BVSs) were calculated using *KDist* in the *Kalvados* program suite [96], including bonding contributions from up to 3.5 Å away and a *b* value of 0.37 was used. Standard R_0 values of 1.620 Å and 2.172 Å were used for Al^{3+}-O^{2-} and La^{3+}-O^{2-}, respectively [97]. For H^{+}-O^{2-} bonds, a R_0 of 0.957 Å, corresponding to the O-H bond distance in gaseous H_2O, was used [73]. Lattice parameters used for DFT calculations were renormalized to the experimental values by changing the volume isotropically for BVS analysis; the adjustment was minor as PBEsol gave values very close to the correct bulk lattice parameters.

It is also worth noting that for a 12-coordinated La atom in LAO, the valence contribution per La-O bond is 3/12 = 1/4 valence per La-O bond compared to 1/6 for Sr in STO. Similarly, the 6-coordinated Al contributes 1/2 valence per Al-O bond while Ti contributes 2/3 valence per Ti-O bond. For an oxygen atom the ratio of valence contribution from Al/La is 2 while for Ti/Sr it is 4. Therefore, the oxygen valence in LAO is more dependent on La atom positions than it is on Sr positions in STO. This is important to keep in mind when comparing STO and LAO surface structures.

5.2.3. X-ray Photoelectron Spectroscopy

After TEM was used to confirm the presence of a LAO (110) 3x1 reconstruction, samples were loaded into SPEAR [98] where XPS data were collected. A series of XPS spectra for the La 4d and Al 2p peaks were collected at varying angles of the sample surface normal relative to the detector, to confirm the dominating surface species. Spectra for the O 1s peak were obtained

from samples before and after annealing at 650°C for 3 hr to look for evidence of hydroxyl groups at the surface. For annealing, samples were transferred to the analytical chamber of SPEAR and placed on an alumina heating stage, where the temperature was monitored by a thermocouple, as well as, a digital pyrometer, and an oxygen pressure of $1x10^{-6}$ torr was introduced.

5.3. Results

5.3.1. Transmission Electron Microscopy and Diffraction

An off-zone TEM diffraction pattern exhibiting well-ordered 3x1 surface spots (i.e., no streaking of spots) is shown in Figure 5.1. The reconstruction was present in areas on the order of several microns squared, and except for the 3x1, no other reconstructions were observed. A representative DF TEM image is shown in Figure 5.2. The change of thickness is shown by clearly defined contrast changes, indicating that the surface has wide areas of flat terrace steps roughly 0.15 microns wide.

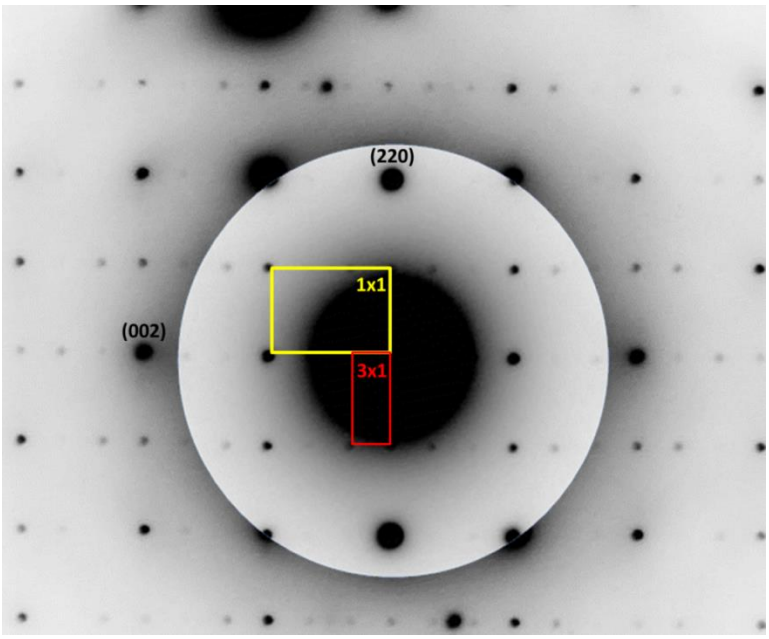

Figure 5.1. Off-zone TED pattern of $LaAlO_3$ (110) with a 3x1 surface reconstruction. Two DP's of with different exposure times were overlaid to show a wider range of surface spots. The 1x1 surface cell is outlined in yellow with the 3x1 cell in red.

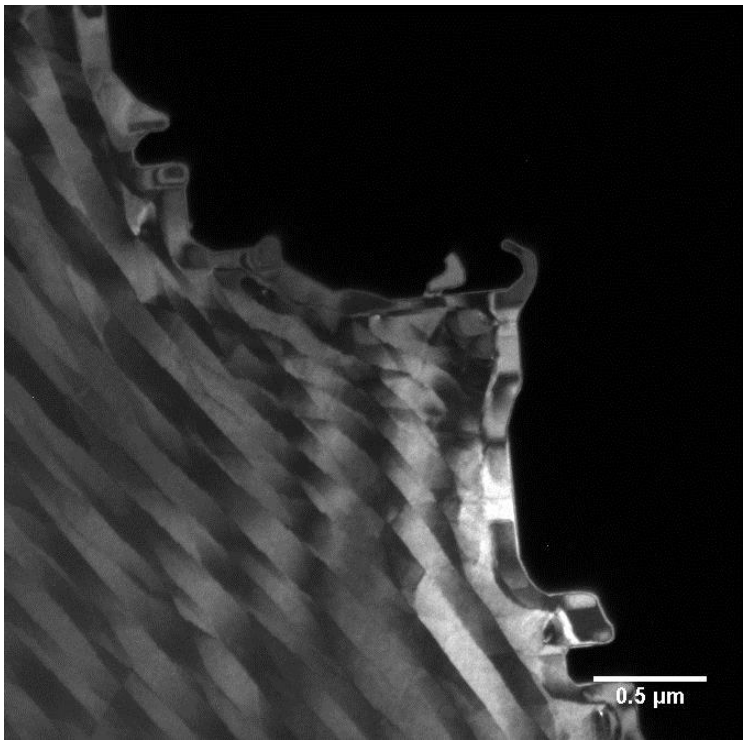

Figure 5.2. DF TEM image of the 3x1 reconstructed $LaAlO_3$ (110) surface.

5.3.2. X-ray Photoelectron Spectroscopy

The ratios of peak areas for the Al peak to the La peak at grazing angles of 0, 30, 45, 60, and 75° are plotted in Figure 5.3. The intensity of peaks was adjusted using relative sensitivity factors. As the grazing angle of the surface normal with the detector increases, the effective sampling depth decreases, making the technique more surface-sensitive. However, since the sampling depth is decreasing with increasing grazing angle, the signal decreases, making it difficult to get a signal past 75° normal to the surface. The ratio of Al-to-La increases with the grazing angle pointing to a surface with a higher concentration of Al than in the bulk. This detail was important in confirming our suspicion that the surface was Al-rich.

XPS spectra of the O 1s peak are shown in Figure 5.4. The 3x1 reconstructed sample used for this scan was first identified with TED, baked overnight at ~200°C in a load-lock chamber, and introduced to the SPEAR UHV Analytical chamber for XPS. To determine if water plays a significant role in the structure formation, i.e., is chemisorbed, XPS was done prior to and after annealing at 650°C in a connected UHV chamber so that it could be filled with a low pressure of oxygen to avoid reducing the surface ($1x10^{-6}$ torr).

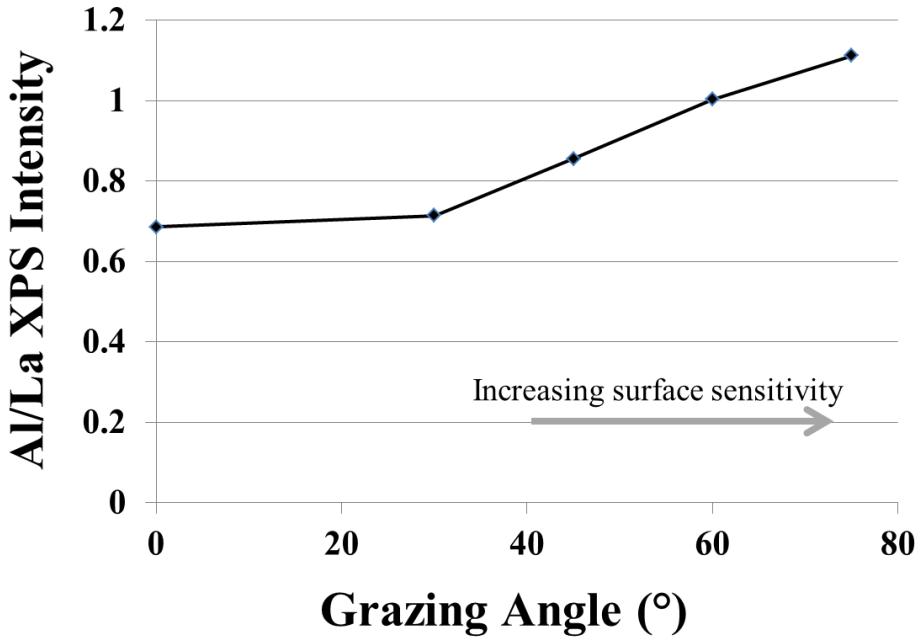

Figure 5.3. Ratio of Al/La XPS intensity peak areas adjusted by relative sensitivity factors versus the angle between the surface normal and the detector. As the angle becomes more grazing, the penetration depth of X-rays decreases while the effective surface sensitivity increases.

The bottom scan shows the main oxide peak in red with a maximum at 539.4 eV and a 1.9 eV higher binding energy shoulder at 541.2 eV. This is consistent with an O peak from aluminum oxide and a peak from surface hydroxyls separated by 1.6 eV, rather than a peak from O in molecularly absorbed water, which would result in a peak 3 eV higher in binding energy than the main oxide peak [99].

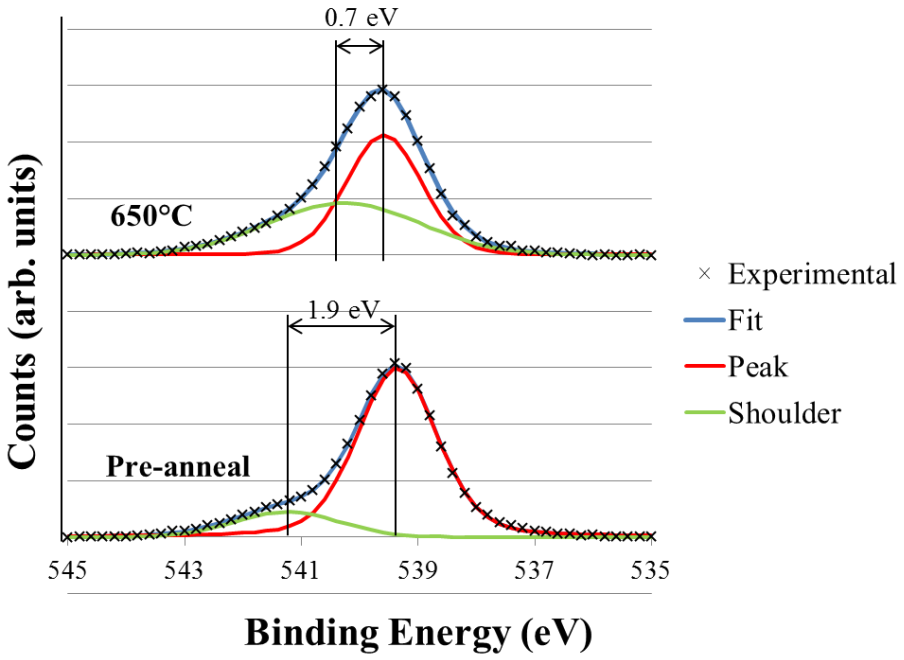

Figure 5.4. XPS spectrum of the oxygen 1s peak before (bottom) and after annealing (top) at 650°C for 3hr in $1x10^{-6}$ torr O_2 atmosphere.

Before annealing, XPS spectra were recorded at a 0° and 45° angles with respect to the surface normal shown in Figure 5.5. The ratio of the shoulder area to the peak area increased from 0.17 at a 0° grazing angle to 0.37 at a 45° grazing angle, indicating that the phenomenon causing the shoulder is located more towards the surface, as expected for surface hydroxyls. After annealing, the curve fittings for the main peak and the shoulder have maxima separated by 0.7 eV compared to a 1.9 eV separation prior to annealing. Because of the separation in the post-anneal spectra, it is more likely that hydroxyl groups from the surface have been removed, leaving an asymmetrical oxygen peak rather than a peak with hydroxyl shoulder. Unfortunately, TED was not able to be done on the sample after annealing to determine if the 3x1 surface reconstruction remained. Based just upon the XPS data, it is unclear the role that hydroxyl groups play in the 3x1 structure.

An estimate of the reconstructed surface depth can be found using the Beer-Lambert Equation:

$$I_1 = I_0 \exp[-d/\lambda \cos\theta_1]$$

where I is the intensity of electrons, I_0 is the intensity of electrons from an infinitely thick sample, and λ is the attenuation length related to the inelastic mean free path of an electron in the sample. Comparing the intensity detected at the surface normal and at a grazing angles (θ_2) results in the following:

$$d = \ln(I_1/I_2)[\lambda/(1/\cos\theta_2)-1]$$

To obtain an estimate of the depth of the Al rich surface reconstruction, a λ of 4.2 Å for an electron ejected from an Al atom with a binding energy of 81.5 eV [100] is used, corresponding with the Al 2p peak energy. The normalized intensities for the Al 2p peak area at θ_1=0° and θ_2=75° are I_1=0.72 and I_2=3.79, respectively, resulting in a thickness layer of roughly 2.4 Å or about 2 monolayers.

5.3.3 Electron Direct Methods

An EDM analysis resulted in several scattering potential maps that were similar to, or contained fragments, of the solution that is shown in Figure 5.6. Bright spots were determined by comparing refinement values for Al in those positions versus La. Al and La gave similar R_1 values, but the χ^2 for Al was significantly lower. This corresponds with the results from XPS that show the surface is Al-rich. Also, the map looks very similar to the resultant EDM for the $SrTiO_3$ (110) 3x1 solved by J. Enterkin [50], referred to as STO 3x1 throughout this chapter. This point is illustrated by the high agreement of cation positions between the map and surface layer from

the STO 3x1 that is overlaid on the left. It refines very well with the experimental data, having an R_1=0.07 and χ^2=1.8.

Unfortunately, the STO 3x1 reconstruction cannot be directly adapted for LAO. The 2D 3x1 surface layer with *x*- and *y*- positions found by EDM must fit onto a bulk layer and balance the surface valence. Along the [110] direction, the bulk crystal structure of LAO consists of two alternating layers, O_2^{4-} and $LaAlO^{4+}$, just as STO consists of O_2^{4-} and $SrTiO^{4+}$ layers, but the difference in formal valance states of Al^{3+} and Ti^{4+} requires additional consideration to be valence-neutral. The surface layer for STO contains 5 Ti and 7 O summing to a valence state of 5*4 - 7*2= 6+, which cancels with the 6- from the bulk oxygen layer beneath it. LAO on the other hand would have a valence of 5*3 – 7*2=1+ that could not be balanced.

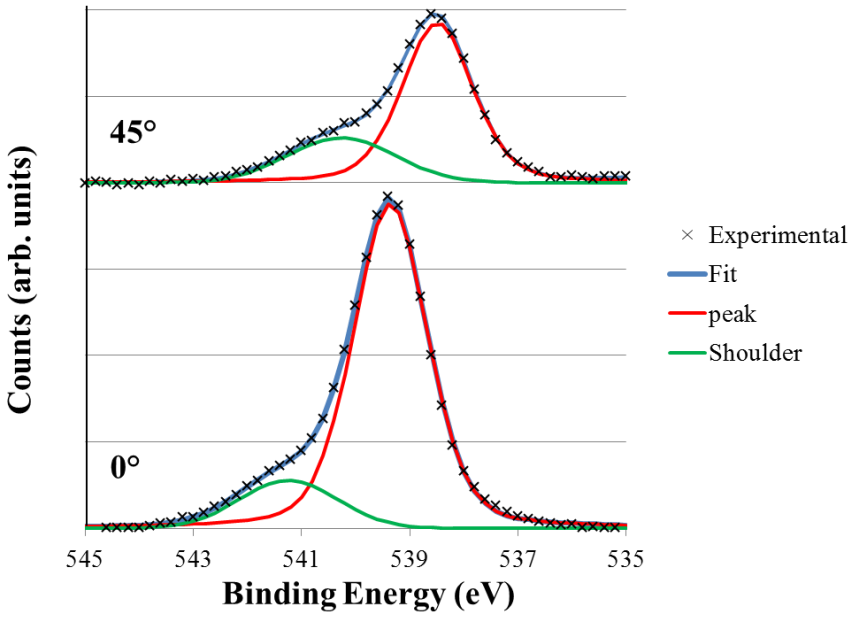

Figure 5.5. XPS spectrum of the oxygen 1s peak at grazing angles of 0° (bottom) and 45° (top) to the surface normal.

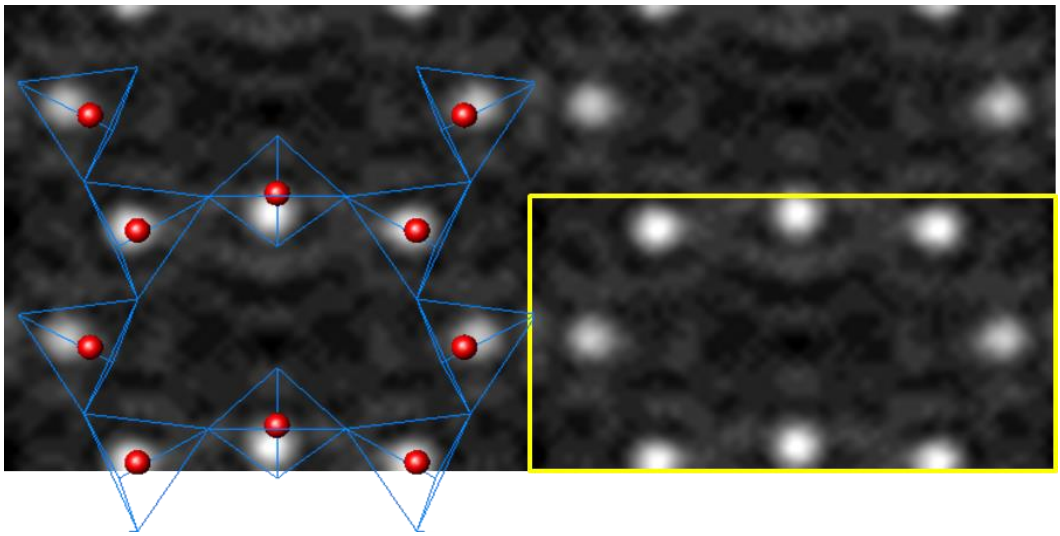

Figure 5.6. EDM scattering potential map with surface unit cell outlined in in yellow for $LaAlO_3$ (110) 3x1 surface reconstruction. To demonstrate the similarity to the $SrTiO_3$ (110) 3x1 reconstruction a cartoon of the structure is overlaid the map showing six TiO_x

Several ways were investigated to reach valence neutrality, such as additional units on the STO-type 3x1 and a similar network with 4 Al per surface unit cell arranged in 6-member polyhedra rings. Another way to reach valence neutrality is with hydroxyl groups and several structures incorporating OH^- were investigated as well. These structures are discussed further in the next section. Two of the structures, M and P (refer to Table 1), which are variations on the STO 3x1-type structure and have the lowest surface energy, also refine reasonably well with R_1 values of 0.10 and 0.15, respectively, although not as well as fitting with STO 3x1 positions. Their χ^2 values, 3.5 and 3.9, respectively, are much higher, most likely due to the greater number of atoms in the surface cell. The wet 3x1 surface structures H-1 and H-5 discussed in the next section have R_1 values of 0.20 and 0.20, respectively, and χ^2 values of 2.2 and 1.9, respectively. Overall the wet structures have slightly higher R_1 values, but lower χ^2 values.

5.3.4. Density Functional Theory

Part of the difficulty in using surface energies to determine a surface structure for this system is the lack of any previously solved structures with which to compare. As a frame of reference, the stoichiometric α-Al_2O_3 (0001) and $(1\bar{1}02)$ faces were calculated having surface energies of 2.9 and 2.3 eV, respectively, for the same surface area as a LAO (110) 1x1 surface cell.

A wide range of LAO (110) surfaces structures were optimized and their surface energies calculated with DFT. This also helps to give a better picture overall of which structures might be feasible or not. Initially, only "dry" structures were calculated. The resulting surface energies for all of the structures are shown in Figure 5.7. The details for a selected set of structures comprising those with the lowest calculated surface energies (B, M, P on the convex hull line) are shown in Table 5.1 with their surface layer and subsurface layer composition, amount of excess $AlO_{1.5}$ units, excess H_2O, and surface energy. The remaining higher energy structures will not be discussed here. For their details, see Appendix A.2. "Wet" structures were created based on the dry structures with the lowest surface energies and the STO 3x1 reconstruction.

Structure B has a 2x1 surface unit cell and will be referred to as the "2x1." It is a simple LAO bulk-terminated surface with two oxygen vacancies to balance the net valance. Structures M and P are based on the STO 3x1 network structure of alternating 6- and 8-member rings. Structure M, to be referred to as "3x1 Al-10", shown in Figure 5.8, mimics the STO 3x1 surface layer as well as its subsurface layer of $3(O_2^{4-})$, but with an additional 5 AlO_5 polyhedra in the center of the larger ring at the outermost surface. Structure P, to be referred to as the "3x1 Al-12", also shown in Figure 5.8, has a higher excess of Al at the surface due to a bulk-like subsurface layer of 6 AlO_x polyhedra and an additional AlO_2 incorporated in the center of the

smaller surface ring. The additional Al is necessary to balance the surface valence, as well as raise the Al excess to a level consistent with the 2 monolayers found from XPS data.

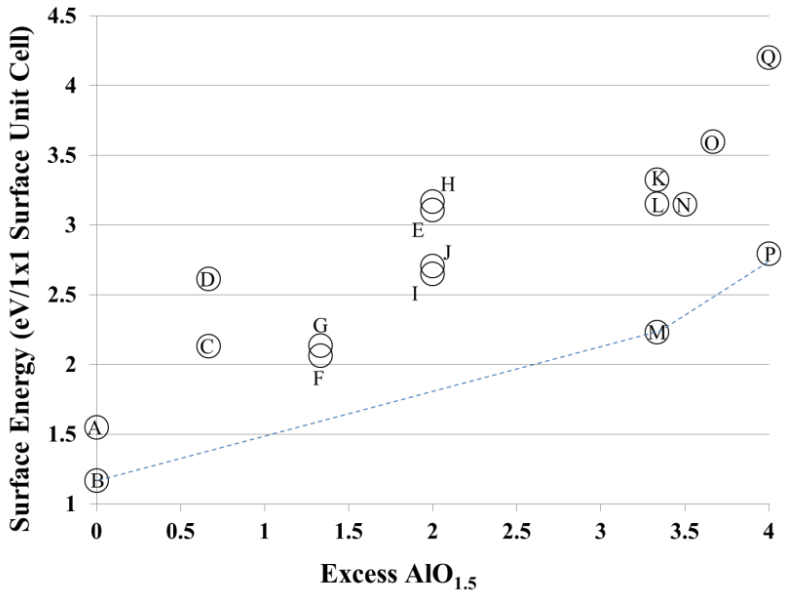

Figure 5.7. Plot of surface energies per 1x1 bulk surface unit cell versus excess $AlO_{1.5}$ units at the surface. Convex hull is indicated by the dotted line connecting the lowest energy structures. Structures B, M, and P are described in Table 5.1, and the remaining are described in Appendix A.2.

Additionally, several hydroxylated "wet" LAO surfaces, based on the STO 3x1 surface of alternating rings of 6 and 8 AlO_x polyhedra, but with added OH^- to achieve valence neutrality, were considered. The wet 3x1 structures, referred to as "H-1" and "H-5", both have a bulk oxygen subsurface layer, but with different surface water content; H-1, shown in Figure 5.9, has one additional OH^- per 3x1 and H-5, shown in Figure 5.10, has 5 additional OH^- per 3x1.

Two simple 1x1 LAO structures, one with excess H_2O (1x1 H) and one with excess Al and H_2O (1x1 AlH), were included to aid in the comparison of the wet structures.

Table 5.1 Table of $LaAlO_3$ (110) structures with DFT calculated surface energies.

Label	Surface Cell	Description	Surface layer	Subsurface layer	Excess ($AlO_{1.5}$/1x1)	Excess (H_2O/1x1)	Surface Energy (±0.05 eV/1x1)
2x1	2x1	Bulk terminated layer with 2 oxygen vacancies	$2O^{4-}$	$2(O_2^{4-})$	0	-	1.95
3x1 Al-10	3x1	STO 3x1-type surface with Al_5O_5	$Al_{10}O_{12}^{6+}$	$3(O_2^{4-})$	3.333	-	3.91
3x1 Al-12	3x1	STO 3x1-type surface with AlO_2 unit	Al_6O_8	$3(Al_2O_2^{2+})$	4	-	4.60
3x1 H-1	3x1	STO 3x1-type surface with OH^- unit on top bulk oxygen layer	$Al_5O_4(OH)^{6+}$	$3(O_2^{4-})$	1.667	0.167	3.26
3x1 H-5	3x1	Similar to Wet-B saturated with OH^- units	$Al_5O_2(OH)_5^{6+}$	$3(O_2^{4-})$	1.667	0.833	1.55
1x1H	1x1	Bulk terminated layer with two OH^- units	$(OH)_2^{2-}$	$LaAlO^{4+}$	0	2	0.44
1x1AlH	1x1	Al-rich 1x1 saturated with OH^- units	$(OH)_2^{2-}$	$Al_2(OH)_2^{4+}$	2	4	1.73

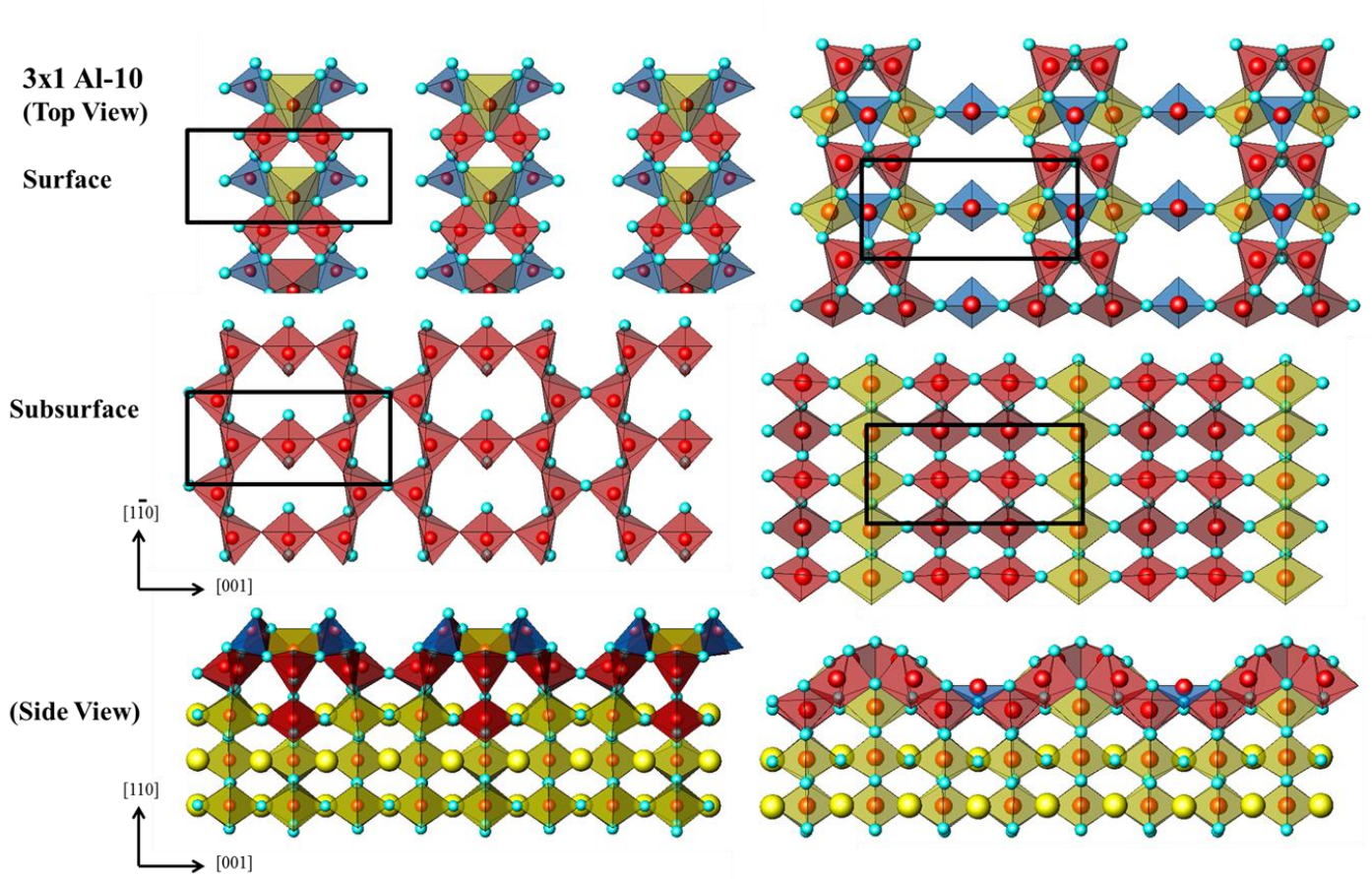

Figure 5.8. (Left) Plan view of the 3x1 Al-10 surface consisting of the outermost surface layer (top) and the next layer below (middle) and a view parallel to the surface (bottom). The subsurface layer mimics the structure of the STO 3x1 structure. Blue, red, and yellow polyhedra represent TiO_4, TiO_5, and TiO_6, respectively. (Right) Plan view of the 3x1 Al-12 surface consisting of the outermost surface layer (top) and the next layer below (middle) and a view parallel to the surface (bottom). The surface layers mimics the STO 3x1 structure with an additional TiO_4 is the center of the smaller ring. Blue, red, and yellow polyhedra represent TiO_4, TiO_5, and TiO_6, respectively.

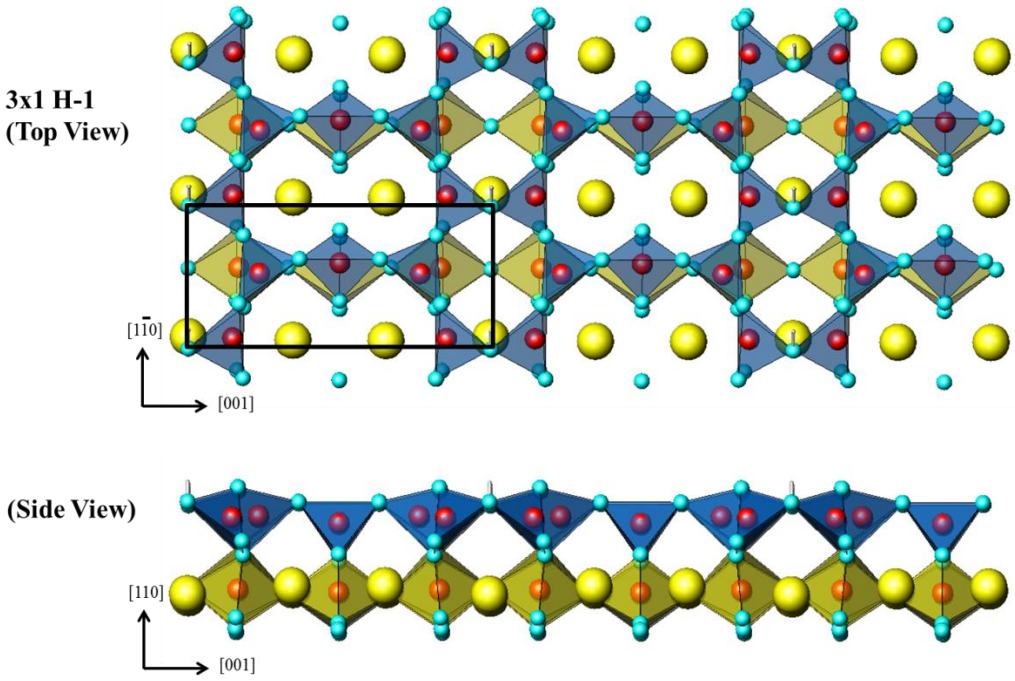

Figure 5.9. Top view perpendicular to the 3x1 H-1 structure surface and side view parallel to the surface. Blue and yellow polyhedra represent TiO_4 and TiO_6, respectively. La, Al, O, and H atoms are in yellow, red, light blue and grey, respectively.

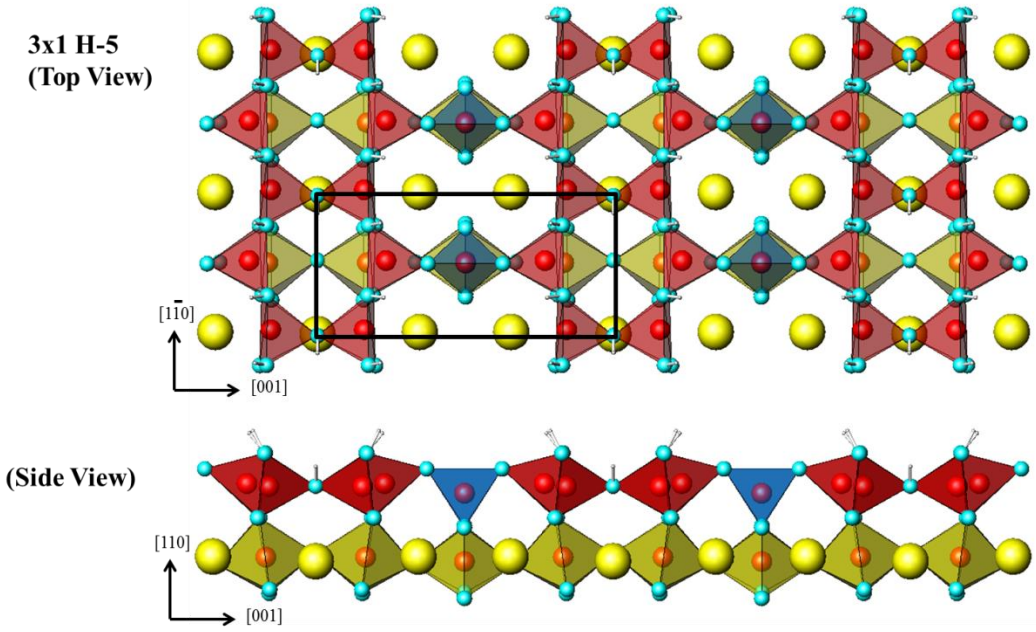

Figure 5.10. Top view perpendicular to the 3x1 H-5 structure surface and side view parallel to the surface. Blue, red and yellow polyhedra represent TiO_4, TiO_5, and TiO_6, respectively. La, Al, O, and H atoms are in yellow, red, light blue and grey, respectively.

The three-dimensional convex hull is plotted in Figure 5.11, generated using MATLAB software [100] (MATLAB code provided in Appendix A.4). The calculated surface energies are plotted on the *z*-axis with excess $AlO_{1.5}$ per 1x1 surface cell along the *x*-axis and excess H_2O per surface 1x1 along the *y*-axis. The overall surface energy range is reasonable given the energies of the alumina references. If we consider only the dry structures in the excess Al vs. surface energy plane at zero excess H_2O, a convex hull line connects the lowest energy structures for each stoichiometry. The 2x1 bulk terminated layer with two O vacancies, the 3x1 Al-10, and 3x1 Al-12 define the convex hull line. Both Al-10 and Al-12 are structures based on the STO 3x1, with alternating 6- and 8-member AlO_x polyhedra.

Looking to the center of the plot, the 3x1 H-5 structure forms at the convergence of all the convex hull planes and would be the most stable structure in that stoichiometric range. This is not surprising, since the H-5 structure is essentially analogous to the STO 3x1 with added hydrogen. H-5 also lies in the excess Al range, consistent with XPS results. At higher amounts of excess water (i.e., higher water chemical potentials), the 1x1 H and AlH structures define the convex hull plane. Moving from a 3x1 H-5 surface to higher chemical potentials may create a surface mixture of H-5, 1x1 H, and 1x1 AlH, although the 1x1 surfaces would not be detectable by TED. Moving from 3x1 H-5 to less H_2O, the surface may dehydrate to the H-1 structure, which is essentially the same polyhedric structure, but with one OH^-. H-1 is also close enough to the convex hull, meaning that an H-5 structure obtained while annealing at high temperatures in a wet environment and then cooled to room temperature would evolve to an H-1 by dehydrating, but not completely, and retaining its atomic arrangement. Although the H-1 is above the convex hull, converting to one of the dry structures would involve atomic rearrangement that may be kinetically limited.

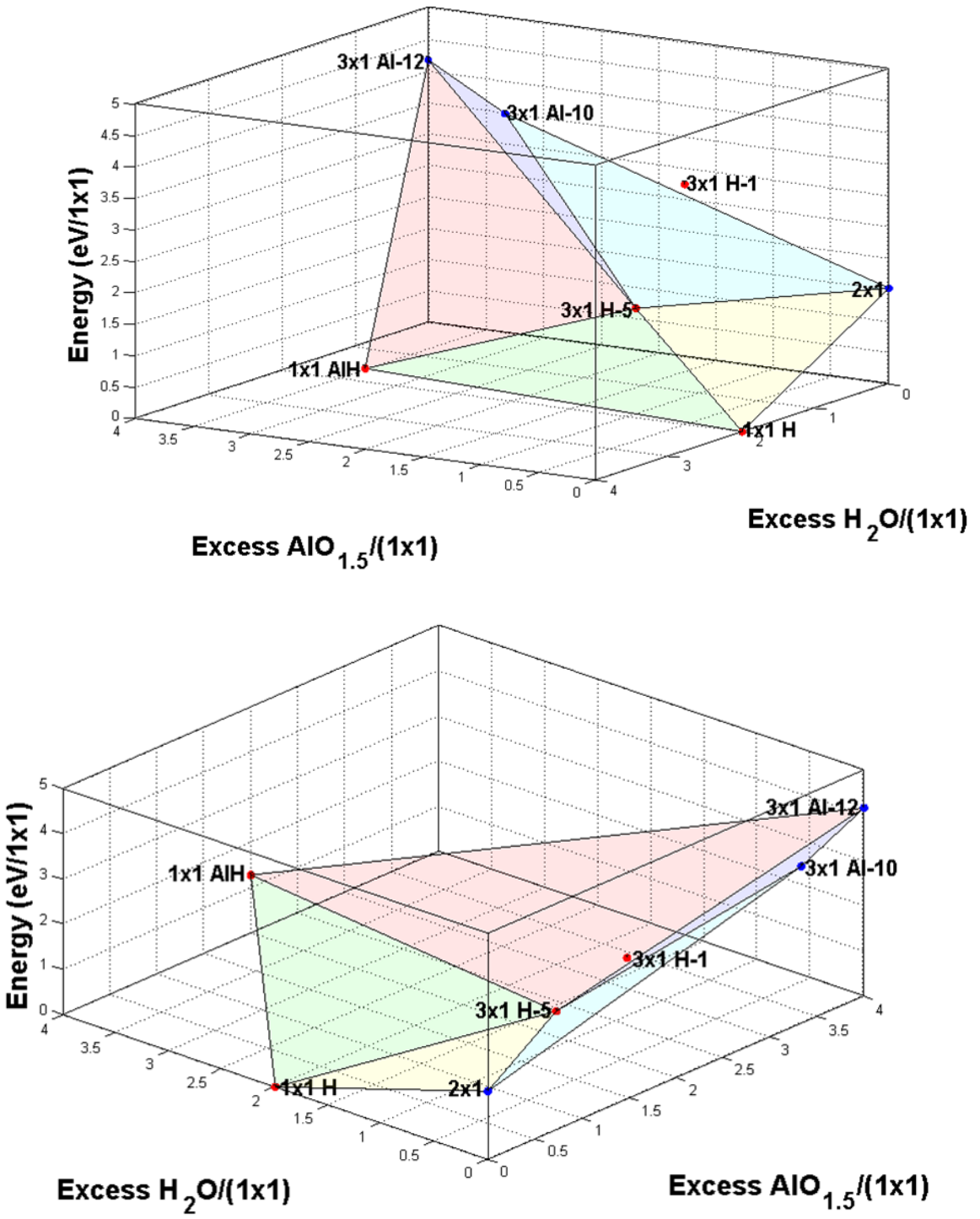

Figure 5.10. Two views (top and bottom) of a 3D plot showing the calculated surface energy for $LaAlO_3$ (110) surface structures relative to the amount of excess $AlO_{1.5}$ on the x-axis and H_2O on the y-axis. Dry structure markers are blue and hydroxylated structure markers are red. Colored planes form the convex hull connecting the lowest energy structures. Surface energies are referenced to the 1x1 H energy.

5.3.5 Bond Valence Sums

Since conventional BVS methods in the bulk are only accurate for octahedral AlO_6 configurations, the BVS for other oxides containing Al were calculated in a range of bonding configurations such as strontium aluminate ($SrAl_4O_7$) [101]. Its structure contains Al atoms that are bonded to 5 oxygen, with an average BVS of 2.85 as well as Al bonded to 4 oxygen with a lower average BVS of 2.65. Another oxide, lanthanum hexaluminate [102], contains Al that can be 4, 5, and 6-fold coordinated, with BVS values ranging from 2.43 for tetrahedral to 2.97 for octahedral, which is closer to the BVS for Al in bulk LAO of 2.85.

The BVS for the three dry structures defining the convex hull at zero H_2O, namely the 2x1, 3x1 Al-10, and 3x1 Al-12, are detailed in Table 5.2, and for the 3x1 H-1 and H-5, Table 5.3. It is important that the local bonding via BVS is comparable to what is found in the bulk oxide. The average BVS at the bottom of the tables are referenced to $LaAlO_3$ bulk values of 2.85, -1.96, and 3.04 for Al, O, and La, respectively, to better illustrate the deviation. The surface BVS numbers do not differ substantially from those of the reference oxides, reinforcing the structures' feasibility. The overall BVS for the H-5 structure are closer to bulk values than H-1 because of the additional OH^- that help improve the Al and O coordination.

Table 5.2 Bond Valence Sums (BVS), coordination number (CN) and multiplicity within the cell (Mult.) for atoms in the surface and subsurface layer for the LAO 2x1, 3x1 Al-10, and 3x1 Al-12 structures. Average BVS are referenced with respect to bulk BVS of Al (2.85) and O (-1.96).

	2x1				3x1 Al-10				3x1 Al-12			
	Atom	**BVS**	**CN**	**Mult.**	**Atom**	**BVS**	**CN**	**Mult.**	**Atom**	**BVS**	**CN**	**Mult.**
Surface layer	Al1	2.56	5	2	Al34	2.63	6	2	Al13	2.97	4	1
	La5	2.41	9	2	Al45	2.46	6	1	Al5	2.71	6	2
	O2	-1.74	5	2	Al37	2.77	6	2	Al6	2.72	6	2
	O1	-1.26	3	2	O3	-1.99	4	1	Al15	2.40	5	1
					O6	-1.92	3	2	O31	-1.62	3	2
					O2	-1.59	2	2	O32	-1.86	3	2
									O34	-1.59	3	1
									O29	-2.15	4	2
									O30	-2.16	5	1
									O33	-2.10	5	1
Subsurface layer	Al5	2.91	6	2	Al33	2.81	6	2	Al4	2.55	5	2
	La3	3.14	12	2	Al38	2.81	6	1	Al3	2.68	5	2
	O5	-1.99	6	2	Al39	2.61	6	2	Al11	3.08	6	1
	O3	-2.00	6	2	O7	-2.04	5	1	Al7	2.59	6	1
	O4	-2.00	6	2	O5	-1.81	5	2	O1	-1.68	5	2
					O4	-1.75	3	2	O2	-1.31	4	2
					O1	-1.90	3	2	O15	-1.71	4	1
									O16	-1.57	3	1
Average Surface Al		-0.29				-0.02				-0.14		
Average Surface O		0.46				-0.04				0.06		
Average Subsurface Al		0.06				-0.12				-0.14		
Average Subsurface O		-0.04				0.13				0.42		

Table 5.3 Bond Valence Sums (BVS), Coordination number (CN) and multiplicity within the cell (Mult.) for atoms in the surface and subsurface layer for wet LAO 3x1 H-1 and H-5 structures. BVS are references with respect to bulk BVS of Al (2.85) and O (-1.96).

	3x1 H-1				3x1 H-5			
	Atom	**BVS**	**CN**	**Mult.**	**Atom**	**BVS**	**CN**	**Mult.**
Surface	Al3	2.55	4	2	Al2	2.82	5	2
	Al4	2.48	4	2	Al3	2.68	5	2
	Al5	2.71	4	1	Al4	2.72	4	1
	O2	-1.51	2	2	O2	-1.57	2	2
	O26	-1.64	2	2	O26	-1.93	3	2
	O27	-1.27	3	1	O28	-2.00	3	2
	O3	-1.81	4	2	O27	-2.27	4	1
	O4	-2.20	4	2	O3	-1.90	4	1
	O15	-1.89	5	2	O4	-1.98	4	1
	O16	-1.65	5	2	O15	-1.70	5	2
	H1	0.87	1	1	O16	-1.79	5	2
					H1	0.90	1	1
					H2	0.96	1	2
					H3	0.90	1	2
Subsurface	La3	3.27	12	1	La3	3.03	11	2
	La8	3.29	12	2	La6	3.14	12	1
	Al2	2.61	6	2	Al6	2.93	6	2
	Al7	2.91	6	1	Al1	2.62	6	2
	O1	-1.66	5	1	O1	-1.60	5	2
	O5	-1.91	5	2	O5	-1.96	5	2
average surface Al		-0.30				-0.11		
average surface O		0.22				0.10		
average subsurface Al		-0.14				-0.07		
average subsurface O		0.13				0.18		

5.4. Discussion

One of the challenges that is faced when attempting to solve a surface structure such as the LAO 3x1 is knowing when it has truly been solved. While correlation between the refined positions from diffraction data and the DFT-stable positions suggests that a solution is correct, this alone is not a complete proof. Other conditions need to be met:

1. There must be a correlation between the refined positions from diffraction data and the DFT stable positions.

2. There should not be major chemical distortions of the underlying bulk material, such as an unrealistically small bond length of 0.5 Å between an O and La atom.

3. It must fit other constraints from the preparation conditions; here it needs to be a valence-neutral insulator with a respectable band gap.

4. The energy has to be reasonable with the surface part of the convex-hull construction. However, this is only a relative measure referenced to some bulk chemical potential, here to that of Al_2O_3.

5. The local bonding must be reasonable, this being an absolute (not a relative) condition.

Addressing condition (1), the 3x1 Al-10 and Al-12 have decent refinement values, although the STO 3x1-type surface and wet 3x1 H-1 and H-5 structures refine better. It is hard to say if this disqualifies Al-10 and Al-12 from being a solution at higher amounts of Al and zero chemical potential of water. All structures satisfy conditions (2) and (3) as well.

In the absence of a solved LAO (110) surface structure, with which to compare surface energies, a large amount of structures were computed to reveal the energy region the surface most likely occupies. Condition (4) is met since the H-5 structure defines the convex-hull.

The BVS of structures are acceptable given the wide range of bond valence states in which Al in oxide compounds can exist, thus satisfying condition (5). Although a definitive structure cannot be pinpointed, there is strong evidence that the observed LAO (110) 3x1

reconstruction is the H-5 structure, remarkably similar to the STO (110) 3x1 reconstruction, but with water.

The kinetic pathway a LAO TEM sample surface would take starts with a disordered, amorphous surface caused by ion polishing during preparation. It is then annealed at high temperatures (1100-1200°C) in the presence of water. When annealed, the near-surface layers begin to reorder to a bulk structure, and the surface forms some combination of the 1x1 H, 1x1 AlH, and 3x1 H-5 surfaces. As the sample is cooled, according to the convex hull, the surface would be dominated by the 3x1 H-5. Further cooling would cause the H-5 to dehydrate, although not completely as evidenced by the hydroxyl shoulder observed on the oxygen peak with XPS. The H-5 structure persists at room temperature, with perhaps varying amounts of hydroxyls such as the H-1, which although slightly higher in energy than the convex hull, would be preferable to atomically rearranging to a 3x1 Al-10 or Al-12.

5.5. Conclusions

Al atoms at the surface have less bonds than octahedrally bonded Al in the bulk which allows for the creation of a stable 2D network of AlO_x at the surface. The behavior of Al at the surface may be more closely related to network-formers in glasses just as has been suggested in Chapter 3 for the STO RT13. Al is known to act as a network former and occupy tetrahedral sites in many materials, most commonly in aluminosilicate glasses [103]. Studies on aluminosilicate glasses and gels have shown that Al^{3+} can replace Si^{4+} as the tetrahedral network former, and may form amorphous networks with irregular cross-linking for charge compensation rather than forming 5-fold coordinated Al [103]. In this way, the LAO surface can be imagined as a sheet of networked AlO_x polyhedra that order into a ring motif at temperatures above 1100°C, producing the 3x1

reconstruction aided by water. Thinking of the surface as a pseudo-glass network of rings is something that could be extended to other perovskites and is demonstrated in the recently determined $SrTiO_3$ surface reconstructions: (110) 3x1 [50] and (001) ($\sqrt{13}$x$\sqrt{13}$)R33.7° [72].

6. $LaAlO_3$ (001) 5x2

6.1. Introduction

Similar to $SrTiO_3$, much work has been done examining the surface of $LaAlO_3$ because of its use as substrates for thin-film growth. Also, like $SrTiO_3$, much of the work is contradictory. Only three reconstructions have been observed on the surface, including the 5x5 [104], the (√5x√5)R26.6º [71], and most recently, presented here, a 5x2 with two domains. Only the (√5x√5)R26.6º has been solved. All other studies have been dedicated to determining whether the surface is terminated with aluminum and oxygen (Al-O) or lanthanum and oxygen (La-O).

6.2. Background

Wang *et al.* annealed mechanically polished $LaAlO_3$ (001) samples in air for 20 hours at 1500ºC and examined the surface step morphology with reflection electron microscopy (REM). The surface steps were found mostly on the [100] and [010] planes, while the composition of the surface was determined to be either all La-O or all Al-O, not a mixture of both [105]. Yao *et al.* found similar results using a variety of techniques including time-of-flight scattering and recoiling spectrometry (TOF-RS), atomic force microscopy (AFM), low energy electron diffraction (LEED), Auger electron spectroscopy (AES), and X-ray photoelectron spectroscopy (XPS). They found that the surface is terminated by an Al-O layer at room temperature to about 150ºC and a La-O layer at temperatures above about 250ºC. Therefore, the surface is terminated by one or the other except at temperatures between 150 and 250ºC where mixed terminations were found. Additionally, the changing of the surface termination was found to be completely

reversible, meaning the surface returned to Al-O upon cooling. They proposed that oxygen deficiencies are created at higher temperatures causing the aluminum to move into the oxygen-rich subsurface while lanthanum outwardly segregates to the surface [106]. Van der Heide *et al.* used angle-resolved XPS to examine the surface, finding a high binding energy component on the Al 2p spectrum that is localized at the surface and is only observed at temperatures below about 200ºC. They also saw a decrease in the surface oxygen content at elevated temperatures. Both findings were reversible and stated to be in agreement with the findings of Yao *et al.* [107].

Alternatively, there is work by Kawanowa *et al.* that directly refutes work by Yao *et al.* They used low energy neutron scattering spectroscopy (LENS) to examine the $LaAlO_3$ surface. Samples were first annealed at 1000K for 8 hours in UHV. Measurements on the samples were then taken at room temperature and 1000K. They found La-O only present at 1000K and *both* La-O and Al-O present at room temperature. A second set of samples with "deoxidized surfaces" were annealed at 1300K for 15 hours in UHV accompanied by a color change from yellowish-clear to light green indicating the lack of oxygen present. Again, measurements taken at 1000K and room temperature found the surface to be mainly terminated by La-O at both temperatures [108]. Also stating disagreement with Yao *et al*. is Francis *et al*. whose samples were first annealed in flowing oxygen at 1473K. An X-ray crystal truncation analysis was done on data collected from samples at room temperature and 670K. They found that an Al-O terminated surface was a better fit to the data at both temperatures. They used this as a starting point for proposing a model to better fit the data. At room temperature, they found fairly minor structural rearrangements of a bulk AlO_2 terminated surface. At the elevated temperature, aluminum relaxed further into the surface accompanied by lateral movements of the surface oxygen. This process was also found to be reversible. They offer the following explanation: at higher

temperatures, the lanthanum, although not on the surface, are more exposed, accounting for the results found by Yao *et al.* [109].

6.2.1. Previous Reconstructions

In addition to concluding the $LaAlO_3$ (001) surface was only terminated by La-O or Al-O, not both, Wang *et al*. observed a (5x5) reconstruction with reflective high energy electron diffraction (RHEED) [104]. Their samples were annealed in air at 1500ºC for 20 hours. They do not, however, address which cation was present at the surface for this reconstruction. Jacobs *et al*. claims that the 5x5 observed by Wang *et al*. is an Al-O populated surface based on molecular dynamics simulations [110]. Simulations were done on surface slabs removing the boundary conditions in the *z*-direction so that atoms were free to move to a low energy configuration. Upon careful inspection of the final configuration of an AlO_2 terminated surface allowed to reconfigure itself, a reconstructed cell is observed that fits with the 5x5. It is also important to note that in a previous paper, Jacobs *et al.* compared molecular simulations of an AlO_2 and LaO terminated surface, finding the LaO terminated surface had a much lower surface energy [111]. Therefore, they order the surface energies of $LaAlO_3$ (001) from lowest to highest as the Al-rich (5x5) reconstruction, LaO terminated surface, and AlO_2 terminated surface. However, it should be remembered that comparing the energies of surfaces with different chemical compositions directly is not appropriate thermodynamically, and one has to use the proper convex-hull approach.

The $LaAlO_3$ (001) ($\sqrt{5}$x$\sqrt{5}$)R26.6º reconstruction was observed in the Marks group by Lanier *et al.* [71]. Although there have been studies of the $LaAlO_3$ (001) surface, this is the first paper to address the issue of charge compensation and how to reconcile the electrostatic dipole at

the surface. Samples were annealed at temperatures between 1100 and 1500ºC for 3 hours in air and a mixture of 20% O_2 and 80% N_2. The reconstruction was observed with off-zone transmission electron diffraction (TED) and solved with DM and DFT. The structure was found to be an over-layer of LaO on a bulk termination of AlO_2 with one La vacancy per surface unit cell. The La vacancy is formed to reduce positive charge at the surface of an ideal LaO bulk termination. Since, La^{3+} is less electronegative, it is favored for vacancy formation. The surface polarity is finally quenched by the presence of an electron hole created by some of the charge on the oxygen ions in the bulk transferring into the covalent bonds near the surface. This was determined after considering and disproving charge compensation by the methods of oxygen vacancies or the presence of H^+ on surface from water splitting.

6.3. Experimental

Self-supported single crystal TEM samples were prepared from LAO [001] single crystal substrates commercially purchased from MTI Corporation (Richmond, CA). To obtain a 5x2 surface, annealing was done in a high-temperature tube furnace over a wide range of times and temperatures.

TEM characterization of samples was done with a Hitachi H-8100 TEM operating at 200 kV in the Northwestern EPIC facility. Bright field and dark field images as well as off-zone diffraction patterns were obtained. Diffraction patterns for the observed LAO (001) 5x2 surface reconstruction were recorded using photographic film with exposure times ranging 1-90 seconds and digitized using an Optronics P-1000 microdensitometer with a 25 μm pixel size. Spot intensities arising from the 5x2 surface were measured using a cross-correlation technique [80] and merged to create a single data set of 51 independent beams for EDM analsyis.

XPS spectra was collected within the SPEAR [96] system for the Al 2p and La 4d peak regions on a sample exhibiting the 5x2 over a range of angles (0-75°) to the detector to determine the dominating surface species, as well as look for evidence of hydroxyl groups at the surface. For more details on the experimental techniques, refer to Chapter 2.

6.4. Results and Discussion

6.4.1. Transmission Electron Microscopy and Diffraction

A 5x2 surface was produced by annealing in air in a high-temperature tube furnace in the range of 1200-1400°C for 3-6 hours. Obtaining a surface with the 5x2 reconstruction was extremely difficult because the annealing conditions that produced a 5x2 coincide with those that produce a RT5, 1100-1500°C for 3hr in air [71]. In Figure 6.1, various time and temperature annealing conditions (in air) that were used and the resultant reconstruction that was observed is plotted. In some cases, streaking in the diffraction pattern rather than a well-ordered reconstruction was observed indicated as “Streaked” in the graph. High temperature anneals at 1400°C resulted in silica contamination at the surface from the quartz tube the sample was annealed in. Longer annealing times of 10 hr resulted in sample coarsening and less thin area for TEM analysis. The 5x2 was most consistently obtained (although not exclusively) using a stepped annealing profile, 5 hr at 700°C followed by 3 hr at 1250°C in air.

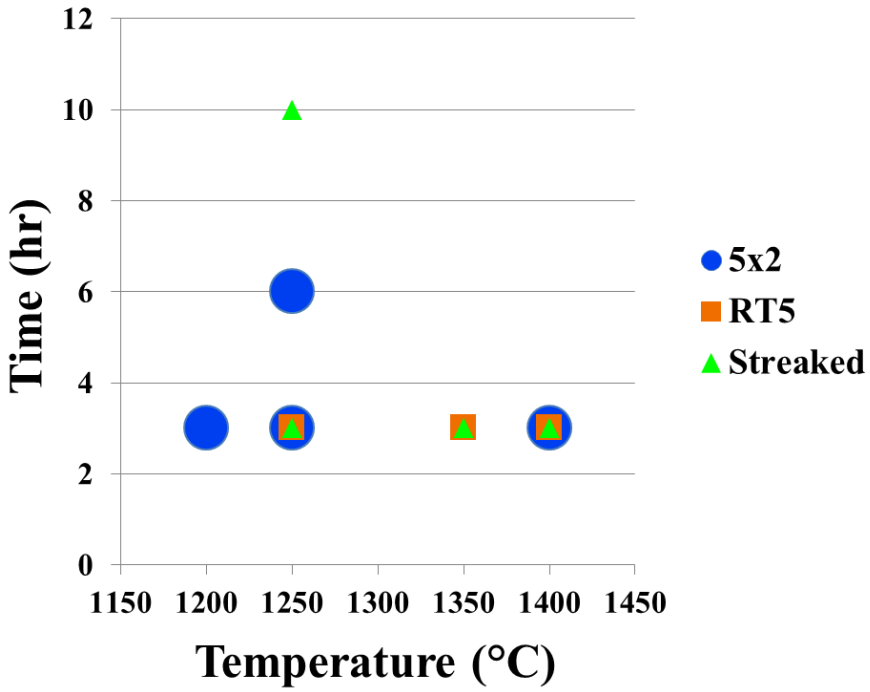

Figure 6.1. Plot of experimental annealing temperature and time conditions and the observed LAO (001) surface that was produced: 5x2, RT5, or a "streaked," semi-formed surface.

A BF TEM image of a LAO (001) sample with a 5x2 reconstructed surface, shown in Figure 6.2, exhibits flat steps with step edges running along two directions perpendicular to each other. A representative off-zone TED pattern for a 5x2 reconstructed surface is shown in Figure 6.3 with the two domains and surface unit cell indicated. Another DP of a sample with a 5x2 surface is shown in Figure 6.4, however, there is also the presence of surface spots not belonging to the 5x2 pattern. The second reconstruction giving rise to the spots is most likely the RT5, whose annealing conditions overlap with the 5x2. There is also the possibility that the extra spots are caused by a 5x5 reconstruction, which has been experimentally observed by others as discussed in the introduction. To illustrate the overlap of surface diffraction spots, the cartoon in Figure 6.5 shows the patterns for the 5x2, RT5, and 5x5 within one reciprocal space surface unit

cell. Spots solely belonging to the 5x5 pattern are not present in Figure 6.4 nor are there any other experimental diffraction pattern taken leading to the conclusion that only the RT5 was found co-existing with the 5x2.

An EDM analysis was done for many sets of DP's obtained from many samples with 5x2 reconstructed surfaces, but ultimately they did not lead to viable results. There was quite a lot of variation in the resulting scattering potential maps between different samples and a model that offered a decent refinement could not be found. One reason to suspect for the difficulty is the possible presence of more than one reconstruction whose spots overlap and therefore their separate intensities cannot be deconvolved.

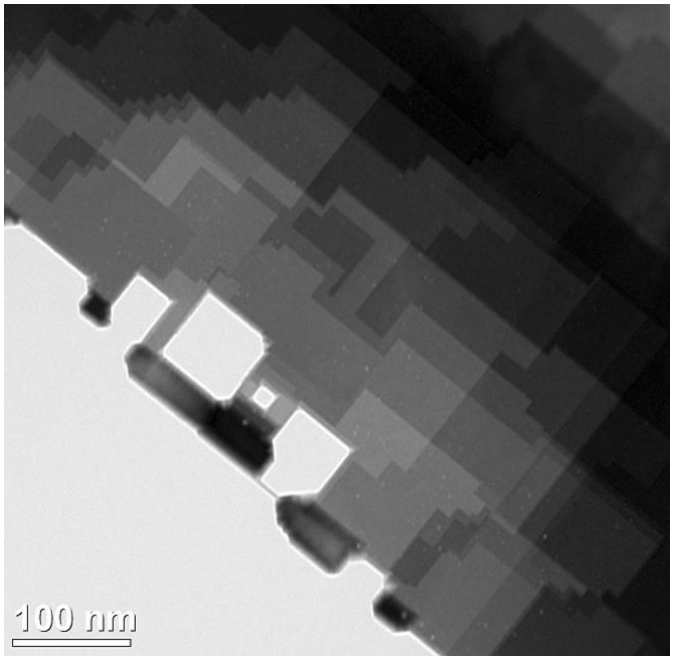

Figure 6.2. Bright field TEM image of the 5x2 reconstructed $LaAlO_3$ (001) surface. Small white spots are visible indicating voids.

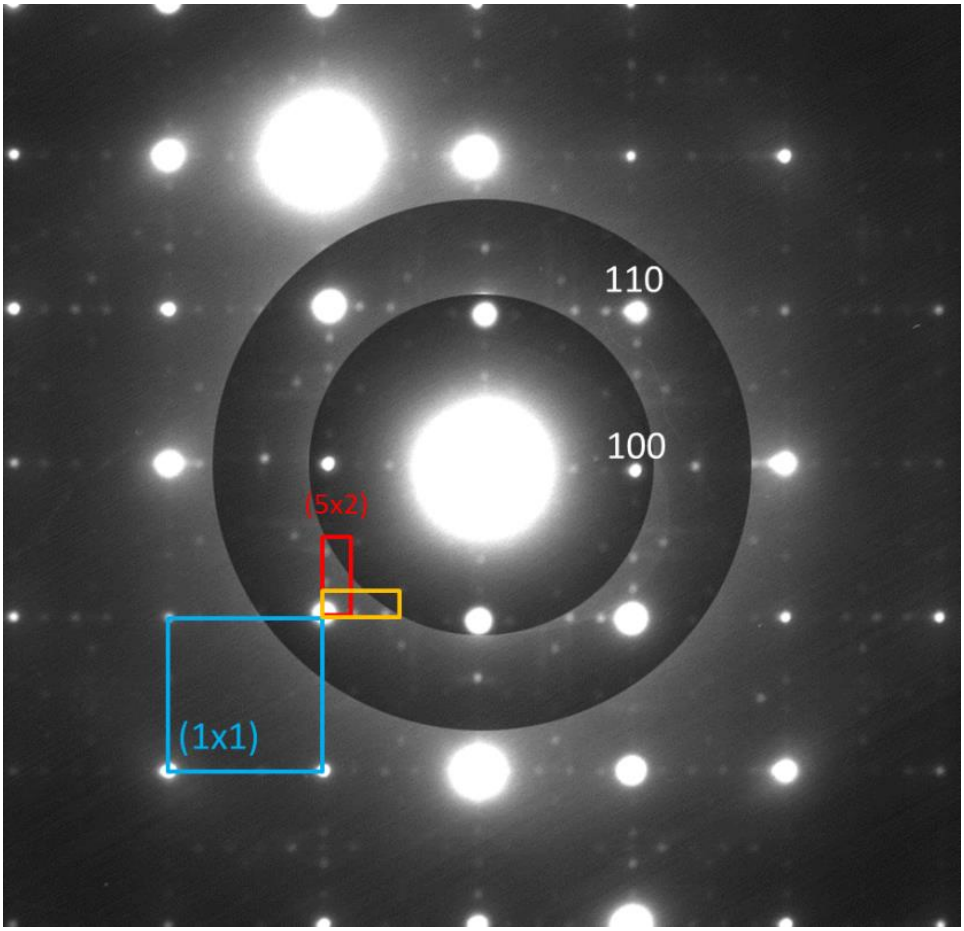

Figure 6.3. Off-zone TED pattern of $LaAlO_3$ (001) showing the two domains of the 5x2 surface reconstruction. The 1x1 surface cell is outlined in blue with the 5x2 cell in red and 2x5 cell in yellow.

Annealing in flowing "dry" oxygen was also attempted, but did not produce a reconstruction. A BF TEM image of the surface annealed in oxygen is shown in Figure 6. Its surface appears smooth and recovered from any damage imparted during sample preparation, but lacks any faceting. It is possible the lack of H_2O in the annealing environment is why a 5x2 reconstruction was not formed.

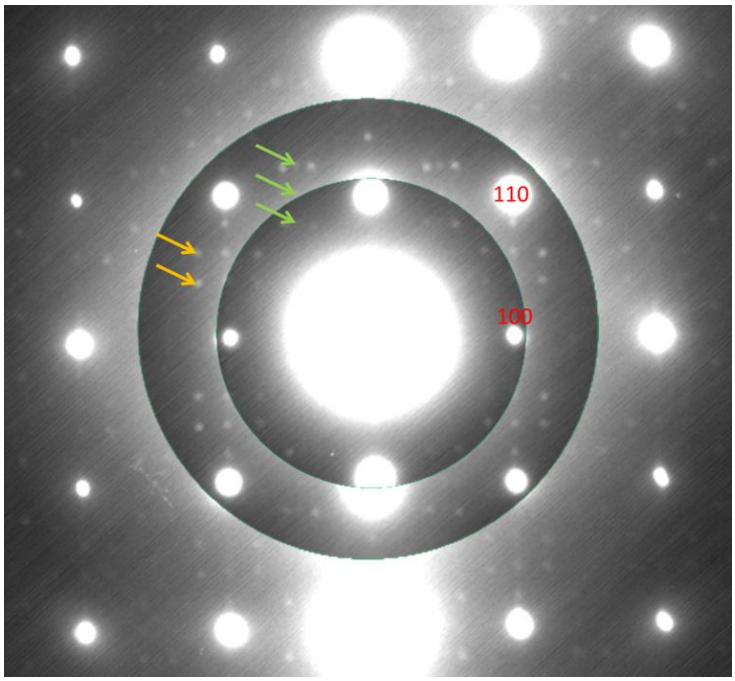

Figure 6.4. Off-zone TED pattern of $LaAlO_3$ (001) exhibiting 5x2 reconstruction spots with a second reconstruction. Green arrows point to diffraction spots that belong to the 5x2 surface while the orange arrows point to spots belong to a (√5x√5)R26.6° or 5x5 surface reconstruction. Refer to Figure 6.5 for spot patterns.

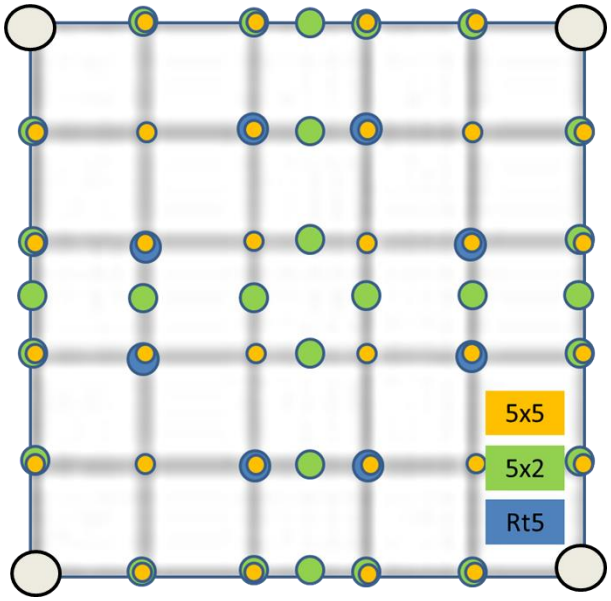

Figure 6.5. Cartoon 1x1 surface cell in reciprocal space showing the diffraction pattern for three sets of reconstructions; orange represents 5x5, green for 5x2, blue for (√5x√5)R26.6°, and white circles at the corners are bulk spots.

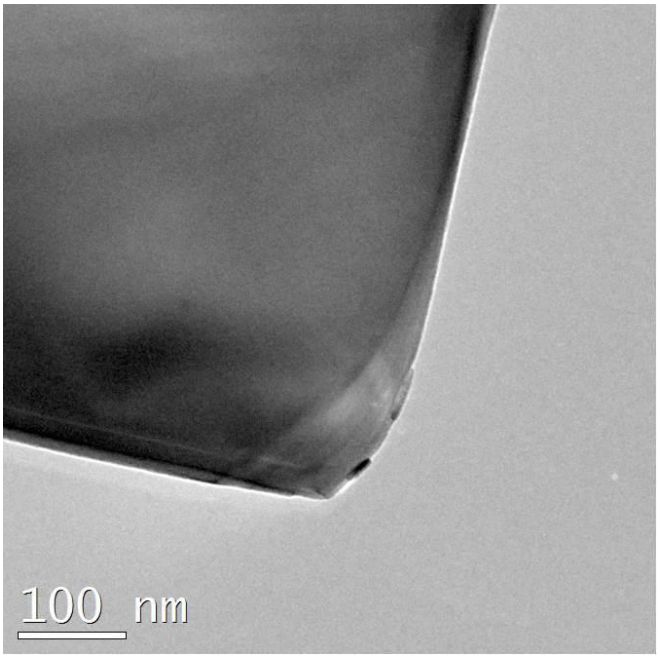

Figure 6.6. Bright-field TEM image of $LaAlO_3$ (001) sample annealed in dry oxygen at 1350°C for 3hr.

6.4.2. X-Ray Photoelectron Spectroscopy

At each angle, spectra of the Al 2p and La 4d peaks regions were recorded and fit using XPSPEAK peak fitting software as detailed in Chapter 2. The total peak sum area for each was found and adjusted by the atomic scattering factor for each element; 2 for La and 0.185 for Al. The presence of satellite peaks arising from the Al 2s line that would overlap the La 4d region was investigated and if present, would have a negligible effect on the overall area of the La peak. The La 4d region was fit with two sets of 3/2 and 5/2 peaks; each set was constrained to have equal full-half-width-maximums (FWHM) and a 3:2 ratio of peak area for 3/2:5/2. The results of peak fitting are tabulated in Table 6.1.

The atomic concentration of Al (C_{Al}) was calculated as $C_{Al} = I_{Al}/(I_{Al}+I_{La})$ where I_{Al} and I_{La} are the total peak areas of Al and La, respectively. Similarly the concentration of La was calculated as $C_{La} = I_{La}/(I_{Al}+I_{La})$. Figure 6.7 plots the concentration of Al and La versus angle with both concentrations normalized to 0.5 at 0°. It is immediately noticeable that the concentration between Al and La is oscillating at least up to around 55°. Looking at the data a different way, Figure 6.8 shows the normalized intensity signals for Al and La varying with angle. Small peaks can be seen at approximately 10, 35, and 55°. The angular dependent asymmetries are most likely due to a photoelectron diffraction effect seen in angle-resolved XPS experiments for single-crystals [112]. The effect causes enhanced intensities corresponding to certain principal crystallographic planes [113]. It is interesting to compare this to the XPS results for the LAO (110) 3x1 surface discussed in Chapter 5, which show a smooth exponential increase for the intensity of Al relative to La with increasingly grazing angles (Figure 5.3) clearly indicating an Al-rich surface. The fact that effects of photoelectron diffraction are observed for the 5x2, but not for the LAO (110) 3x1 could indicate the 5x2 surface structure has not significantly deviated from the bulk structure similar to the LAO (001) RT5 reconstruction which consists of a bulk surface layer with La vacancies.

At higher angles, the surface does appear to be Al-rich for the 5x2 as well. To compare, the sum of intensity from a depth profile of alternating layers of Al and La was computed as illustrated in Figure 6.9. The intensity was calculated for each layer below the surface layer as $I_n=\exp(-nd/(\lambda\cos\theta))$ where n is the layer, d is the spacing between layers, in this case 1.895 Å for $LaAlO_3$ in the [001] direction, λ is the electron attenuation length, and θ is the polar angle.

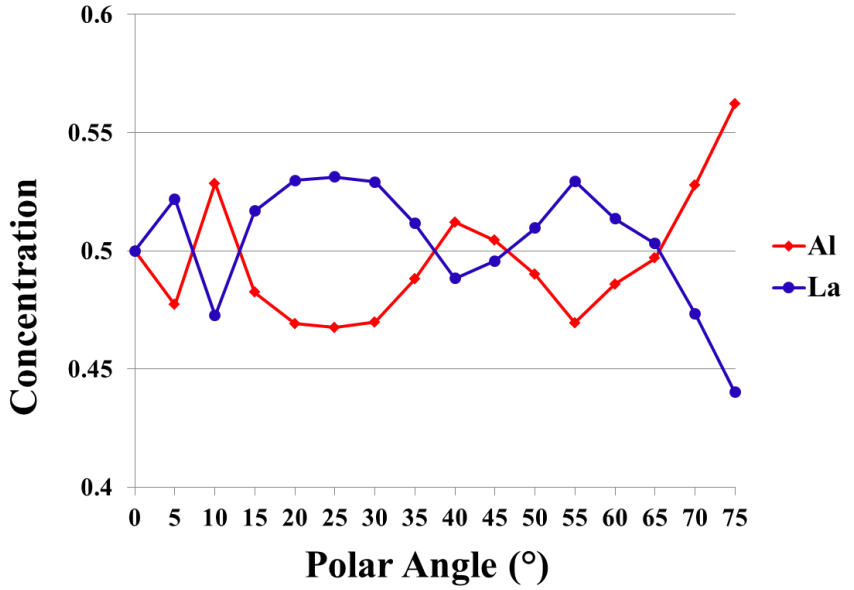

Figure 6.7. Experimental angle-resolved XPS results showing concentration versus polar angle. Intensities were corrected with atomic scattering factors and normalized to 0.5 at 0°.

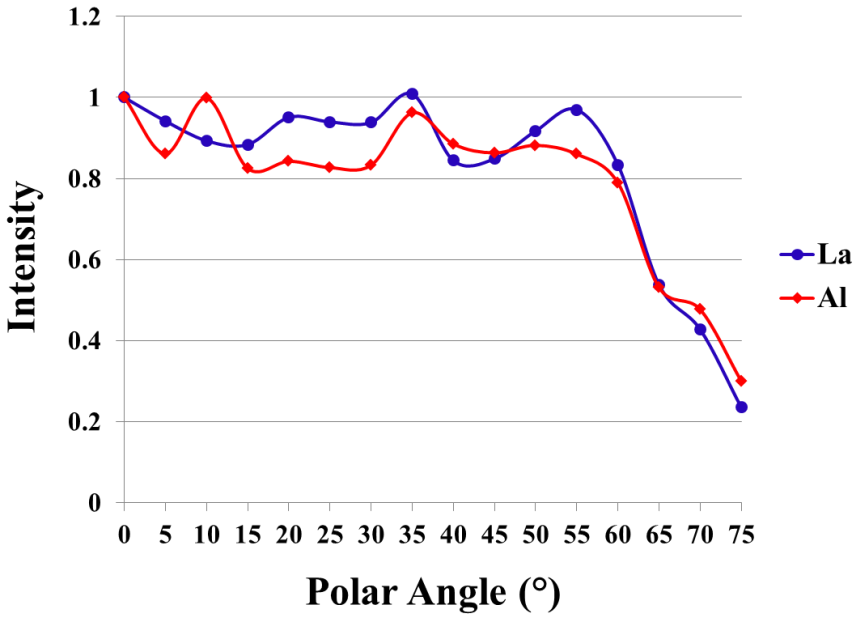

Figure 6.8. XPS normalized intensities of Al and La signal at varying polar angles.

Distinct attenuation length values for each element at each depth and angle were taken from the NIST Electron Effective-Attenuation-Length Database [114] and result in a less smooth calculated intensity line. The surface layer is not affected by attenuation and thus is only based on the composition.

The best fit was found for a surface layer close to 0.5 occupancy shown in Figure 6.10, where the concentration of Al is equal to $I_{Al}/(I_{Al}+I_{La})$ and similarly, the concentration of La is equal to $I_{La}/(I_{Al}+I_{La})$. The thinner red and blue lines show the concentrations of Al and La, respectively, computed from the depth profile for surface Al layers with concentrations of 0.25, 0.4, 0.5, 0.6, 0.75 and 1. Because of the peaks in the experimental intensities, the concentrations versus angles were normalized to 0.5 at 55° to compare the fits at more grazing angles. As the angle becomes more grazing, less layers are being sampled and the effect of photoelectron diffraction should be minimized. This angular range is shown in the bottom plot. It is hard to tell from just the Al concentration lines which one best fits the experimental, but it appears to be between 0.5 and 1. More telling is the La concentration lines which show a greater variance in concentration with respect to the Al surface layer. The best fit is close to a 0.5 occupancy Al surface layer.

It is not a surprise that a concentration of 0.5 Al would be the best fit because ½ of an AlO_2 layer would offset the polar nature of the (001) created by its alternating layers of LaO (1+) and AlO_2 (1-). Extrapolating to a 5x2 cell (ten 1x1 surface unit cells) would require 5 Al atoms (1/2 Al per 1x1) and 10 oxygen atoms.

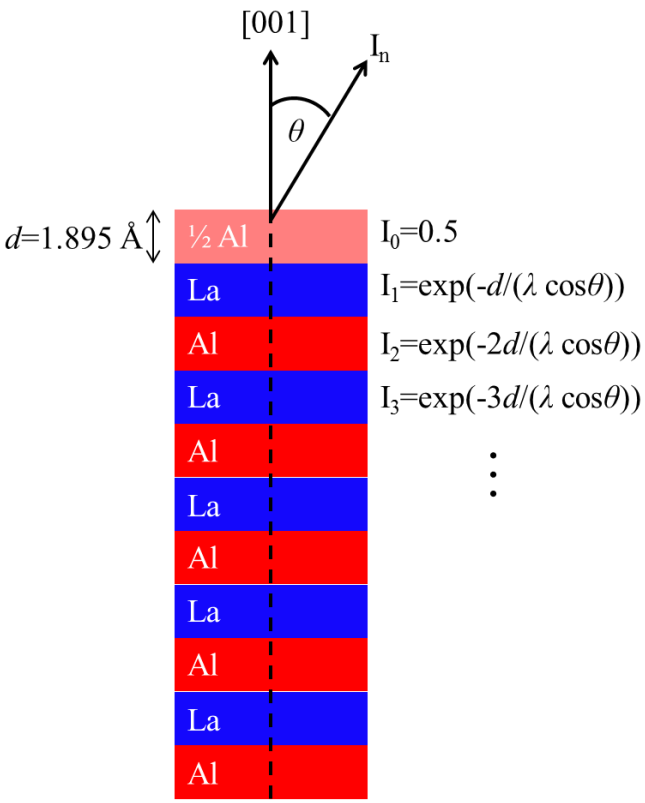

Figure 6.9. Depth profile perpendicular to the [001] direction for $LaAlO_3$ made up of a surface layer of ½ monolayer Al followed by alternating layers La and Al with a *d*-spacing of 1.895Å. The observed intensity of a photoelectron ejected from layer *n* at a depth *n*d* can be approximated as an exponential decay: $I_n=\exp(-nd/(\lambda\cos\theta))$ where λ is the electron attenuation length and θ is the polar angle between the surface normal and detector.

An XPS spectrum of the O 1s region was recorded and is displayed in Figure 6.11. A high-binding energy shoulder was not observed in the spectra, unlike the LAO (110) 3x1 O 1s region which showed a shoulder 1.9 eV higher in binding energy than the main peak. Here for the 5x2, the O 1s region was fit with two peaks and the secondary peak denoted as II is separated from the main peak (I) by 0.5 eV, which does not indicate hydroxyl groups at the surface.

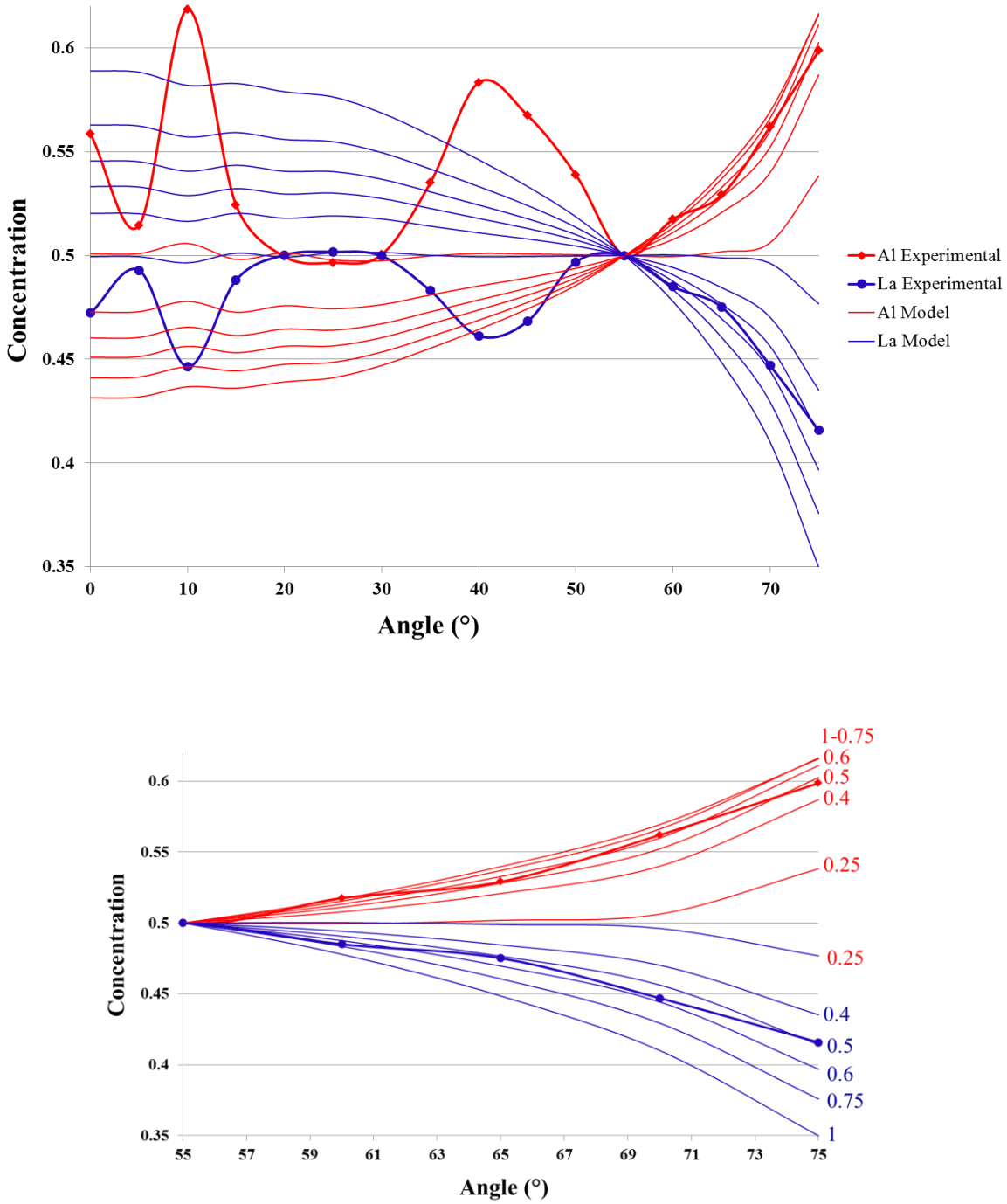

Figure 6.10. (Top) Experimental angle-resolved XPS results showing concentration versus polar angle and the calculated Al and La concentration for the model shown in Figure 6.9 having a surface Al layer with concentrations of 0.25, 0.4, 0.5, 0.6, 0.75 and 1. Experimental intensities were corrected with atomic scattering factors. Both experimental and calculated concentrations were normalized to 0.5 at 55° to avoid photoelectric diffraction effects. The (bottom) plot zooms in on the angular range of interest (55-75°). Numbers along the right-side correspond to the Al surface monolayer concentration.

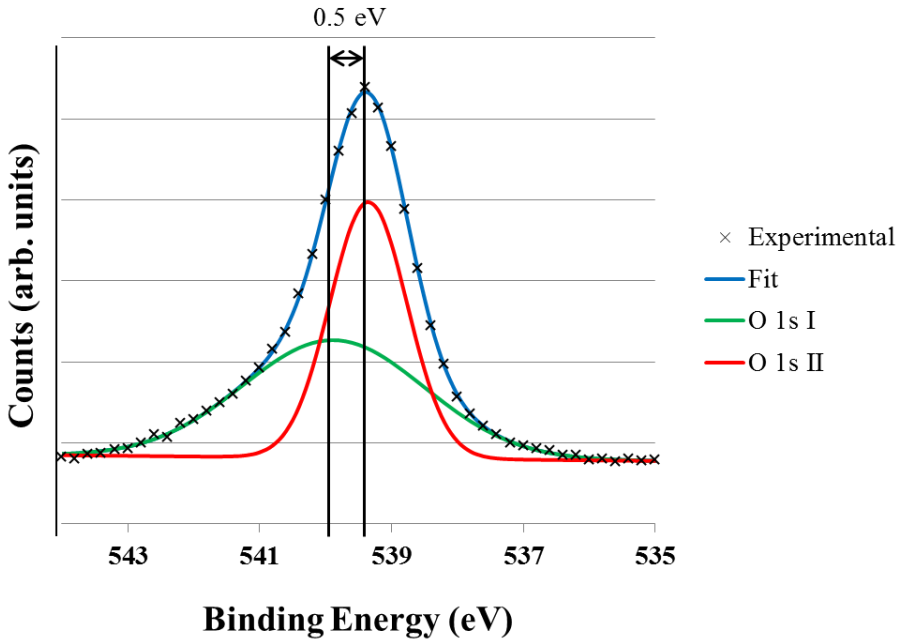

Figure 6.11. XPS spectrum of the oxygen 1s peak with the detector normal to the surface.

6.5. Conclusions

The $LaAlO_3$ (001) 5x2 reconstructed surface has been observed via transmission electron diffraction on TEM samples annealed in air over a range temperatures and times has been reported here for the first time. An EDM analysis was done for several sets of recorded diffraction patterns; however the results failed to lead to an atomic surface structure. X-Ray photoelectron spectra were collected over a range of detector-to-surface-normal angles elucidating an Al-rich surface layer. XPS intensities were calculated for a model of alternating Al and La layers over a range of grazing angles and varying amounts of Al in the top surface layer. An Al concentration of 0.5 was found to give the best fit to experimental results.

Table 6.1 Peak fitting for the Al 2p and La 4d regions showing the binding energy (BE), full-width-half-maximum (FWHM), and area at each angle listed (0° being the detector normal to the surface). Peaks that were too small to fit are marked with an X.

	La 4d 3/2 I			La 4d 5/2 I			La 4d 3/2 II			La 4d 5/2 II			Al 2p		
Angle (°)	BE	FWHM	Area	BE	FWHM	Area	BE	FWHM	Area	BE	FWHM	Area	BE	FWHM	Area
0	115.1	2.1	9331	112.1	2.1	6221	117.2	3.7	3295	113.5	3.7	2197	83.6	1.7	1873
5	115.1	2.0	8930	112.1	2.0	5953	117.0	4.0	3224	114.0	4.0	2150	83.6	1.8	1613
10	115.0	2.1	8423	112.0	2.1	5615	117.2	3.6	3026	113.3	3.6	2018	83.5	1.7	1870
15	115.0	2.1	8510	112.0	2.1	5673	117.2	3.5	2776	113.1	3.5	1851	83.5	1.8	1545
20	114.8	2.1	8919	111.8	2.1	5946	117.0	3.6	3218	112.9	3.6	2145	83.3	1.8	1578
25	114.8	2.0	8841	111.8	2.0	5894	117.0	3.6	3233	113.0	3.6	2155	83.2	1.7	1549
30	114.8	2.1	8865	111.8	2.1	5910	116.9	3.6	3124	113.0	3.6	2083	83.3	1.6	1560
35	114.8	2.1	9695	111.7	2.1	6466	117.1	3.5	3078	112.8	3.5	2052	83.2	1.8	1802
40	114.8	2.1	8265	111.7	2.1	5510	117.1	3.5	2546	113.0	3.5	1697	83.2	1.8	1658
45	114.8	2.1	7957	111.8	2.1	5305	117.1	3.6	2761	113.0	3.6	1841	83.3	1.7	1617
50	114.8	2.0	8735	111.8	2.0	5823	116.8	3.8	3377	113.2	3.8	2251	83.3	1.8	1652
55	114.8	2.1	9314	111.8	2.1	6209	117.1	3.4	3137	113.0	3.4	2092	83.3	1.8	1611
60	115.0	2.1	7932	111.9	2.1	5288	117.2	3.4	2653	113.0	3.4	1768	83.4	1.7	1478
65	114.9	2.0	5042	111.9	2.0	3362	117.0	3.3	1873	112.8	3.3	1249	83.4	1.9	994
70	114.9	1.9	4051	116.8	1.9	2701	116.8	4.0	1536	13.6	4.0	1024	83.4	1.7	893
75	115.1	2.3	3060	112.0	2.3	2040	X	X	X	X	X	X	83.4	1.8	561

7. Conclusions and Suggestions for Future Work

There is an accumulating amount of evidence, as presented in Chapter 3, supporting the TiO_2 double-layer $SrTiO_3$ (001) surface reconstructions which are characterized by a network of corner- or edge-sharing TiO_x units in varying stoichiometries. The network can range from ordered, like the 2x1 and c(4x2), to pseudo-ordered, like the c(6x2), to a disordered glass-like surface layer made up of TiO_x units. In all cases, there are additional surface Ti atoms that are under-coordinated relative to bulk Ti which are octahedrally coordinated. The RT13 reconstruction presented in this work in Chapter 4 is yet another example of a DL structure with a honeycomb-like 2D network of TiO_x. The RT13 also points to the fact that all of the DL structures can be thought of in terms of a basic 2x1 building block. These 2x1 surface building blocks can be constructed in periodic ways resulting in a wide range of possible TiO_2 surface stoichiometries.

Chapters 5 and 6 turned to the discussion of $LaAlO_3$ surfaces. It is clear that as more research dedicated to studying $LaAlO_3$ surfaces is conducted and more surface reconstructions are discovered, the overall picture becomes more and more complicated, not unlike $SrTiO_3$. However, with this research comes more opportunities for finding similarities between $LaAlO_3$ and $SrTiO_3$ surfaces. An example of this is presented in Chapter 5, where it is likely that the $LaAlO_3$ (110) 3x1 reconstruction forms a hydrated 2D network of 6- and 8-corner-sharing AlO_x polyhedra just as the $SrTiO_3$ (110) surface forms a 2D network of 6- and 8-corner-sharing TiO_x polyhedra [50]. Indeed, the fact that the $SrTiO_3$ (110) structure was known led to the $LaAlO_3$ 3x1 structures in Chapter 5.

Going beyond just the surface structure and looking to the $SrTiO_3/LaAlO_3$ interface, when we take into account the $SrTiO_3$ (110) nx1 reconstructions, the $SrTiO_3$ double layer reconstructions as well as the (001) pseudo-ordered glass-like reconstructions, it becomes clear that to obtain interfaces in these oxides suitable for electronic applications will require substantial care to control the surface excess of TiO_2 and/or Al_2O_3 as otherwise disordered network structures are going to form. Note that these more open disordered structures would not be apparent in images obtained using conventional cross-sectional HREM techniques, so could well have gone undetected. The same is true, albeit less controllably for grain boundaries in ceramics where disordered interfacial structures have been commonly reported in the past [115-118]. While it has been assumed that these are often due to depressed melting points of disordered regions with impurities at the interface, in some cases these might be the thermodynamic lowest energy configuration.

As shown in Table 3.1, a variety of surface reconstructions have been observed and reported on the $SrTiO_3$ (001) surface under the same experimental conditions. Similarly, the $LaAlO_3$ (001) 5x2 and RT5 reconstructions formed under seemingly the same conditions. This has been the experience within the L. D. Marks group, as well, where graduate students can obtain multiple surface reconstructions from samples seemingly prepared the same way. With respect to TEM sample preparation, the mechanical thinning is done by hand to an approximate thickness of 100 microns, but can vary across the sample. Further thinning with a dimple grinder is performed until the sample center is approximately 20 microns, however the variability in thickness directly affects how much time the sample undergoes Argon ion polishing to become electron transparent. This leads to varying degrees of inflicted damage, and in other words, different starting points from which structural rearrangements will occur during annealing.

Future surface structure investigations should pay particular attention to monitoring sample preparation aspects, such as the Argon ion beam energy, beam angle, and time a sample is exposed to ion beam thinning. Additionally, during annealing, the humidity or H_2O partial pressure should be monitored given the importance water adsorption may play as a stabilization mechanism for $SrTiO_3$ surfaces [119, 120]. It would also be likely that any conclusions ascertained from a more rigid sample preparation study could provide insight into the surface structure. Related to this, a question that arises when investigating the connection between preparation conditions and surface structure, is reproducibility. How many times must a surface structure be obtained to deem the structure reproducible?

Another avenue of further study relating to sample preparation would be to more closely mimic the experimental conditions reported using other analytical techniques for investigating $SrTiO_3$ surfaces, such as STM, that include Argon ion polishing and annealing of Nb-doped $SrTiO_3$ samples in UHV, as described in reference [121]. Alternatively, other methods of TEM sample preparation that provide greater control and lead to more uniform sample creation, such as Focused Ion Beam (FIB) thinning, should also be investigated. For example, it has been shown that high-quality TEM samples of oxide materials with a controlled thickness can be obtained using a low voltage FIB method [122].

While there is yet much unknown about $SrTiO_3$ and $LaAlO_3$, for example, a structure solution for the $LaAlO_3$ (001) 5x2 presented in Chapter 6, it is also important to examine other oxide materials, such as perovskites $BaTiO_3$ or $CaTiO_3$. A number of surface reconstructions have been reported for $BaTiO_3$ (001), including a 2x2 [123], c(2x2) [123, 124], 3x1 [123], $(\sqrt{5}x\sqrt{5})R26.6°$ [125, 126], and $(\sqrt{13}x\sqrt{13})R37.7°$ [124], however, the structures and compositions are yet undetermined. A first-principle study of the (001) surfaces of $CaTiO_3$,

$BaTiO_3$, and $SrTiO_3$ seeking to obtain rules of surface properties based on different *A*-site atoms in $ATiO_3$ perovskites found that CaO- and TiO_2-terminated can equally exist on the (001) surface of cubic $CaTiO_3$, unlike $SrTiO_3$ [127]. Knowledge of $SrTiO_3$ and $LaAlO_3$ surface reconstructions, as well as refined experimental and computational investigative procedures, can be applied to $BaTiO_3$, $CaTiO_3$, and other lesser-studied perovskites to aid in structure solutions, just as the $SrTiO_3$ (110) 3x1 reconstruction aided in identifying the $LaAlO_3$ (110) 3x1 presented in Chapter 5. It would be interesting to investigate if the 3x1 AlO_x network structure on $SrTiO_3$ and $LaAlO_3$ (110) surfaces extended to the (110) surface of other ABO_3 perovskite materials.

One future direction for this research is to apply the acquired surface structure knowledge of single-crystal model systems to application-based systems. For instance, studies investigating the catalytic properties of $SrTiO_3$ will most likely be conducted with $SrTiO_3$ in the form of nanoparticles to maximize the material's surface area, rather than a single crystal. Recently, $SrTiO_3$ (001) surface reconstructions originally observed and solved using single-crystal samples, were identified on the surface of $SrTiO_3$ nanocubes by Lin *et. al.* [128]. The cubes, with [001]-type faces, can be synthesized three different ways, each resulting in different surfaces. Simulated HREM images of the RT13 reconstruction were compared to, and showed high agreement with experimental HREM images of nanocube surfaces synthesized with oleic acid, helping lead to the conclusion that the surface was a glass-like mixture of RT13 and RT5.

The work by Lin *et. al.* [128] illustrates how surface structures solved via TEM diffraction and Direct Methods from single crystal samples can be instrumental to interpreting HREM images of nanostructures. This approach to understanding oxide surfaces in a more application-based form, such as nanocubes, could also be applied to other materials. For example, sub-10 nm $BaTiO_3$ nanocubes have been successfully synthesized using a solvothermal

method with oleic acid as the surfactant [129], or, perhaps a similar a synthesis method for $LaAlO_3$ nanocubes could be investigated. Regardless of the specific oxide in question, understanding how that oxide's surface behaves at a fundamental level, by studying single-crystal systems, will greatly aid in not only understanding the surfaces of polycrystalline or nanoparticle systems, but also, in the ultimate goal of engineering the surfaces for a particular desired property.

References

1. Erdman, N., et al., *The structure and chemistry of the TiO_2-rich surface of $SrTiO_3$ (001).* Nature, 2002. **419**(6902): p. 55-58.

2. Kawasaki, M., et al., *Atomic Control of the $SrTiO_3$ Crystal Surface.* Science, 1994. **266**(5190): p. 1540-1542.

3. Kawasaki, M., *Atomic control of $SrTiO_3$ surface for perfect epitaxy of perovskite oxides.* Applied Surface Science, 1996. **107**: p. 102-106.

4. Jiang, Q.D. and J. Zegenhagen, *$SrTiO_3$ (001) surfaces and growth of ultra-thin $GdBa_2Cu_3O_{7-x}$ films studied by LEED/AES and UHV-STM.* Surface Science, 1995. **338**(1-3): p. L882-L888-L882-L888.

5. Ishibashi, T., et al., *Submicron-size fabrication of BSCCO thin films by using patterned substrates.* IEEE Transactions on Applied Superconductivity, 1999. **9**(2): p. 2383-2386.

6. Zegenhagen, J., T. Haage, and Q.D. Jiang, *Microscopic structure and structuring of perovskite surfaces and interfaces: $SrTiO_3$, $RBa_2Cu_3O_7$.* Applied Physics A: Materials Science & Processing, 1998. **67**(6): p. 711-722.

7. Droopad, R., et al., *Development of high dielectric constant epitaxial oxides on silicon by molecular beam epitaxy.* Materials Science and Engineering: B, 2001. **87**(3): p. 292-296.

8. Eisenbeiser, K., et al., *GaAs MESFETs fabricated on Si substrates using a $SrTiO_3$ buffer layer.* Electron Device Letters, IEEE, 2002. **23**(6): p. 300-302.

9. McKee, R.A., F.J. Walker, and M.F. Chisholm, *Crystalline Oxides on Silicon: The First Five Monolayers.* Physical Review Letters, 1998. **81**: p. 3014-3017.

10. Sharma, R., A. Kumar, and J. Anthony, *Advances in high-k dielectric gate materials for future ULSI devices.* JOM Journal of the Minerals, Metals and Materials Society, 2001. **53**(6): p. 53-55.

11. Liang, Y. and D.A. Bonnell, *Atomic structures of reduced $SrTiO_3$ (001) surfaces.* Surface Science, 1993. **285**(3): p. L510-L516-L510-L516.

12. Castell, M.R., *Nanostructures on the $SrTiO_3$(001) surface studied by STM.* Surface Science, 2002. **516**(1-2): p. 33-42.

13. Santander-Syro, A.F., et al., *Two-dimensional electron gas with universal subbands at the surface of $SrTiO_3$.* Nature, 2011. **469**(7329): p. 189-193.

14. Ohtomo, A. and H.Y. Hwang, *A high-mobility electron gas at the $LaAlO_3/SrTiO_3$ heterointerface.* Nature, 2004. **427**(6973): p. 423-426.

15. Singh-Bhalla, G., et al., *Built-in and induced polarization across $LaAlO_3/SrTiO_3$ heterojunctions.* Nat Phys, 2011. **7**(1): p. 80-86.

16. Müller, K. and H. Burkard, *$SrTiO_3$: An intrinsic quantum paraelectric below 4 K.* Physical Review B, 1979. **19**(7): p. 3593-3602.

17. Mavroides, J.G., J.A. Kafalas, and D.F. Kolesar, *Photoelectrolysis of water in cells with $SrTiO_3$ anodes.* Applied Physics Letters, 1976. **28**(5): p. 241-241.

18. Cardona, M., *Optical Properties and Band Structure of $SrTiO_3$ and $BaTiO_3$.* Physical Review, 1965. **140**(2A): p. A651-A655-A651-A655.

19. Schooley, J., W. Hosler, and M. Cohen, *Superconductivity in Semiconducting $SrTiO_3$.* Physical Review Letters, 1964. **12**(17): p. 474-475.

20. Chen, Y.F., et al., *Growth and characterization of 2 inch double-sided $Tl_2Ba_2CaCu_2O_8$ thin films on $LaAlO_3$ substrates.* Superconductor Science and Technology, 2008. **21**(8): p. 085005-085005.

21. Schneidewind, H., et al., *TlBaCaCuO-(2212) thin films on lanthanum aluminate and sapphire substrates for microwave filters.* Superconductor Science and Technology, 2001. **14**(4): p. 200-212.

22. Simon, R.W., et al., *Low-loss substrate for epitaxial growth of high-temperature superconductor thin films.* Applied Physics Letters, 1988. **53**(26): p. 2677-2677.

23. O'Bryan, H.M., et al., *Thermal analysis of rare earth gallates and aluminates.* Journal of Materials Research, 2011. **5**(01): p. 183-189.

24. Edon, V., *Investigation of lanthanum and hafnium-based dielectric films by X-ray reflectivity, spectroscopic ellipsometry and X-ray photoelectron spectroscopy.* Thin Solid Films, 2008. **516**(22): p. 7974-7974.

25. Klenov, D.O., et al., *The Interface between Single Crystalline (001) $LaAlO_3$ and (001) Silicon.* Japanese Journal of Applied Physics, 2005. **44**(No. 20): p. L617-L619-L617-L619.

26. Zhao, Y., et al., *Development of a new series of buffer layers for REBCO coated conductors.* Physica C: Superconductivity, 2007. **463–465**(0): p. 574-579.

27. Park, B.-E. and H. Ishiwara, *Electrical properties of $LaAlO_3$/Si and $Sr_{0.8}Bi_{2.2}Ta_2O_9/LaAlO_3$/Si structures.* Applied Physics Letters, 2001. **79**(6): p. 806-808.

28. Valden, M., et al., *Reactivity of Pd/Al_2O_3, Pd/La_2O_3–Al_2O_3 and $Pd/LaAlO_3$ Catalysts for the Reduction of NO by CO: CO and NO Adsorption.* Journal of Catalysis, 1996. **161**(2): p. 614-625.

29. Dunn, D.N., P. Xu, and L.D. Marks, *Problems with the use of surface reconstructions as indicators of a well-ordered surface.* Journal of Crystal Growth, 1992. **125**(3–4): p. 543-547.

30. Marks, L.D., W. Sinkler, and E. Landree, *A feasible set approach to the crystallographic phase problem.* Acta Crystallographica Section A Foundations of Crystallography, 1999. **55**(4): p. 601-612.

31. Usón, I. and G.M. Sheldrick, *Advances in direct methods for protein crystallography.* Current Opinion in Structural Biology, 1999. **9**(5): p. 643-648.

32. Kienzle, D.M. and L.D. Marks, *Surface transmission electron diffraction for $SrTiO_3$ surfaces.* CrystEngComm, 2012.

33. Kilaas, R., L.D. Marks, and C.S. Own, *EDM 1.0: Electron direct methods.* Ultramicroscopy, 2005. **102**(3): p. 233-237.

34. Hohenberg, P. and W. Kohn, *Inhomogeneous Electron Gas.* Physical Review, 1964. **136**(3B): p. B864-B871-B864-B871.

35. Kohn, W. and L.J. Sham, *Self-Consistent Equations Including Exchange and Correlation Effects.* Physical Review, 1965. **140**(4A): p. A1133-A1138-A1133-A1138.

36. Perdew, J.P. and Y. Wang, *Accurate and simple analytic representation of the electron-gas correlation energy.* Physical Review B, 1992. **45**(23): p. 13244-13249.

37. Perdew, J.P. and W. Yue, *Accurate and simple density functional for the electronic exchange energy: Generalized gradient approximation.* Physical Review B, 1986. **33**(12): p. 8800-8802.

38. Blaha, P., et al., *WIEN2k, An Augmented Plane Wave Plus Local Orbitals Program for Calculating Crystal Properties*, K. Schwarz, Editor 2001: Vienna University of Technology, Austria.

39. Perdew, J.P., K. Burke, and M. Ernzerhof, *Generalized Gradient Approximation Made Simple.* Physical Review Letters, 1996. **77**(18): p. 3865-3865.

40. Mattsson, A.E. and D.R. Jennison, *Computing accurate surface energies and the importance of electron self-energy in metal/metal-oxide adhesion.* Surface Science, 2002. **520**(1–2): p. L611-L618-L611-L618.

41. Perdew, J.P., et al., *Restoring the Density-Gradient Expansion for Exchange in Solids and Surfaces.* Physical Review Letters, 2008. **100**(13): p. 136406.

42. Adamo, C., G.E. Scuseria, and V. Barone, *Accurate excitation energies from time-dependent density functional theory: Assessing the PBE0 model.* The Journal of Chemical Physics, 1999. **111**(7): p. 2889-2899.

43. Perdew, J.P., M. Ernzerhof, and K. Burke, *Rationale for mixing exact exchange with density functional approximations.* The Journal of Chemical Physics, 1996. **105**(22): p. 9982-9982.

44. Anisimov, V.I., J. Zaanen, and O.K. Andersen, *Band theory and Mott insulators: Hubbard U instead of Stoner I.* Physical Review B, 1991. **44**(3): p. 943-954.

45. Tao, J., et al., *Climbing the Density Functional Ladder: Nonempirical Meta–Generalized Gradient Approximation Designed for Molecules and Solids.* Physical Review Letters, 2003. **91**(14).

46. Staroverov, V., et al., *Comparative assessment of a new nonempirical density functional: Molecules and hydrogen-bonded complexes.* The Journal of Chemical Physics, 2003. **119**(23): p. 12129-12137.

47. Perdew, J.P., et al., *Workhorse Semilocal Density Functional for Condensed Matter Physics and Quantum Chemistry.* Physical Review Letters, 2009. **103**(2): p. 026403.

48. 1996, XPSPEAK 95 v. 2 Hong Kong.

49. Chiaramonti, A.N., et al., *Time, temperature, and oxygen partial pressure-dependent surface reconstructions on $SrTiO_3$ (111): A systematic study of oxygen-rich conditions.* Surface Science, 2008. **602**(18): p. 3018-3025.

50. Enterkin, J.A., et al., *A homologous series of structures on the surface of $SrTiO_3$(110).* Nature Materials, 2010. **9**: p. 245-248.

51. Henrich, V., G. Dresselhaus, and H. Zeiger, *Surface defects and the electronic structure of $SrTiO_3$ surfaces.* Physical Review B, 1978. **17**(12): p. 4908-4921.

52. Martin R, C., *Scanning tunneling microscopy of reconstructions on the SrTiO3(0 0 1) surface.* Surface Science, 2002. **505**(0): p. 1-13.

53. Andersen, J.E.T. and P.J. Moller, *Impurity-induced 900 °C (2×2) surface reconstruction of $SrTiO_3$ (100).* Applied Physics Letters, 1990. **56**(19): p. 1847-1847.

54. van der Heide, P.A.W., et al., *X-ray photoelectron spectroscopic and ion scattering study of the $SrTiO_3$ (001) surface.* Surface Science, 2001. **473**(1-2): p. 59-70.

55. Charlton, G., et al., *Surface relaxation of $SrTiO_3$ (001).* Surface Science, 2000. **457**(1-2): p. L376-L380-L376-L380.

56. Cord, B. and R. Courths, *Electronic study of $SrTiO_3$ (001) surfaces by photoemission.* Surface Science, 1985. **162**(1-3): p. 34-38.

57. Castell, M.R., *Scanning tunneling microscopy of reconstructions on the $SrTiO_3$ (001) surface.* Surface Science, 2002. **505**: p. 1-13.

58. Erdman, N., et al., *Surface structures of $SrTiO_3$ (001): a TiO_2-rich reconstruction with a c(4 x 2) unit cell.* Journal of the American Chemical Society, 2003. **125**(33): p. 10050-10056.

59. Naito, M. and H. Sato, *Reflection high-energy electron diffraction study on the $SrTiO_3$ surface structure.* Physica C: Superconductivity, 1994. **229**(1-2): p. 1-11.

60. Matsumoto, T., *STM-imaging of $SrTiO_3$ (100) surface with atomic-scale resolution.* Surface Science, 1992. **278**(3): p. L153-L158-L153-L158.

61. Moller, P.J., S.A. Komolov, and E.F. Lazneva, *Selective growth of a MgO(100)-c(2x2) superstructure on a $SrTiO_3$(100)-(2x2) substrate.* Surface Science, 1999. **425**(1): p. 15-21.

62. Kubo, T. and H. Nozoye, *Surface structure of $SrTiO_3$(100).* Surface Science, 2003. **542**(3): p. 177-191.

63. Lanier, C.H., et al., *Atomic-scale structure of the $SrTiO_3$(001)-c(6x2) reconstruction: Experiments and first-principles calculations.* Physical Review B, 2007.

64. Kubo, T. and H. Nozoye, *Surface Structure of $SrTiO_3$(100)-(Rt.5×Rt.5)-R26.6°.* Physical Review Letters, 2001. **86**(9): p. 1801-1804.

65. Tanaka, H., et al., *Surface Structure and Electronic Property of Reduced $SrTiO_3$ (100) Surface Observed by Scanning Tunneling Microscopy/Spectroscopy.* Japanese Journal of Applied Physics, 1993. **32**(Part 1, No. 3B): p. 1405-1409.

66. Akiyama, R., et al., *Electric Field and Contact Interactions of Tip with Adenine Molecules on $SrTiO_3$(100)-Rt.5xRt.5 Surfaces.* Japanese Journal of Applied Physics, 1997. **36**(Part 1, No. 6B): p. 3881-3886.

67. Gonzalez, M.S.M., et al., *In situ reduction of (100) $SrTiO_3$.* Solid State Sciences, 2000. **2**: p. 519-524.

68. Newell, D.T., *The surface structure and reconstructions of $SrTiO_3$ (001)*, 2007, Oxford.

69. Fompeyrine, J., et al., *Local determination of the stacking sequence of layered materials.* Applied Physics Letters, 1998. **72**(14): p. 1697-1699.

70. Jiang, Q.D. and J. Zegenhagen, *c(6×2) and c(4×2) reconstruction of $SrTiO_3$(001).* Surface Science, 1999. **425**(2-3): p. 343-354.

71. Lanier, C.H., et al., *Surface reconstruction with a fractional hole (Rt5xRt5)R26.6 $LaAlO_3$ (001).* Physical Review Letters, 2007. **98**(8).

72. Kienzle, D.M., A.E. Becerra-Toledo, and L.D. Marks, *Vacant-Site Octahedral Tilings on $SrTiO_3$ (001), the (Rt.13×Rt.13)R33.7° Surface, and Related Structures.* Physical Review Letters, 2011. **106**(17): p. 176102-176102.

73. Enterkin, J.A., *A Chemical Approach to Understanding Oxide Surface Structure and Reactivity*.2010.

74. Warschkow, O., et al., *TiO_2-rich reconstructions of $SrTiO_3$ (001): a theoretical study of structural patterns.* Surface Science, 2004. **573**(3): p. 446-456.

75. Herger, R., et al., *Surface structure of $SrTiO_3$ (001).* Physical Review B, 2007. **76**(19): p. 195435-195435.

76. Russell, B.C. and M.R. Castell, *Reconstructions on the polar $SrTiO_3$ (110) surface: Analysis using STM, LEED, and AES.* Physical Review B, 2008. **77**(24): p. 245414.

77. Wang, Z., et al., *Evolution of the surface structures on $SrTiO_3$(110) tuned by Ti or Sr concentration.* Physical Review B, 2011. **83**(15): p. 155453-155453.

78. Zachariasen, W.H., *THE ATOMIC ARRANGEMENT IN GLASS.* Journal of the American Chemical Society, 1932. **54**(10): p. 3841-3851.

79. Christensen, S., *Nanoscale Investigation of Platinum Nanoparticles on $SrTiO_3$ Grown via Physical Vapor Deposition and Atomic Layer Desposition*, in *Materials Science and Engineering*2008, Northwestern University.

80. Xu, P., G. Jayaram, and L.D. Marks, *Cross-correlation method for intensity measurement of transmission electron diffraction patterns.* Ultramicroscopy, 1994. **53**(1): p. 15-18.

81. Ciston, J., et al., *Structure and morphology of hydroxylated nickel oxide (111) surfaces.* arXiv:0908.1888, 2009.

82. Marks, L.D., et al., *The small unit cell reconstructions of $SrTiO_3$ (111).* Surface Science, 2009. **603**(14): p. 2179-2187.

83. Sheldrick, G., *A short history of SHELX.* Acta Crystallographica Section A 2008. **64**(1): p. 112-122.

84. Lin, Y., et al., *The (2×2) reconstructions on the $SrTiO_3$ (001) surface: A combined scanning tunneling microscopy and density functional theory study.* Surface Science, 2011. **605**(17-18): p. L51-L55-L51-L55.

85. Marks, L.D., et al., *Direct methods for surfaces.* Surface Review and Letters, 1998. **5**(5): p. 1087-1106.

86. Schülli, T.U., et al., *Substrate-enhanced supercooling in AuSi eutectic droplets.* Nature, 2010. **464**(7292): p. 1174-1177.

87. Thiel, S., et al., *Electron Scattering at Dislocations in $LaAlO_3/SrTiO_3$ Interfaces.* Physical Review Letters, 2009. **102**(4): p. 046809-046809.

88. Mannhart, J. and D.G. Schlom, *Oxide Interfaces—An Opportunity for Electronics.* Science, 2010. **327**(5973): p. 1607-1611.

89. Liao, Y.C., et al., *Metal-insulator transition of the $LaAlO_3$-$SrTiO_3$ interface electron system.* Physical Review B, 2011. **83**(7): p. 075402-075402.

90. Caviglia, A.D., et al., *Electric field control of the $LaAlO_3/SrTiO_3$ interface ground state.* Nature, 2008. **456**(7222): p. 624-627.

91. Ariando, et al., *Electronic phase separation at the $LaAlO_3/SrTiO_3$ interface.* Nature Communications, 2011. **2**: p. 188-188.

92. Maurice, J.l., et al., *Electronic conductivity and structural distortion at the interface between insulators $SrTiO_3$ and $LaAlO_3$.* Physica status Solidi (A), 2006. **203**(9): p. 2209-2214.

93. Brinkman, A., et al., *Magnetic effects at the interface between non-magnetic oxides.* Nature Materials, 2007. **6**(7): p. 493-496.

94. Mortada, H., et al., *Structural investigation of the $LaAlO_3$(110) surface.* Thin Solid Films, 2008. **517**(1): p. 441-443.

95. Wang, Z.L., *Steps and facets on annealed $LaAlO_3$ {100} and {110} surfaces.* Surface Science, 1996. **360**(1–3): p. 180-186.

96. Knížek, K. *Kalvados - software for crystal structure and powder diffraction*. 2012; Available from: http://www.fzu.cz/~knizek/kalvados/index.html.

97. Brown, I.D., *# ACCUMULATED TABLE OF BOND VALENCE PARAMETERS*, 2011: http://www.iucr.org/__data/assets/file/0018/59004/bvparm2011.cif.

98. Collazo-Davila, C., et al., *Design and Initial Performance of an Ultrahigh Vacuum Sample Preparation Evaluation Analysis and Reaction (SPEAR) System.* Microscopy and Microanalysis, 1995. **1**(06): p. 267-279.

99. Miller, J.B., S.L. Bernasek, and J. Schwartz, *Surface Hydroxylation of Single Crystal Aluminum(110) in Ultrahigh Vacuum.* Langmuir, 1994. **10**(8): p. 2629-2635.

100. *MATLAB*, 2004, The MathWorks Inc.: Natick, Massachusetts.

101. Boyko, E. and L.G. Wisnyl, *The optical properties and structures of $CaO.2Al_2O_3$ and $SrO.2Al_2O_3$.* Acta Crystallographica, 1958. **11**(6): p. 444-445.

102. Iyi, N., et al., *The crystal structure of lanthanum hexaaluminate.* Journal of Solid State Chemistry, 1984. **54**(1): p. 70-77.

103. MacKenzie, K.J.D., et al., *Crystallization of fibre-coating compounds of potential use in fibre-reinforced oxide ceramics.* Journal of the European Ceramic Society, 2000. **20**(5): p. 645-650.

104. Tripodo, G., et al., *Studies of $LaAlO_3$ {100} surfaces using RHEED and REM II: 5 x 5 surface reconstruction.* Surface Science, 1995. **328**(1): p. 159-169.

105. Wang, Z.L. and A.J. Shapiro, *Studies of $LaAlO_3$ (100) surfaces using RHEED and REM. I: twins, steps and dislocations.* Surface Science, 1995. **328**(1–2): p. 141-158.

106. Yao, J., et al., *Thermal stimulation of the surface termination of $LaAlO_3$ {100}.* The Journal of Chemical Physics, 1998. **108**(4): p. 1645-1652.

107. van der Heide, P.A.W. and J.W. Rabalais, *Photoelectron spectroscopic study of the temperature-dependent termination of the $LaAlO_3$ (100) surface.* Chemical Physics Letters, 1998. **297**(3): p. 350-356.

108. Kawanowa, H., et al., *Structure analysis of $LaAlO_3$(001) surfaces by low energy neutral scattering spectroscopy.* Surface Science, 2002. **506**(1): p. 87-92.

109. Francis, R.J., S.C. Moss, and A.J. Jacobson, *X-ray truncation rod analysis of the reversible temperature-dependent [001] surface structure of $LaAlO_3$.* Physical Review B, 2001. **64**(23): p. 235425.

110. Miguel, M.A.S., et al., *On the origin of the reconstruction of $LaAlO_3$ {100} surfaces.* Surface Science, 1997. **389**(1): p. 1147-1152.

111. Jacobs, J.P., M.A. San Miguel, and L.J. Alvarez, *Studies of $LaAlO_3$ {100} surfaces by molecular dynamics simulations.* Journal of Molecular Structure: THEOCHEM, 1997. **390**(1): p. 193-198.

112. Fadley, C.S., *Angle-resolved x-ray photoelectron spectroscopy.* Progress in Surface Science, 1984. **16**(3): p. 275-388.

113. Egelhoff, W.F., Jr., *X-ray photoelectron and Auger-electron forward scattering: A new tool for studying epitaxial growth and core-level binding-energy shifts.* Physical Review B, 1984. **30**(2): p. 1052-1055.

114. Powell, C.J. and A. Jablonski, *NIST Electron Effective-Attenuation-Length Databse* Version 1.3 ed2011, Gaithersburg, MD: National Institute of Standards and Technology.

115. Clarke, D.R., *On the Equilibrium Thickness of Intergranular Glass Phases in Ceramic Materials.* Journal of the American Ceramic Society, 1987. **70**(1): p. 15-22.

116. Clarke, D.R., *High-Temperature Microstructure of a Hot-Pressed Silicon Nitride.* Journal of the American Ceramic Society, 1989. **72**(9): p. 1604-1609.

117. Tang, M., W.C. Carter, and R. Cannon, *Grain boundary order-disorder transitions.* Journal of Materials Science, 2006. **41**(23): p. 7691-7695.

118. Yoshiya, M., et al., *Theoretical Study on the Chemistry of Intergranular Glassy Film in Si_3N_4–SiO_2 Ceramics.* Journal of the American Ceramic Society, 2002. **85**(1): p. 109-112.

119. Becerra-Toledo, A.E., M.R. Castell, and L.D. Marks, *Water adsorption on $SrTiO_3$(001): I. Experimental and simulated STM.* Surface Science, 2012. **606**(7–8): p. 762-765.

120. Becerra-Toledo, A.E., et al., *Water adsorption on $SrTiO_3$(001): II. Water, water, everywhere.* Surface Science, 2012. **606**(9–10): p. 791-802.

121. Deak, D.S., et al., *Ordering of TiO_2-Based Nanostructures on $SrTiO_3$(001) Surfaces.* The Journal of Physical Chemistry B, 2006. **110**(18): p. 9246-9251.

122. Bals, S., et al., *High-Quality Sample Preparation by Low kV FIB Thinning for Analytical TEM Measurements.* Microscopy and Microanalysis, 2007. **13**(02): p. 80-86.

123. Kolpak, A.M., et al., *Evolution of the Structure and Thermodynamic Stability of the $BaTiO_3$(001) Surface.* Physical Review Letters, 2008. **101**(3): p. 036102.

124. Morales, E.H. and D.A. Bonnell, *On the relationship between surface reconstructions and step edge stability on $BaTiO_3$ (001).* Surface Science, 2013. **609**(0): p. 62-66.

125. Bando, H., et al., *Structure and electronic states on reduced $BaTiO_3$ (100) surface observed by scanning tunneling microscopy and spectroscopy.* Journal of Vacuum Science & Technology B, 1996. **14**(2): p. 1060-1063.

126. Martirez, J.M.P., et al., *Atomic and Electronic Structure of the $BaTiO_3$(001) (sqrt[5]×sqrt[5])R26.6° Surface Reconstruction.* Physical Review Letters, 2012. **109**(25): p. 256802.

127. Wang, Y.X., et al., *First-principles study of the (001) surface of cubic $CaTiO_3$.* Physical Review B, 2006. **73**(3): p. 035411.

128. Lin, Y., et al., *Synthesis-Dependent Atomic Surface Structures of Oxide Nanoparticles.* Physical Review Letters, 2013. **111**(15): p. 156101.

129. Zhou, J. and Z. Yang, *Solvothermal growth of sub-10 nm monodispersed $BaTiO_3$ nanocubes.* CrystEngComm, 2013. **15**(44): p. 8912-8914.

Appendix

The Crystallographic Information Files (CIF) for all relevant structures are found in this appendix. Additional information for structures referred to but not discussed can be found A.3.

A.1. Chapter 4 CIF files

$SrTiO_3$ (001) (√13x√13)R33.7°

```
STO_RT13
_symmetry_cell_setting     tetragonal
_symmetry_space_group_name_H-M   'P 1 1 2/m'
_symmetry_space_group_name_Hall   '-P 2'
_symmetry_Int_Tables_number   10
loop_
  _symmetry_equiv_pos_as_xyz
    x,y,z
    -x,-y,-z
    -x,y,-z
    x,-y,z
_cell_length_a      14.222100
_cell_length_b      14.222100
_cell_length_c      35.575400
_cell_angle_alpha   90.000000
_cell_angle_beta    89.999997
_cell_angle_gamma   90.000000
loop_
  _atom_site_label
  _atom_site_fract_x
  _atom_site_fract_y
  _atom_site_fract_z
  _atom_site_U_iso_or_equiv
  _atom_site_occupancy
  _atom_site_type_symbol
    O        0.961324   0.692059   0.270665  0.000  1.000 O
    O        0.152758   0.722555   0.276305  0.000  1.000 O
    O        0.196120   0.535087   0.273507  0.000  1.000 O
    O        0.000000   0.500000   0.282719  0.000  1.000 O
    O        0.003711   0.808505   0.667594  0.000  1.000 O
    O        0.291226   0.627532   0.666051  0.000  1.000 O
    O        0.741892   0.839882   0.269470  0.000  1.000 O
    O        0.316802   0.982096   0.280815  0.000  1.000 O
    O        0.410489   0.396715   0.271688  0.000  1.000 O
```

O	0.500000	0.000000	0.272548	0.000	1.000	O
O	0.464986	0.193901	0.284143	0.000	1.000	O
O	0.658101	0.221572	0.272715	0.000	1.000	O
O	0.595992	0.402447	0.280858	0.000	1.000	O
O	0.873441	0.087712	0.276729	0.000	1.000	O
O	0.777207	0.649452	0.267796	0.000	1.000	O
O	0.931039	0.907768	0.281375	0.000	1.000	O
O	0.799313	0.954354	0.666057	0.000	1.000	O
O	0.403463	0.894065	0.666714	0.000	1.000	O
O	0.342043	0.268723	0.671494	0.000	1.000	O
O	0.500000	0.500000	0.666213	0.000	1.000	O
O	0.601258	0.910585	0.645477	0.000	1.000	O
O	0.527696	0.292981	0.645225	0.000	1.000	O
O	0.000000	0.000000	0.645030	0.000	1.000	O
O	0.036057	0.814243	0.222284	0.000	1.000	O
O	0.274801	0.648087	0.221892	0.000	1.000	O
O	0.096244	0.438959	0.219514	0.000	1.000	O
O	0.815055	0.968481	0.221629	0.000	1.000	O
O	0.427402	0.881819	0.221441	0.000	1.000	O
O	0.360302	0.263291	0.221620	0.000	1.000	O
O	0.500000	0.500000	0.220339	0.000	1.000	O
O	0.731060	0.847091	0.167461	0.000	1.000	O
O	0.191946	0.537812	0.164627	0.000	1.000	O
O	0.537702	0.808755	0.163087	0.000	1.000	O
O	0.346722	0.768530	0.165941	0.000	1.000	O
O	0.154729	0.731688	0.168295	0.000	1.000	O
O	0.577433	0.614992	0.164954	0.000	1.000	O
O	0.770095	0.654248	0.171433	0.000	1.000	O
O	0.804199	0.961635	0.110662	0.000	1.000	O
O	0.418586	0.886974	0.110516	0.000	1.000	O
O	0.038890	0.805196	0.110809	0.000	1.000	O
O	0.659293	0.730034	0.111261	0.000	1.000	O
O	0.731534	0.344476	0.110612	0.000	1.000	O
O	0.500000	0.500000	0.109738	0.000	1.000	O
O	0.876136	0.584915	0.110122	0.000	1.000	O
O	0.385719	0.576558	0.165032	0.000	1.000	O
O	0.114835	0.923575	0.163915	0.000	1.000	O
O	0.922400	0.884825	0.165172	0.000	1.000	O
O	0.307001	0.961233	0.168378	0.000	1.000	O
O	0.500000	0.000000	0.165378	0.000	1.000	O
O	0.000000	0.500000	0.156454	0.000	1.000	O
O	0.962538	0.691577	0.166434	0.000	1.000	O
Ti	0.419284	0.880427	0.722772	0.000	1.000	Ti
Ti	0.446666	0.202328	0.664501	0.000	1.000	Ti
Ti	0.331111	0.998457	0.666433	0.000	1.000	Ti
Ti	0.416384	0.608040	0.666671	0.000	1.000	Ti
Ti	0.928990	0.909807	0.666737	0.000	1.000	Ti
Ti	0.887563	0.576542	0.837219	0.000	1.000	Ti
Ti	0.729797	0.345349	0.168200	0.000	1.000	Ti
Ti	0.654891	0.729295	0.167715	0.000	1.000	Ti
Ti	0.038501	0.811690	0.168079	0.000	1.000	Ti
Ti	0.424511	0.884009	0.166422	0.000	1.000	Ti
Ti	0.803982	0.962161	0.164257	0.000	1.000	Ti
Ti	0.500000	0.500000	0.163337	0.000	1.000	Ti
Ti	0.668920	0.710429	0.723948	0.000	1.000	Ti
Ti	0.257311	0.643542	0.282047	0.000	1.000	Ti
Ti	0.099907	0.419644	0.269959	0.000	1.000	Ti

Ti	0.053950	0.809039	0.281330	0.000	1.000	Ti
Ti	0.801494	0.951530	0.272526	0.000	1.000	Ti
Ti	0.500000	0.500000	0.271695	0.000	1.000	Ti
Sr	0.609635	0.920629	0.222742	0.000	1.000	Sr
Sr	0.540435	0.304941	0.222597	0.000	1.000	Sr
Sr	0.081105	0.621179	0.221233	0.000	1.000	Sr
Sr	0.000000	0.000000	0.777378	0.000	1.000	Sr
Sr	0.696664	0.534948	0.219266	0.000	1.000	Sr
Sr	0.148009	0.231248	0.219792	0.000	1.000	Sr
Sr	0.769617	0.158721	0.222496	0.000	1.000	Sr
Sr	0.461853	0.693385	0.110424	0.000	1.000	Sr
Sr	0.613661	0.921414	0.110356	0.000	1.000	Sr
Sr	0.230922	0.844512	0.110638	0.000	1.000	Sr
Sr	0.692263	0.537099	0.110099	0.000	1.000	Sr
Sr	0.847244	0.771522	0.110334	0.000	1.000	Sr
Sr	0.920042	0.380155	0.110021	0.000	1.000	Sr
Sr	0.000000	0.000000	0.110524	0.000	1.000	Sr
Sr	0.000000	0.000000	0.000000	0.000	1.000	Sr
Sr	0.152876	0.228711	0.000000	0.000	1.000	Sr
Sr	0.386124	0.077815	0.000000	0.000	1.000	Sr
Sr	0.538288	0.306626	0.000000	0.000	1.000	Sr
Sr	0.231044	0.844548	0.000000	0.000	1.000	Sr
Sr	0.920501	0.380508	0.000000	0.000	1.000	Sr
Sr	0.307587	0.462616	0.000000	0.000	1.000	Sr
O	0.343355	0.269097	0.000000	0.000	1.000	O
O	0.579487	0.113843	0.000000	0.000	1.000	O
O	0.732915	0.345551	0.000000	0.000	1.000	O
O	0.961503	0.193764	0.000000	0.000	1.000	O
O	0.879776	0.581116	0.000000	0.000	1.000	O
O	0.500000	0.500000	0.000000	0.000	1.000	O
O	0.077159	0.115888	0.055470	0.000	1.000	O
O	0.269500	0.152553	0.055281	0.000	1.000	O
O	0.461773	0.191588	0.055423	0.000	1.000	O
O	0.693873	0.039438	0.055253	0.000	1.000	O
O	0.347613	0.768366	0.054879	0.000	1.000	O
O	0.845056	0.267786	0.055448	0.000	1.000	O
O	0.885460	0.076452	0.055305	0.000	1.000	O
O	0.037554	0.309047	0.055189	0.000	1.000	O
O	0.231557	0.345514	0.055050	0.000	1.000	O
O	0.423506	0.384013	0.055225	0.000	1.000	O
O	0.615743	0.424043	0.054893	0.000	1.000	O
O	0.808898	0.461582	0.055451	0.000	1.000	O
Ti	0.194716	0.037165	0.054302	0.000	1.000	Ti
Ti	0.576242	0.115947	0.055240	0.000	1.000	Ti
Ti	0.961564	0.191297	0.055755	0.000	1.000	Ti
Ti	0.115123	0.422170	0.054194	0.000	1.000	Ti
Ti	0.343327	0.270174	0.055429	0.000	1.000	Ti
Ti	0.500000	0.500000	0.054658	0.000	1.000	Ti
Ti	0.269328	0.654567	0.055719	0.000	1.000	Ti
O	0.806187	0.961656	0.000000	0.000	1.000	O
O	0.000000	0.500000	0.055025	0.000	1.000	O
O	0.500000	0.000000	0.054966	0.000	1.000	O

$SrTiO_3$ (001) ($\sqrt{5}x\sqrt{5}$)R26.6°

```
STO_RT5
_cell_length_a    8.704965
_cell_length_b    8.704965
_cell_length_c   43.819773
_cell_angle_alpha   90.000000
_cell_angle_beta    90.000000
_cell_angle_gamma   90.000000
_symmetry_space_group_name_H-M         'P_1_1_2/m   '
_symmetry_space_group_name_Hall   '-P 2'
_symmetry_space_group_number   10
loop_
_symmetry_equiv_pos_as_xyz
   +x,+y,+z
   -x,-y,+z
   -x,-y,-z
   +x,+y,-z
loop_
_atom_site_label
_atom_site_type_symbol
_atom_site_fract_x
_atom_site_fract_y
_atom_site_fract_z
Ti001  Ti  0.00000000  0.00000000  0.31020461
Ti002  Ti  0.00000000  0.00000000  0.22196044
Ti003  Ti  0.00000000  0.00000000  0.13299360
Ti004  Ti  0.00000000  0.00000000  0.95561730
Sr005  Sr  0.69730797  0.90270229  0.26666807
Sr006  Sr  0.69914040  0.90086341  0.17789074
Sr007  Sr  0.69937583  0.90018146  0.08882155
O0008  O   0.00000000  0.00000000  0.26741707
O0009  O   0.00000000  0.00000000  0.17785814
O0010  O   0.00000000  0.00000000  0.08872257
O0011  O   0.79823438  0.09262112  0.30904661
O0012  O   0.92526190  0.79205814  0.31685555
O0013  O   0.79947668  0.09892728  0.22179419
O0014  O   0.90182738  0.80003201  0.22409168
O0015  O   0.80000919  0.10028064  0.13358288
O0016  O   0.89976153  0.80069493  0.13226538
O0017  O   0.79995849  0.09980669  0.95571668
O0018  O   0.00000000  0.50000000  0.95558535
O0019  O   0.60015555  0.70030034  0.95554521
O0020  O   0.50000000  0.00000000  0.95471424
O0021  O   0.90016062  0.79963608  0.95535630
O0022  O   0.69987371  0.40003570  0.95636206
O0023  O   0.00000000  0.00000000  0.00000000
Sr024  Sr  0.69959010  0.90005158  0.00000000
Ti025  Ti  0.20205259  0.39778299  0.31178129
Ti026  Ti  0.59379585  0.18876954  0.31317622
Ti027  Ti  0.19971939  0.39967210  0.22222358
Ti028  Ti  0.60059121  0.20211716  0.22352095
Ti029  Ti  0.19998568  0.39942224  0.13340082
Ti030  Ti  0.59959364  0.19968207  0.13365329
Ti031  Ti  0.20003549  0.40014430  0.95561752
```

```
Ti032  Ti  0.60014275  0.20021721  0.95550182
Sr033  Sr  0.89860389  0.30207715  0.26735099
Sr034  Sr  0.50000000  0.50000000  0.26856826
Sr035  Sr  0.89963221  0.30005138  0.17780656
Sr036  Sr  0.50000000  0.50000000  0.17801740
Sr037  Sr  0.89968782  0.30001184  0.08878051
Sr038  Sr  0.50000000  0.50000000  0.08886575
O0039  O   0.19682368  0.40921377  0.26750581
O0040  O   0.61728356  0.22604102  0.26743416
O0041  O   0.19778559  0.38809891  0.17782931
O0042  O   0.59095482  0.18877030  0.17833073
O0043  O   0.20173178  0.40463842  0.08892291
O0044  O   0.60380816  0.20522150  0.08896778
O0045  O   0.00000000  0.50000000  0.30964465
O0046  O   0.60860350  0.70802760  0.30668371
O0047  O   0.69190318  0.40983573  0.31876680
O0048  O   0.50000000  0.00000000  0.30456201
O0049  O   0.00000000  0.50000000  0.22122093
O0050  O   0.60081370  0.70081302  0.22313997
O0051  O   0.70094592  0.40176932  0.21933652
O0052  O   0.50000000  0.00000000  0.22735783
O0053  O   0.00000000  0.50000000  0.13350252
O0054  O   0.59934903  0.69900078  0.13285193
O0055  O   0.70070839  0.39955068  0.13522640
O0056  O   0.50000000  0.00000000  0.13139194
O0057  O   0.19917459  0.39845772  0.00000000
O0058  O   0.59815864  0.19693463  0.00000000
Sr059  Sr  0.89970441  0.30017717  0.00000000
Sr060  Sr  0.50000000  0.50000000  0.00000000
Ti061  Ti  0.96334159  0.77275399  0.35976964
Ti062  Ti  0.67528149  0.40150435  0.36258828
O0063  O   0.00000000  0.00000000  0.36006652
O0064  O   0.50000000  0.50000000  0.37744059
O0065  O   0.59320284  0.21250692  0.35580933
O0066  O   0.87142073  0.31920191  0.37566745
O0067  O   0.80649773  0.62587703  0.35866067
```

$SrTiO_3$ (001) 3x3

```
STO_3x3

_cell_length_a   11.678932

_cell_length_b   11.678932
_cell_length_c   34.339986
_cell_angle_alpha   90.000000
_cell_angle_beta    90.000000
_cell_angle_gamma   90.000000
_symmetry_space_group_name_H-M         'P_4/m_m_m'
_symmetry_space_group_name_Hall   '-P 4 2'
_symmetry_space_group_number  123
loop_
_symmetry_equiv_pos_as_xyz
```

```
   +x,+y,+z
   -x,-y,-z
   -x,-y,+z
   -x,+y,-z
   -x,+y,+z
   -y,-x,-z
   -y,-x,+z
   +y,-x,-z
   +y,-x,+z
   -y,+x,-z
   -y,+x,+z
   +y,+x,-z
   +y,+x,+z
   +x,-y,-z
   +x,-y,+z
   +x,+y,-z
loop_
_atom_site_label
_atom_site_type_symbol
_atom_site_fract_x
_atom_site_fract_y
_atom_site_fract_z
Ti001  Ti  0.34186175  0.16423652  0.34488012
O0002  O   0.00000000  0.33355451  0.34420278
O0003  O   0.33229983  0.33229983  0.34386561
O0004  O   0.18312620  0.18312620  0.35377493
O0005  O   0.50000000  0.16940884  0.35323057
O0006  O   0.00000000  0.16669689  0.28170943
O0007  O   0.66513262  0.16873754  0.28701495
O0008  O   0.00000000  0.50000000  0.28053883
O0009  O   0.67096639  0.50000000  0.27972376
Ti010  Ti  0.00000000  0.00000000  0.28369799
Ti011  Ti  0.66812598  0.00000000  0.28355484
Ti012  Ti  0.65556533  0.34443467  0.28539558
Sr013  Sr  0.83476333  0.16523667  0.23094694
Sr014  Sr  0.50000000  0.16476002  0.22989491
Sr015  Sr  0.50000000  0.50000000  0.22764304
O0016  O   0.00000000  0.00000000  0.22831371
O0017  O   0.66678522  0.00000000  0.22836186
O0018  O   0.66982740  0.33017260  0.22923752
O0019  O   0.00000000  0.16673729  0.17093967
O0020  O   0.66643316  0.16642222  0.17105731
O0021  O   0.00000000  0.50000000  0.17096100
O0022  O   0.66668614  0.50000000  0.17107436
Ti023  Ti  0.00000000  0.00000000  0.17090573
Ti024  Ti  0.66692517  0.00000000  0.17050364
Ti025  Ti  0.66726640  0.33273360  0.17084132
Sr026  Sr  0.83348995  0.16651005  0.11457180
Sr027  Sr  0.50000000  0.16658782  0.11450424
Sr028  Sr  0.50000000  0.50000000  0.11437767
O0029  O   0.00000000  0.00000000  0.11417224
O0030  O   0.66659119  0.00000000  0.11406827
O0031  O   0.66663348  0.33336652  0.11424515
O0032  O   0.00000000  0.16668275  0.05706973
O0033  O   0.66664529  0.16666683  0.05708140
O0034  O   0.00000000  0.50000000  0.05708033
O0035  O   0.66667225  0.50000000  0.05709058
```

Ti036	Ti	0.00000000	0.00000000	0.05701801
Ti037	Ti	0.66670023	0.00000000	0.05694875
Ti038	Ti	0.66669362	0.33330638	0.05697056
Sr039	Sr	0.83338025	0.16661975	0.00000000
Sr040	Sr	0.50000000	0.16663906	0.00000000
Sr041	Sr	0.50000000	0.50000000	0.00000000
O0042	O	0.00000000	0.00000000	0.00000000
O0043	O	0.66664373	0.00000000	0.00000000
O0044	O	0.66665357	0.33334643	0.00000000

A.2. Chapter 5 Supplemental Information

Details for entire set of dry $LaAlO_3$ (001) structures initially calculated for work presented in Chapter 5. Only relevant lowest energy structures defining the convex hull were described in the chapter.

Table A.2. Table of $LaAlO_3$ (110) structures with DFT calculated surface energies.

Label	Surface Cell	Description	Surface layer	Subsurface layer	Excess $AlO_{1.5}$	Surface Energy (eV/1x1)
A	1x1	Bulk terminated layer with 1 oxygen vacancy	O_2^{-}	O_2^{4-}	0	1.55
B (2x1)	2x1	Bulk terminated layer with 2 oxygen vacancies	$2O^{4-}$	$2(O_2^{4-})$	0	1.16
C	3x1	Bulk terminated layer with 2 La vacancies	$LaAl_3O_3^{6+}$	$LaAlO^{4+}$	0.667	2.13
D	3x1	2 Al adatoms	Al_2^{6+}	$3(O_2^{4-})$	0.667	2.61
E	1x1	2 Al and 2 O adatoms	$Al_2O_2^{2+}$	$3(O_2^{4-})$	2	3.11
F	3x1	Surface network of rings of 6 AlO_4	$Al_4O_3^{6+}$	$3(O_2^{4-})$	1.333	2.06
G	3x1	F with variation in oxygen position	$Al_4O_3^{6+}$	$3(O_2^{4-})$	1.333	2.13
H	3x1	F with additional AlO_2 in center of ring	$Al_6O_6^{6+}$	$3(O_2^{4-})$	2	3.17
I	3x1	Similar to H with inversion symmetry in-plane instead of mirror plane	$Al_6O_6^{6+}$	$3(O_2^{4-})$	2	2.65
J	3x1	H with different location of AlO_2	$Al_6O_6^{6+}$	$3(O_2^{4-})$	2	2.70
K	3x1	$Al_6O_6^{6+}$ in bulk like positions subsurface	Al_4O_6	$3(Al_2O_2^{2+})$	3.333	3.32
L	3x1	K with oxygen position variation	Al_4O_6	$3(Al_2O_2^{2+})$	3.333	3.15
M (3x1 Al-10)	3x1	STO 3x1-type surface with Al_5O_5	$Al_{10}O_{12}^{6+}$	$3(O_2^{4-})$	3.333	2.23
N	4x1	10 and 4 member AlO_x rings	Al_6O_9	$3(Al_2O_2^{2+})$	3.5	3.15
O	6x2	Double cell, STO 3x1-type surface with 1/2 occupancy oxygen	$Al_{20}O_{30}$	$3(Al_2O_2^{2+})$	3.667	3.59
P (3x1 Al-12)	3x1	STO 3x1-type surface with AlO_2 unit	Al_6O_8	$3(Al_2O_2^{2+})$	4	2.79
Q	2x1	Al_4O_6 six member rings	Al_4O_6	$3(Al_2O_2^{2+})$	4	4.20

A.3. Chapter 5 CIF Files

$LaAlO_3$ (110) 3x1 Al-10

```
LAO_3x1Al10
_cell_length_a   5.3393
_cell_length_b  37.3753
_cell_length_c  11.3264
_cell_angle_alpha   90.000
_cell_angle_beta   90.000
_cell_angle_gamma   90.000
_symmetry_space_group_name_H-M 'p112/m         '
loop_
_atom_site_label
_atom_site_type_symbol
_atom_site_fract_x
_atom_site_fract_y
_atom_site_fract_z
O1    O    0.8326441   0.6868204   0.2253539
O2    O    0.3986676   0.3769280   0.6925128
O3    O    0.1908504   0.3188518   0.5000000
O4    O    0.6714763   0.3226615   0.8471831
O5    O    0.5243054   0.3083034   0.6377076
O6    O    0.8911108   0.3523439   0.6191904
O7    O    0.0241311   0.2817021   0.0000000
O8    O    0.2755869   0.2439668   0.5000000
O9    O    0.7807124   0.2702730   0.5000000
O10   O    0.2693851   0.2486336   0.8187638
O11   O    0.7468027   0.2563486   0.8040945
O12   O    0.5412507   0.2090875   0.6639531
O13   O    0.5331645   0.2159900   0.0000000
O14   O    0.8275612   0.1867628   0.5000000
O15   O    0.3106374   0.1711698   0.5000000
O16   O    0.7973287   0.1822888   0.8410335
O17   O    0.2877661   0.1782773   0.8389695
O18   O    0.0142888   0.1448417   0.6674045
O19   O    0.0279049   0.1411410   0.0000000
O20   O    0.2263344   0.1017117   0.5000000
O21   O    0.7310503   0.1129995   0.5000000
O22   O    0.2694348   0.1078762   0.8282581
O23   O    0.7686065   0.1076861   0.8336083
O24   O    0.5151805   0.0708757   0.6662667
O25   O    0.5044854   0.0725024   0.0000000
O26   O    0.7955824   0.0411613   0.5000000
O27   O    0.2918057   0.0304043   0.5000000
O28   O    0.7460822   0.0349232   0.8357825
O29   O    0.2463758   0.0369211   0.8340492
O30   O    0.0000000   0.0000000   0.6673101
O31   O    0.0000000   0.0000000   0.0000000
Al1   Al   0.5311234   0.2149478   0.8325185
Al2   Al   0.0644759   0.7072842   0.8591822
Al3   Al   0.3479125   0.6489378   0.2785320
Al4   Al   0.4882636   0.9286065   0.5000000
Al5   Al   0.4908768   0.9282684   0.8338874
```

```
Al6   Al   0.7930656   0.6576389   0.3504709
Al7   Al   0.5549184   0.7160670   0.5000000
Al8   Al   0.5390589   0.7131317   0.2158189
Al9   Al   0.9741117   0.8561718   0.8344307
Al10  Al   0.0194676   0.1432902   0.5000000
Al11  Al   0.4802391   0.7908414   0.5000000
Al12  Al   0.0000000   0.0000000   0.1653503
Al13  Al   0.0000000   0.0000000   0.5000000
Al14  Al   0.8529876   0.3182351   0.5000000
La1   La   0.5181976   0.1423417   0.6715855
La2   La   0.5281684   0.1445381   0.0000000
La3   La   0.0100009   0.0715162   0.6685317
La4   La   0.0120582   0.0721602   0.0000000
La5   La   0.5000000   0.0000000   0.6693098
La6   La   0.5000000   0.0000000   0.0000000
La7   La   0.0175827   0.2163469   0.6678191
La8   La   0.0544391   0.2162607   0.0000000
```

$LaAlO_3$ (110) 3x1 Al-12

```
LAO_3x1Al12
_symmetry_cell_setting     orthorhombic
_symmetry_space_group_name_H-M   'P_1_1_2/m'
_symmetry_space_group_name_Hall   '-P 2'
_symmetry_Int_Tables_number   10
loop_
  _symmetry_equiv_pos_as_xyz
    x,y,z
    -x,-y,-z
    -x,-y,z
    x,y,-z
_cell_length_a      5.339340
_cell_length_b      37.375300
_cell_length_c      11.326400
_cell_angle_alpha   90.000000
_cell_angle_beta    90.000000
_cell_angle_gamma   89.999997
loop_
  _atom_site_label
  _atom_site_fract_x
  _atom_site_fract_y
  _atom_site_fract_z
  _atom_site_U_iso_or_equiv
  _atom_site_occupancy
  _atom_site_type_symbol

O34   0.875631    0.377308    0.500000    0     1     O
O32   0.404507    0.369931    0.366474    0     1     O
Al15  0.201723    0.368386    0.500000    0     1     Al
O31   0.930167    0.359712    0.271233    0     1     O
Al6   0.710229    0.353172    0.373537    0     1     Al
Al5   0.20489     0.336546    0.30339     0     1     Al
O29   0.235395    0.321298    0.848549    0     1     O
O33   0.249715    0.321007    0.500000    0     1     O
```

O30	0.763558	0.319374	0.500000	0	1	O
Al13	0.235751	0.317409	0.000000	0	1	Al
O2	0.526643	0.303588	0.313804	0	1	O
O16	0.526979	0.296749	0.00000	0	1	O
O1	0.033273	0.289245	0.332801	0	1	O
Al7	0.51107	0.287665	0.500000	0	1	Al
Al11	0.008537	0.286366	0.500000	0	1	Al
O15	0.996453	0.285657	0.00000	0	1	O
Al4	0.501013	0.284955	0.166883	0	1	Al
Al3	0.01205	0.281465	0.176834	0	1	Al
O18	0.751414	0.251329	0.168977	0	1	O
O4	0.753762	0.251135	0.500000	0	1	O
O3	0.264706	0.250708	0.500000	0	1	O
O17	0.26224	0.248826	0.16484	0	1	O
La8	0.011354	0.213676	0.662751	0	1	La
La3	0.002086	0.213636	0.00000	0	1	La
Al9	0.507231	0.213299	0.500000	0	1	Al
Al2	0.50787	0.211454	0.832287	0	1	Al
O19	0.517286	0.2094	0.00000	0	1	O
O5	0.502326	0.208973	0.333407	0	1	O
O20	0.771992	0.179766	0.168709	0	1	O
O6	0.764073	0.179094	0.500000	0	1	O
O7	0.249965	0.178596	0.500000	0	1	O
O21	0.256649	0.177314	0.164381	0	1	O
La1	0.504096	0.142474	0.666149	0	1	La
Al8	0.003879	0.142308	0.833152	0	1	Al
Al12	0.004532	0.142302	0.500000	0	1	Al
La2	0.502475	0.142269	0.000000	0	1	La
O8	0.006205	0.142246	0.333564	0	1	O
O22	0.997659	0.142029	0.000000	0	1	O
O24	0.745498	0.107776	0.16809	0	1	O
O10	0.750886	0.10715	0.500000	0	1	O
O9	0.252951	0.106812	0.500000	0	1	O
O23	0.246983	0.106041	0.165861	0	1	O
Al1	0.50112	0.071146	0.166827	0	1	Al
La7	0.001267	0.071134	0.000000	0	1	La
Al14	0.501195	0.071112	0.500000	0	1	Al
La5	0.001792	0.071091	0.33323	0	1	La
O25	0.503636	0.070803	0.000000	0	1	O
O11	0.500146	0.070671	0.333415	0	1	O
O26	0.754726	0.036201	0.166978	0	1	O
O12	0.751816	0.035759	0.500000	0	1	O
O13	0.250685	0.035489	0.500000	0	1	O
O27	0.253797	0.035047	0.16633	0	1	O
O14	0.00000	0.000000	0.333304	0	1	O
O28	0.00000	0.000000	0.000000	0	1	O
Al10	0.00000	0.000000	0.500000	0	1	Al
Al16	0.00000	0.000000	0.833409	0	1	Al
La4	0.50000	0.000000	0.333348	0	1	La
La6	0.50000	0.000000	0.000000	0	1	La

$LaAlO_3$ (110) 3x1 H-1

```
LAO_3x1H1
_cell_length_a   5.3393
_cell_length_b  37.3753
_cell_length_c  11.3264
_cell_angle_alpha   90.000
_cell_angle_beta   90.000
_cell_angle_gamma   90.000
_symmetry_space_group_name_H-M 'P112/m         '
loop_
_atom_site_label
_atom_site_type_symbol
_atom_site_fract_x
_atom_site_fract_y
_atom_site_fract_z
O1    O    0.9971154   0.2829846   0.0000000
O2    O    0.0609498   0.8022159   0.3666876
O3    O    0.7755495   0.7495633   0.5000000
O4    O    0.2682047   0.7445033   0.5000000
O5    O    0.0107933   0.7098787   0.3300225
O6    O    0.2268516   0.6734746   0.5000000
O7    O    0.7239619   0.6809128   0.5000000
O8    O    0.5040885   0.6434309   0.3324310
O9    O    0.7825864   0.6110391   0.5000000
O10   O    0.2842178   0.6023823   0.5000000
O11   O    0.0005391   0.5709657   0.3333620
O12   O    0.2174744   0.5309653   0.5000000
O13   O    0.7172422   0.5401907   0.5000000
O14   O    0.5000000   0.5000000   0.3330512
O15   O    0.7274356   0.7484265   0.1830976
O16   O    0.2299904   0.7612851   0.1808753
O17   O    0.2944907   0.6851864   0.1609342
O18   O    0.7849856   0.6752007   0.1588106
O19   O    0.4993711   0.6427268   0.0000000
O20   O    0.7274926   0.6037313   0.1659846
O21   O    0.2267740   0.6116635   0.1683149
O22   O    0.0066785   0.5718285   0.0000000
O23   O    0.2774968   0.5396177   0.1667974
O24   O    0.7764786   0.5321699   0.1655495
O25   O    0.5000000   0.5000000   0.0000000
O26   O    0.2548112   0.1840324   0.8336776
O27   O    0.5686290   0.1989172   0.0000000
Al1   Al   0.9973726   0.4283596   0.1674506
Al2   Al   0.0093911   0.7148138   0.8337442
Al3   Al   0.4897880   0.2146273   0.1461706
Al4   Al   0.0375583   0.2118547   0.2339260
Al5   Al   0.0355936   0.7814386   0.5000000
Al6   Al   0.4946492   0.3566939   0.8313806
Al7   Al   0.0001096   0.7122877   0.5000000
Al8   Al   0.5000000   0.5000000   0.5000000
Al9   Al   0.5026348   0.6423736   0.5000000
Al10  Al   0.0008744   0.5712993   0.5000000
Al11  Al   0.5000000   0.5000000   0.8332511
H1    H    0.4381781   0.1793848   0.0000000
```

```
La1   La   0.0005686   0.6436405   0.6661067
La2   La   0.0077129   0.6420394   0.0000000
La3   La   0.5243742   0.7092074   0.0000000
La4   La   0.0000000   0.5000000   0.3330625
La5   La   0.4978892   0.4284791   0.3330547
La6   La   0.0000000   0.5000000   0.0000000
La7   La   0.5037562   0.5712820   0.0000000
La8   La   0.5011220   0.7172860   0.6538306
```

$LaAlO_3$ (110) 3x1 H-5

```
LAO_3x1H5
_cell_length_a   5.3600
_cell_length_b  37.0882
_cell_length_c  11.3700
_cell_angle_alpha   90.000
_cell_angle_beta   90.000
_cell_angle_gamma   90.000
_symmetry_space_group_name_H-M 'p112/m         '
loop_
_atom_site_label
_atom_site_type_symbol
_atom_site_fract_x
_atom_site_fract_y
_atom_site_fract_z
O1    O    0.9921217   0.7193457   0.5000000
O2    O    0.9839900   0.1943426   0.8729824
O3    O    0.2385666   0.2521628   0.0000000
O4    O    0.7461856   0.2544162   0.0000000
O5    O    0.9947361   0.2918321   0.8306952
O6    O    0.7672487   0.3262136   0.0000000
O7    O    0.2708483   0.3204147   0.0000000
O8    O    0.4971504   0.3559676   0.8312822
O9    O    0.2224224   0.3899207   0.0000000
O10   O    0.7191377   0.3972173   0.0000000
O11   O    0.9968830   0.4293284   0.8331737
O12   O    0.7777185   0.4685828   0.0000000
O13   O    0.2781078   0.4605091   0.0000000
O14   O    0.5000000   0.5000000   0.8324872
O15   O    0.2563174   0.2442357   0.6958106
O16   O    0.7621561   0.2439844   0.6883852
O17   O    0.7251294   0.3170280   0.6549588
O18   O    0.2363305   0.3209928   0.6569149
O19   O    0.4943648   0.3580529   0.5000000
O20   O    0.2619294   0.3943805   0.6681445
O21   O    0.7650557   0.3895555   0.6670366
O22   O    0.9980823   0.4278563   0.5000000
O23   O    0.7289442   0.4613190   0.6652872
O24   O    0.2305085   0.4666476   0.6655005
O25   O    0.5000000   0.5000000   0.5000000
O26   O    0.7408675   0.8211738   0.3277409
O27   O    0.5295272   0.7880642   0.5000000
O28   O    0.2428913   0.8218032   0.3308321
```

```
Al1   Al   0.9915202   0.2841592   0.3321501
Al2   Al   0.4876907   0.7876948   0.6578800
Al3   Al   0.9935781   0.7906947   0.7314209
Al4   Al   0.9891696   0.2191303   0.0000000
Al5   Al   0.5030312   0.6436781   0.3333878
Al6   Al   0.0005841   0.2886236   0.0000000
Al7   Al   0.5000000   0.5000000   0.0000000
Al8   Al   0.4972738   0.3579043   0.0000000
Al9   Al   0.9983083   0.4289497   0.0000000
Al10  Al   0.5000000   0.5000000   0.3342229
Al11  Al   0.0031544   0.5718012   0.6666553
H1    H    0.6532817   0.8080059   0.5000000
H2    H    0.2573931   0.8418900   0.2765888
H3    H    0.7267790   0.8441498   0.2882661
La1   La   0.4973082   0.4286206   0.8322827
La2   La   0.5039723   0.5718384   0.5000000
La3   La   0.5037343   0.7164137   0.8455006
La4   La   0.0005097   0.6431693   0.8327701
La5   La   0.0077271   0.6434723   0.5000000
La6   La   0.5191209   0.7115842   0.5000000
La7   La   0.0000000   0.5000000   0.1673322
La8   La   0.0000000   0.5000000   0.5000000
```

$LaAlO_3$ (110) 2x1

```
LAO_2x1
_cell_length_a  37.3753
_cell_length_b   5.3393
_cell_length_c   7.5510
_cell_angle_alpha   90.000
_cell_angle_beta   90.000
_cell_angle_gamma   90.000
_symmetry_space_group_name_H-M 'pccm           '
loop_
_atom_site_label
_atom_site_type_symbol
_atom_site_fract_x
_atom_site_fract_y
_atom_site_fract_z
O1    O    0.6150741   0.8132569   0.5000000
O2    O    0.6411055   0.5000000   0.2500000
O3    O    0.6855091   0.7149739   0.5000000
O4    O    0.6697963   0.2230388   0.5000000
O5    O    0.7130770   0.0000000   0.2500000
O6    O    0.7441025   0.2847014   0.5000000
O7    O    0.7550275   0.7876737   0.5000000
O8    O    0.7852216   0.5000000   0.2500000
O9    O    0.8261717   0.7156196   0.5000000
O10   O    0.8162535   0.2168495   0.5000000
O11   O    0.8568702   0.0000000   0.2500000
O12   O    0.8880470   0.2827467   0.5000000
O13   O    0.8974851   0.7831446   0.5000000
O14   O    0.9284474   0.5000000   0.2500000
O15   O    0.9597231   0.2188882   0.5000000
```

```
O16   O    0.9688061   0.7187058   0.5000000
O17   O    0.0000000   0.0000000   0.2500000
Al1   Al   0.3559210   0.4621260   0.5000000
Al2   Al   0.2146110   0.4985354   0.5000000
Al3   Al   0.0715042   0.4995336   0.5000000
Al4   Al   0.1430465   0.0002687   0.5000000
Al5   Al   0.2866037   0.9977285   0.5000000
Al6   Al   0.0000000   0.0000000   0.5000000
La1   La   0.8570447   0.5000000   0.2500000
La2   La   0.9285722   0.0000000   0.2500000
La3   La   0.7139331   0.5000000   0.2500000
La4   La   0.7853754   0.0000000   0.2500000
La5   La   0.6399922   0.0000000   0.2500000
La6   La   0.0000000   0.5000000   0.2500000
```

$LaAlO_3$ (110) 1x1 H

```
LAO_1x1H
_cell_length_a   3.7755
_cell_length_b   5.3393
_cell_length_c  37.3753
_cell_angle_alpha   90.000
_cell_angle_beta   90.000
_cell_angle_gamma   90.000
_symmetry_space_group_name_H-M 'pmmm           '
loop_
_atom_site_label
_atom_site_type_symbol
_atom_site_fract_x
_atom_site_fract_y
_atom_site_fract_z
H1    H    0.0000000   0.7293098   0.3457534
O1    O    0.0000000   0.7608558   0.3202070
O2    O    0.5000000   0.5000000   0.2828520
O3    O    0.0000000   0.2446624   0.2513261
O4    O    0.5000000   0.0000000   0.2152435
O5    O    0.0000000   0.7498959   0.1792093
O6    O    0.5000000   0.5000000   0.1427660
O7    O    0.0000000   0.2496747   0.1073665
O8    O    0.5000000   0.0000000   0.0715183
O9    O    0.0000000   0.7500745   0.0357595
O10   O    0.5000000   0.5000000   0.0000000
Al1   Al   0.0000000   0.5000000   0.8567318
Al2   Al   0.0000000   0.0000000   0.9284894
Al3   Al   0.0000000   0.0000000   0.7852600
Al4   Al   0.0000000   0.5000000   0.7134975
Al5   Al   0.0000000   0.5000000   0.0000000
La1   La   0.5000000   0.5000000   0.2154846
La2   La   0.5000000   0.0000000   0.1429792
La3   La   0.5000000   0.0000000   0.2851588
La4   La   0.5000000   0.5000000   0.0715870
La5   La   0.5000000   0.0000000   0.0000000
```

$LaAlO_3$ (110) 1x1 AlH

```
LAO_1x1AlH
_cell_length_a  37.3753
_cell_length_b   5.3393
_cell_length_c   3.7755
_cell_angle_alpha   90.000
_cell_angle_beta   90.000
_cell_angle_gamma   90.000
_symmetry_space_group_name_H-M 'pmmm           '
loop_
_atom_site_label
_atom_site_type_symbol
_atom_site_fract_x
_atom_site_fract_y
_atom_site_fract_z
O     O    0.3612835   0.0000000   0.5000000
O     O    0.3544415   0.5000000   0.5000000
O     O    0.3201306   0.2469853   0.0000000
O     O    0.2791657   0.0000000   0.5000000
O     O    0.2484430   0.7436585   0.0000000
O     O    0.2124917   0.5000000   0.5000000
O     O    0.1772614   0.2491359   0.0000000
O     O    0.1411877   0.0000000   0.5000000
O     O    0.1063434   0.7492715   0.0000000
O     O    0.0707982   0.5000000   0.5000000
O     O    0.0354445   0.7500976   0.0000000
O     O    0.0000000   0.0000000   0.5000000
Al    Al   0.6464428   0.5000000   0.0000000
Al    Al   0.7876743   0.5000000   0.0000000
Al    Al   0.9291756   0.5000000   0.0000000
Al    Al   0.8583246   0.0000000   0.0000000
Al    Al   0.7173054   0.0000000   0.0000000
Al    Al   0.0000000   0.0000000   0.0000000
La    La   0.1415398   0.5000000   0.5000000
La    La   0.0708662   0.0000000   0.5000000
La    La   0.2825327   0.5000000   0.5000000
La    La   0.2126398   0.0000000   0.5000000
Al    Al   0.3555777   0.0000000   0.0000000
La    La   0.0000000   0.5000000   0.5000000
O     O    0.3913152   0.2558572   0.0000000
H     H    0.4170986   0.2603499   0.0000000
H     H    0.3873261   0.0000000   0.5000000
H     H    0.3805903   0.5000000   0.5000000
```

A.4. Chapter 6 MATLAB Code

The following code can be executed in MATLAB to reproduce the three-dimensional convex-hull presented in Chapter 6.

```
%%%%%%%%%%%%%%%%%%%%%%%%%%%%%%%%%%%%%%%%%%%%%%%%%%%%%%%%%%%%%%%%%%%%%%%%%%%%
%x-axis:excess AlO1.5 per 1x1
%y-axis:excess H2O per 1x1
%z-axis:energy per 1x1 in eV

%The following coordinates are in the form of:
%Structure_Name=[(excess AlO1.5) (excess H2O) {energy}]
two_x_1=[0 0 1.508];
N10a=[3.333 0 3.469];
N12=[4 0 4.155];
N12_5H=[1.667 0.1667 2.816];
One_x_1H=[0 2 0];
N12Sat=[1.667 0.833 1.102];
One_x_1AlH=[2 4 1.280];

%The following are used for plotting error bars
x=[0 3.333 4 1.667 0 1.667 2];
y=[0 0 0 0.1667 2 0.833 4];
z=[1.508 3.469 4.155 2.816 0 1.102 1.28];
e=[0.05 0.05 0.05 0.05 0.05 0.05 0.05];

%The following create 2d planes between 3 data points
%Fill One_x_1H=[0 2 0] to two_x_1=[0 0 1.508] to N12Sat=[1.667 0.833 1.102];
tri1x=[0 0 1.667];
tri1y=[2 0 0.833];
tri1z=[0 1.508 1.102];
%Fill  N10a=[3.333  0  3.469]  to  two_x_1=[0  0  1.508]  to  N12Sat=[1.667  0.833
1.102]
tri2x=[3.333 0 1.667];
tri2y=[0 0 0.833];
tri2z=[3.469 1.508 1.102];
%Fill  One_x_1H=[0  2  0]  to  One_x_1AlH=[2  2  1.280]  to  N12Sat=[1.667  0.833
1.102]
tri3x=[0 2 1.667];
tri3y=[2 4 0.833];
tri3z=[0 1.280 1.102];
%Fill N12=[4 0 4.155] to One_x_1AlH=[2 2 1.280] to N12Sat=[1.667 0.833 1.102]
tri4x=[4 2 1.667];
tri4y=[0 4 0.833];
tri4z=[4.155 1.280 1.102];
%Fill N10a=[3.333 0 3.469] to N12Sat=[1.667 0.833 1.102] to N12=[4 0 4.155];
tri5x=[3.333 1.667 4];
tri5y=[0 0.833 0];
tri5z=[3.469 1.102 4.155];
hold off

%Plot data points
```

```
h1=plot3(...
    two_x_1(1),two_x_1(2),two_x_1(3),'b.',...
    N10a(1),N10a(2),N10a(3),'b.',...
    N12(1),N12(2),N12(3),'b.',...
    N12_5H(1),N12_5H(2),N12_5H(3),'r.',...
    One_x_1H(1),One_x_1H(2),One_x_1H(3),'r.',...
    N12Sat(1),N12Sat(2),N12Sat(3),'r.',...
    One_x_1AlH(1),One_x_1AlH(2),One_x_1AlH(3),'r.');
set(h1,'MarkerSize',20,'LineWidth',2);
hold on
%Plot 2d planes
f=fill3(tri1x,tri1y,tri1z,'y');
f2=fill3(tri2x,tri2y,tri2z,'c');
f3=fill3(tri3x,tri3y,tri3z,'g');
f4=fill3(tri4x,tri4y,tri4z,'r');
f5=fill3(tri5x,tri5y,tri5z,'b');
set(f,'FaceAlpha',.1);
set(f2,'FaceAlpha',.1);
set(f3,'FaceAlpha',.1);
set(f4,'FaceAlpha',.1);
set(f5,'FaceAlpha',.1);
grid on
box on
%Axis labels
axislabx=xlabel('Excess AlO_{1.5}/(1x1)');
axislaby=ylabel('Excess H_{2}O/(1x1)');
axislabz=zlabel('Energy (eV/1x1)');
set(axislabx,'FontWeight','bold','FontSize',20);
set(axislaby,'FontWeight','bold','FontSize',20);
set(axislabz,'FontWeight','bold','FontSize',20);
axis([0 4 0 4 0 5]);
set(gca,'LineWidth',1);

%Data point labels
labels={'2x1' '3x1 Al-10' '3x1 Al-12' ...
    '3x1 H-1' '1x1 H' '3x1 H-5' '1x1 AlH'};

%Makes error bars
top=.02;
for i=1:length(x)
  xV = [x(i); x(i)];
      yV = [y(i); y(i)];
    zV = [z(i); z(i)];
      zMin = z(i) + e(i);
      zMax = z(i) - e(i);
    xMin = x(i)+ top;
    xMax = x(i)- top;

      zBar = [zMin, zMax];
    xBar = [xMin, xMax];
    xTop = [z(i)+e(i); z(i)+e(i)];
    xBot = [z(i)-e(i); z(i)-e(i)];
      % draw vertical error bar
      h=plot3(xV, yV, zBar, '-k');
      set(h, 'LineWidth', 1);
    %draw error bar tops in x direction on top and bottom
    h2=plot3(xBar,yV,xTop,'-k');
```

```
    set(h2, 'LineWidth', 1);
    h3=plot3(xBar,yV,xBot,'-k');
    set(h3, 'LineWidth', 1);
    %Add data point labels
    if i==6||i==3||i==1||i==7
        h4=text(x(i),y(i)+.04,z(i),labels(i));

set(h4,'FontSize',15,'FontWeight','bold','HorizontalAlignment','right');
    else
    h4=text(x(i)+.01,y(i)-.04,z(i),labels(i));
    set(h4,'FontSize',15,'FontWeight','bold','HorizontalAlignment','left');
    end
end
%%%%%%%%%%%%%%%%%%%%%%%%%%%%%%%%%%%%%%%%%%%%%%%%%%%%%%%%%%%%%%%%%%%%%%%%%%%%
```